Closing the reactive carbon flux budget: Observations from dual mass spectrometers over a coniferous forest

Michael P Vermeuel[1], Dylan B. Millet[2], Delphine Farmer[3], Matson A. Pothier[4], Michael F. Link[3], Mj Riches[3], Sara Williams[3], and Lauren A. Garofalo[4]

[1]University of Minnesota - Twin Cities Department of Soil, Water, and Climate
[2]University of Minnesota
[3]Colorado State University
[4]Department of Chemistry, Colorado State University

February 27, 2023

Abstract

We use observations from dual high-resolution mass spectrometers to characterize ecosystem-atmosphere fluxes of reactive carbon across an extensive range of volatile organic compounds (VOCs) and test how well that exchange is represented in current chemical transport models. Measurements combined proton-transfer reaction mass spectrometry (PTRMS) and iodide chemical ionization mass spectrometry (ICIMS) over a Colorado pine forest; together, these techniques have been shown to capture the majority of ambient VOC abundance and reactivity. Total VOC mass and associated OH reactivity fluxes were dominated by emissions of 2-methyl-3-buten-2-ol, monoterpenes, and small oxygenated VOCs, with a small number of compounds detected by PTRMS driving the majority of both net and upward exchanges. Most of these dominant species are explicitly included in chemical models, and we find here that GEOS-Chem accurately simulates the net and upward VOC mass and OH reactivity fluxes under clear sky conditions. However, large upward terpene fluxes occurred during sustained rainfall, and these are not captured by the model. Far more species contributed to the downward fluxes than are explicitly modeled, leading to a major underestimation of this key sink of atmospheric reactive carbon. This model bias mainly reflects missing and underestimated concentrations of depositing species, though inaccurate deposition velocities also contribute. The deposition underestimate is particularly large for assumed isoprene oxidation products, organic acids, and nitrates—species that are primarily detected by ICIMS. Ecosystem-atmosphere fluxes of ozone reactivity were dominated by sesquiterpenes and monoterpenes, highlighting the importance of these species for predicting near-surface ozone, oxidants, and aerosols.

Closing the reactive carbon flux budget: Observations from dual mass spectrometers over a coniferous forest

Michael P. Vermeuel[1], Dylan B. Millet[1*,] Delphine K. Farmer[2], Matson A. Pothier[2], Michael F. Link[2^], Mj Riches[2], Sara Williams[2], Lauren A. Garofalo[2]

[1] Department of Soil, Water, and Climate, University of Minnesota – Twin Cities, St. Paul, MN, USA

[2] Department of Chemistry, Colorado State University, Fort Collins, CO, USA

[^]now at Engineering Laboratory, National Institute of Standards and Technology, Gaithersburg, MD, USA

[*]Correspondence to D.B. Millet, dbm@umn.edu

Key Points

1. A small number of known organic compounds dominate the net and upward reactive carbon fluxes over a coniferous forest.
2. PTRMS captures VOCs controlling the net and upward fluxes, while ICIMS measures a range of important depositing species.
3. Far more VOCs contribute to the downward fluxes than are currently modeled, leading to a major sink underestimate.

Abstract

We use observations from dual high-resolution mass spectrometers to characterize ecosystem-atmosphere fluxes of reactive carbon across an extensive range of volatile organic compounds (VOCs) and test how well that exchange is represented in current chemical transport models. Measurements combined proton-transfer reaction mass spectrometry (PTRMS) and iodide chemical ionization mass spectrometry (ICIMS) over a Colorado pine forest; together, these techniques have been shown to capture the majority of ambient VOC abundance and reactivity. Total VOC mass and associated OH reactivity fluxes were dominated by emissions of 2-methyl-3-buten-2-ol, monoterpenes, and small oxygenated VOCs, with a small number of compounds detected by PTRMS driving the majority of both net and upward exchanges. Most of these dominant species are explicitly included in chemical models, and we find here that GEOS-Chem accurately simulates the net and upward VOC mass and OH reactivity fluxes under clear sky conditions. However, large upward terpene fluxes occurred during sustained rainfall, and these are not captured by the model. Far more species contributed to the downward fluxes than are explicitly modeled, leading to a major underestimation of this key sink of atmospheric reactive carbon. This model bias mainly reflects missing and underestimated concentrations of depositing species, though inaccurate deposition velocities also contribute. The deposition underestimate is particularly large for assumed isoprene oxidation products, organic acids, and nitrates—species that are primarily detected by ICIMS. Ecosystem-atmosphere fluxes of ozone reactivity were dominated by sesquiterpenes and monoterpenes, highlighting the importance of these species for predicting near-surface ozone, oxidants, and aerosols.

Plain Language Summary

Reactive carbon species in the atmosphere have a strong influence on air quality and climate and require accurate modeling to understand their global impacts. Natural ecosystems such as forests both emit and take up reactive carbon to and from the atmosphere, acting simultaneously as the largest source and an important sink of these species. We performed the most comprehensive measurements to date of this two-way reactive carbon exchange over a pine forest. We observed that the upward reactive carbon exchange was controlled by just a few known species and was much larger than the downward exchange, which was composed of far more species. We compared

the observations to chemical model predictions and found that the model accurately simulates the net reactive carbon exchange over this forest because the few species dominating that exchange are included in the model. However, the model does not adequately simulate the many depositing species, leading to a large underestimate for this sink of atmospheric reactive carbon.

1. Background

Surface-atmosphere exchange of volatile organic compounds (VOCs) plays a major role in modifying the chemical and physical properties of the atmosphere. In particular, the terrestrial biosphere is a major source of biogenic VOCs to the atmosphere (~1000 Tg C yr^{-1}) that is nearly an order of magnitude larger than the estimated anthropogenic source (90-160 Tg C yr^{-1}) (Boucher et al., 2013; Glasius & Goldstein, 2016; Huang et al., 2017). Emission uncertainties for these biogenic VOCs frequently exceed 200% both globally and regionally (Sindelarova et al., 2014). Even for isoprene, the best-studied biogenic VOC, model disparities can reach a factor of 4 (Arneth et al., 2011). Developing an improved understanding of biosphere VOC emissions is thus an important science priority.

At the same time, terrestrial ecosystems are a primary depositional sink for oxygenated VOCs, which are compounds that can be directly emitted or formed in the atmosphere through VOC oxidation. Additional oxygenated VOC sinks include chemical reactions, wet scavenging, and condensation to form secondary organic aerosol (SOA) (Lary & Shallcross, 2000; Mellouki et al., 2015; Muller & Brasseur, 1999; Singh et al., 1995). Since oxygenated VOCs are ubiquitous and represent the majority of ambient reactive carbon (Bates et al., 2021; Chen et al., 2019; Heikes, 2002; Jacob et al., 2002; Millet et al., 2008, 2010, 2015), uncertainties in their dry deposition limit our understanding both of the overall VOC budget (Safieddine et al., 2017) and of the partitioning between reactive carbon loss pathways. For example, prior studies have shown that deposition uncertainties encompass a range that can change predicted oxygenated VOC and SOA concentrations by as much as 50% (Bessagnet et al., 2010; Nguyen et al., 2015).

With up to 10^5 different organic species thought to exist in the atmosphere (Goldstein & Galbally, 2007), there are open questions regarding the number of VOCs undergoing surface-atmosphere exchange (Park et al., 2013), the main environmental factors driving that exchange (Yáñez-Serrano et al., 2015), and the extent to which those factors are represented in current chemical transport models (CTMs; Millet et al., 2018). To date there have been few direct ecosystem-scale flux observations with comprehensive VOC coverage to address those questions. Park et al. (2013) performed detailed flux measurements over an orange orchard and detected 555 species contributing to the net VOC flux budget—with 10 commonly-known compounds making up 68% of the total flux. A recent study over a winter wheat field measured fluxes for 264 VOCs, with only four ubiquitous oxygenated VOCs accounting for 85% of total emissions (Loubet et al., 2022). A third study over a mixed temperate forest observed 377 VOCs with detectable surface-atmosphere exchange (Millet et al., 2018). While the GEOS-Chem CTM underestimated net fluxes by 40-60%, the exchange was dominated (90% on a carbon basis) by known VOCs included in the CTM—and isoprene alone represented >90% of the OH reactivity-weighted flux.

The aforementioned studies are limited by their reliance on proton-transfer reaction mass spectrometry (PTRMS) alone to characterize total ecosystem VOC fluxes. PTRMS measures a wide but incomplete suite of VOCs; the technique has been shown to capture a large portion of gas-phase VOC carbon (VOC-C) and associated OH reactivity over forests (Hunter et al., 2017), but it misses more oxidized VOCs, organic nitrates, organosulfur compounds, and other species that can undergo bidirectional surface-atmosphere exchange. Field deployable negative-ion chemical ionization mass spectrometry (CIMS) methods (e.g., using iodide, I^-; acetate, CH_3COO^-; or trifluoromethanolate, CF_3O^- ions) can detect molecules not present in the PTRMS spectrum (Beaver et al., 2012; Bertram et al., 2011; Lee et al., 2014; Mattila et al., 2018), thereby better constraining the speciation, direction, and magnitude of total VOC fluxes when paired with PTRMS measurements.

Here we present the most comprehensive ecosystem-scale VOC flux measurements to date, obtained by applying the eddy covariance (EC) technique to spectra collected simultaneously using dual high-resolution time-of-flight mass spectrometers (PTRMS and ICIMS). Measurements were collected over a ponderosa pine plantation and provide a detailed and novel characterization of bidirectional fluxes across the two mass spectra encompassing hydrocarbons, low-to-mid molecular weight oxygenated VOCs, N-containing species, and halogenated species. Detected species are expected to cover the majority of gas-phase VOC-C and associated OH reactivity undergoing surface exchange (Hunter et al., 2017). We quantify the relative contributions of PTRMS- and ICIMS-detected species to the total net, upward, and downward VOC-C fluxes and interpret the combined observations with the GEOS-Chem CTM to test current understanding of VOC flux drivers and the importance of previously unknown or unmodeled compounds. We further determine the total OH and O_3 reactivity fluxes to better constrain the overall influence of two-way ecosystem VOC fluxes on atmospheric chemistry.

2. Methods

2.1 Measurement Site

The Flux Closure Study 2021 (FluCS 2021) took place from 06 August to 25 September 2021 at the Manitou Experimental Forest (39.1006° N,105.0942° W, ~2370 m elevation) in the Colorado Front Range. Chemical and meteorological observations were made at the Manitou Experimental Forest Observatory (MEFO), a semi-arid mountainous site established by the National Center for Atmospheric Research (NCAR) in 2008 (Ortega et al., 2014). The site is surrounded by an open canopy of primarily ponderosa pine (~15 m height), shrubs, and grassland with a summertime leaf area index of ~1.2 m^2 m^{-2} (Berkelhammer et al., 2016). The area is normally unpolluted but is at times impacted by surrounding cities (e.g., Colorado Springs), suburbs, and wildfires. The MEFO site has been previously used for EC studies of 2-methyl-3-buten-2-ol (232-MBO) and isoprene (Thomas Karl et al., 2014), small organic acids (Fulgham et al., 2019), and other oxygenated VOCs (Kaser et al., 2013a; S. Kim et al., 2010). Other detailed atmospheric chemistry studies at MEFO have primarily focused on reactive carbon abundance and chemistry (Karl et al., 2012; Kaser et al., 2013b; Link et al., 2021; Wolfe et al., 2014; Zhou et al., 2015).

FluCS 2021 included ambient observations of VOCs, NO_x, O_3, CO, and OH reactivity from a 28 m walk-up tower, along with HONO and HO_x radical measurements near the tower base. The tower-based PTRMS and ICIMS measurements are described in the following section. VOC speciation was characterized via offline thermal desorption gas chromatography mass spectrometry (GC-MS) analysis of sorbent tubes that sampled ambient air as well as ponderosa pine and understory emissions using a portable photosynthesis system (PPS; LI-6800, LI-COR Biosciences) (Riches et al., 2020) (**S1.1**). A high-resolution aerosol mass spectrometer (HR-AMS; Aerodyne Research, Inc.) sampling 4.5 m above the ground at the instrument building measured submicron nonrefractory aerosol mass and composition (**S1.2**) (Canagaratna et al., 2015; DeCarlo et al., 2006).

Tower sampling employed custom built, identical PFA inlets (I.D. 0.375”, length 45 m) held at 45 °C to minimize wall interactions and avoid water condensation. These inlets were installed at six heights (3.2, 6.9, 10.6, 14.6, 19.8, and 27.8 m) and oriented at 200° into the prevailing wind. 3D winds and temperature were recorded at 10 Hz from 6.9, 14.6, and 27.8 m using sonic anemometers (CSAT 3B, Campbell Scientific) collocated with the corresponding inlets. Inlets with sonic anemometers were mounted on 1.8 m booms to avoid wind modulation by the tower structure; remaining inlets were mounted on 0.9 m booms. A photosynthetically active radiation (PAR) sensor (MQ-100x, Apogee Instruments) positioned on the ground ~20 m in front of the sonic anemometers recorded half hourly photosynthetic photon flux densities (PPFD). **Fig. S1** summarizes the meteorological observations collected during FluCS 2021.

2.2 VOC measurements

VOCs were measured simultaneously using two high-resolution time-of-flight mass spectrometers housed in an air-conditioned trailer at the tower base. Both instruments employed the same custom-built automated sampling manifold to cycle through the six tower inlets every hour. The measurement sequence was offset between the two instruments and included 30 minutes of sampling from 27.8 m (for EC fluxes) followed by 5 minutes of sampling from each of the remaining inlets (for concentration gradients) and a 5 minute zero. Two rotary vane pumps (Model 1023, Gast Manufacturing) were used for sampling, with one dedicated to the 27.8 m inlet (35 standard liters per minute; SLPM) and one backing the remaining 5 inlets (10-15 SLPM each).

Continuous airflow was maintained through all six inlets to reduce surface adhesion. All wetted sampling surfaces upstream of the PTRMS and ICIMS were composed of PFA to avoid surface-catalyzed reactions of ambient compounds.

2.2.1 PTRMS Operation, Calibrations, and Data Processing

The PTRMS (PTR-QiTOF, Ionicon Analytik) time-of-flight analyzer collected ions (m/z 0-351) with a 33.2 μs extraction period; the resulting spectra were coadded to obtain results at 10 Hz. The mass axis was continuously calibrated using peaks for water vapor (m/z 21.022, $H_3{}^{18}O^+$), acetone (m/z 59.049, $C_3H_7O^+$), and an internal diiodobenzene standard (m/z 203.943, $C_6H_5I^+$ and m/z 330.848, $C_6H_5I_2{}^+$). The drift tube was held at 2.9 mbar, 80 °C, and 740 V to maintain E/N = 136 Townsend (Td). The overall operating conditions led to sensitivities and mass resolutions of 2400 cps/ppb (cps counts per second) and 4200 Δm/m for acetone, and of 850 cps/ppb and 4100 Δm/m for β-pinene. PTRMS subsampling details are outlined in **S1.3**.

The PTRMS was zeroed for 5 minutes hourly by passing sampled air through a platinum bead catalyst (3.2 mm diameter; Shimadzu Corp.) heated to 400 °C. Calibrations were performed once daily for 45 minutes between 00:00-03:00 Mountain Daylight Time (MDT) while the PTRMS was sampling from 27.8 m, with uninterrupted sampling of nocturnal gradients on the other inlets. Four-point calibration curves were collected for 27 VOCs via dynamic dilution of compressed ppm-level gas-phase standards into zero air (Apel-Reimer Environmental; **Table S1**). Laboratory calibrations were performed post-study for individual monoterpene (MT) isomers and for oxygenated terpenoids using aspirated cyclohexane solutions (**S2.1**; **Fig. S2-S3**). Formaldehyde (HCHO) calibrations were also performed post-study using a compressed standard, and the HCHO signal was corrected for methanol interference (**S2.2**; **Fig. S4**). Ambient isoprene concentrations and fluxes were derived by removing the 232-MBO contribution to measured signals at m/z 69.069 (**S2.2**). All signals were normalized to 2×10^5 cps of $H_3{}^{18}O^+$.

The total sesquiterpene (ΣSQT; $C_{15}H_{25}^+$, m/z 205.195) signal was calibrated on the last study day using a compressed β-caryophyllene standard. We apply the β-pinene sensitivity to the total monoterpene (ΣMT; $C_{10}H_{17}^+$, m/z 137.133) signal as this compound had the median sensitivity across all MT isomers identified with the offline GC-MS measurements. Sensitivities for other MT isomers were within 30% of β-pinene (**Fig. S2**). Uncalibrated VOCs employ the measured sensitivity for methacrolein (~1100 ncps/ppb), which had the median sensitivity and humidity dependence across all calibrated compounds. We then apply the second lowest and highest measured sensitivities for all VOCs (275-3000 ncps ppb^{-1}) to derive lower and upper uncertainty bounds for the sum of uncalibrated species.

Humidity corrections were derived on the last study day by diluting VOC standards into zero air with varying water vapor concentrations (LI-610 Portable Dew Point Generator, LI-COR Biosciences). Water vapor concentrations were determined from the ratio of $H_2O{\cdot}H_3O^+$ (m/z 37.028) to $H_3{}^{18}O^+$, scaled by isotopic abundance: $(H_2O{\cdot}H_3O^+)/(500 \times H_3{}^{18}O^+)$. Values of this ratio ranged from 0.003 – 0.05 during the study. Calibration curves were collected at dew points ranging from -10 to 15 ^oC ($(H_2O{\cdot}H_3O^+)/(500 \times H_3{}^{18}O^+) = 0.002 – 0.2$), with the resulting sensitivity vs. water signal fits used to humidity-correct the field data. These corrections led to only modest (typically <15%) changes in the derived calibrations.

Peak fitting and integration were performed using the Ionicon Data Analyzer v 1.0.0.2 (IDA; Ionicon Analytik) (Müller et al., 2013). A custom table of 1340 peaks for m/z 13-351 was generated from this dataset, with 56 days of continuous 10 Hz data then fitted and integrated in one week on a standard workstation. Of the 1340 ions, 776 species were identified using PTRwid (Holzinger, 2015) and the molecular formula assignment workflow used in Millet et al. (2018). All subsequent data processing was performed in MATLAB (R2021a, MathWorks).

2.2.2 ICIMS Operation, Calibrations, and Data Processing

The ICIMS (Bertram et al., 2011; Brophy & Farmer, 2015) sampled at 5 Hz resolution, measuring ions of mass range m/z 2-491 with an extraction frequency of 40 µs. During measurement, the instrument pulls 1.9 SLPM of ambient air into the ion molecule reactor (IMR) where it mixed with 1.3 SLPM of humidified ultra-high N_2 humidified to 85% (to reduce the instrument water dependence) and 1.0 SLPM of I^- ions in ultrahigh purity N_2, both introduced directly into the IMR. The IMR was held at ambient temperature and 100 mbar pressure. The ICIMS was zeroed for one minute every hour via N_2 overflow, followed by external standard calibrations of C_1-C_5 alkanoic acids via permeation tube over the subsequent four minutes. Tofware (v3.2.0, Aerodyne Research, Inc.) fit the mass spectra to the 578 selected ions, and integrated peak areas. The final reported peaklist (485 analyte ions) used for the data analysis herein was limited to include only organic compounds containing C, H, N, and O. We normalize all ICIMS signal to the average sum of I^- and $I\cdot H_2O^-$ during instrument zeros (~1.4×10^6 cps). The mass resolution and sensitivity for formic acid (CH_2O_2) were 3500 Δm/m and 7.29 ncps ppt^{-1}, respectively. We estimate sensitivities for uncalibrated species using the log-linear dependence of instrument sensitivity on the gradient in voltages (dV) between adjacent ion optics within the ICIMS that controls collisionally-induced dissociation of I^- adducts (Lopez-Hilfiker et al., 2015). We determined the half-maximum of a sigmoidal fit of dV vs. analyte signal (dV_{50}) for a suite of calibrants to quantify the relationship between sensitivity and dV_{50} (**Fig. S5**), which was then applied to field-determined dV_{50} values for uncalibrated species across the ICIMS spectrum (**S1.4**) (Bi et al., 2021; Iyer et al., 2016; Lopez-Hilfiker et al., 2014; Mattila et al., 2020). Errors in sigmoidal fits were propagated to derive sensitivity uncertainties for uncalibrated ICIMS species.

There was some overlap in species coverage between the PTRMS and ICIMS, including for several organic acids; in these cases, results were employed from a single instrument based on superior flux signal-to-noise and/or availability of in-field calibrations.

2.4 Flux calculations

EC fluxes were calculated from the covariance of concentration (*X*) with vertical wind (*w*) for an ensemble of *n* measurements (Stull, 1988) within a 30-minute period:

$$F_C = \overline{w'X'} = \frac{1}{n}\sum_{i=1}^{n}(w_i - \overline{w})(X_i - \bar{X}) \quad \textbf{(E1)}$$

Fluxes were derived based on the native PTRMS and ICIMS sampling frequencies of 10- and 5-Hz, respectively. Concentrations and winds were first despiked using the median absolute deviation method (Mauder et al., 2013) and detrended by subtracting a linear fit to each 30-minute signal time series. Winds underwent double rotation so that $\overline{w} = 0$ for each averaging period (X. Lee et al., 2005). The time lag between the sonic wind measurements and the corresponding VOC detection within the mass spectrometer was quantified from the maximum *w*-*X* cross-covariance. Lag times derived in this way for ΣMT and formic acid (HCOOH) were employed for all PTRMS and ICIMS compounds, respectively (**Fig. S6**), due to the high flux signal-to-noise in each case.

Flux uncertainties were determined for each averaging period as 1.96× the standard deviation of the outer 30 points within a 600-point lag time window centered around the peak in *w*-*X* cross-covariance. The resulting flux uncertainties averaged 16%, 21%, and 8% for 232-MBO, ΣMT, and HCOOH, respectively. Species whose mean fluxes were lower than their uncertainty calculated in this way were removed from the following analyses. Sensitivity tests described later assess how the inclusion versus exclusion of these compounds affects our overall findings. Additional recommended EC filtering criteria were applied based on wind shear and stationarity (**S3**) (Foken & Wichura, 1996).

Figure S7 shows examples of frequency-normalized cospectra for VOCs measured by PTRMS and by ICIMS as well as for sensible heat. High frequency attenuation through the sampling line was estimated for each VOC using the empirical model of Horst (1997) (**S4**), resulting in cumulative corrections of 8.2% and 43%, respectively, for the total upward and downward fluxes, and a 5.5% correction for the net flux (**Fig. S8**).

2.5 Model runs

Model simulations for the study period were performed using GEOS-Chem v13.3.0 (https://geos-chem.org/). The model uses assimilated meteorological data (Goddard Earth Observation System

Forward Processing product; GEOS-FP) from the NASA Global Modeling and Assimilation Office (GMAO), which have native horizontal resolution of 0.25° × 0.3125°, 72 vertical layers, 3-h temporal resolution for 3-D meteorological parameters, and 1-h resolution for surface quantities and mixing depths. We performed a nested, full-chemistry simulation at 0.25° × 0.3125° using the FlexGrid functionality for 06 July to 01 October 2021 within a custom domain surrounding MEFO (±3° latitude and longitude). Boundary conditions were taken from a 2° × 2.5° global model run for the same time period that was itself initialized using output from a year-long global simulation at 4° × 5°. Nested simulations employed 5 and 10 min timesteps for transport and chemistry, respectively, while global simulations used 15 and 30 min timesteps (Philip et al., 2016).

The full-chemistry GEOS-Chem chemical mechanism used here features comprehensive HO_x-NO_x-O_x-VOC-Br-Cl-I chemistry coupled to aerosols and incorporates the most recent JPL/IUPAC recommendations. GEOS-Chem v13 also incorporates recent chemical updates for isoprene oxidation (Bates & Jacob, 2019), small oxygenated VOCs (Bates et al., 2021; Chen et al., 2019), halogens (Wang et al., 2019), and small alkyl nitrates (Fisher et al., 2018). For the present analysis we added simplified oxidation schemes for 232-MBO, ∑SQT, and >C2 organic acids (lumped as RCOOH and treated as propanoic acid) to the chemical mechanism (**Table S2**), with RCOOH dry deposition also included (**Table S3**) using a Henry's law constant for propanoic acid from Sander (2015). Rate coefficients for the updated mechanisms are taken from the Master Chemical Mechanism (Saunders et al., 2003) and product yields from published laboratory studies (Fantechi et al., 1998; Ferronato et al., 1998).

Land cover in the 0.25° × 0.3125° model grid cell containing the MEFO site is heterogenous, with 6 Community Land Model (CLM) classifications and cropland plus bare ground accounting for 46% of the total area. This is not representative of the 1 × 1 km^2 measurement footprint, which primarily consists of ponderosa pine, grass, and shrubs (**Fig S9-S10**). We therefore modified the model land cover and leaf area to more realistically reflect the MEFO site as described in **S5** (Byrne et al., 2005; Guenther et al., 2006; Olson et al., 2001).

Model emissions use the Harmonized Emissions Component module version v3 (HEMCO v3) (Lin et al., 2021), with biogenic emissions from terrestrial plants computed online using the Model of Emissions of Gases from Nature (Guenther et al., 2012) as implemented in GEOS-Chem by Hu et al. (2015). For simulations here we implemented 232-MBO and ∑SQT emissions and updated the plant species-specific basal emissions for all VOC to the latest available MEGAN values (MEGAN v3.2; Guenther et al., 2020) within the nested domain. Global anthropogenic emissions are from the Community Emissions Data Systems (CEDS, year-2019) inventory (Hoesly et al., 2018) and biomass burning emissions from the Global Fire Emissions Database v4 (GFED4, year-2019) (Giglio et al., 2013).

In analyses that follow, cumulative model fluxes are calculated by summing the simulated emissions, dry deposition, and net chemical production/loss scaled to the height of the first model layer (**Fig. S11**). The net chemical production/loss is then the average of two limiting cases where either all or none of the production/loss in this grid cell occurs below our sensor.

3. Results and Discussion

3.1 Contributions to VOC carbon flux

Many species contributed to the measured VOC-C fluxes over the sampled ecosystem. Of the 744 PTRMS and 485 ICIMS ions identified as VOCs, 230 and 85 had detectable fluxes, respectively, based on an S/N threshold of 1.96. This drops to 65 (PTRMS) and 25 (ICIMS) when instead using S/N =3 (**Figure S8**). **Figure 1** shows the contribution of individual ions to the total detected VOC-C mass flux. Net fluxes were partitioned into upward and downward components based on the exchange direction for each molecule and averaging period (**Figure 1a**), allowing bidirectional ions to contribute to both upward and downward fractions. **Table S4** shows the top ten contributors to upward and downward VOC-C fluxes, as well as to the reactivity fluxes discussed later.

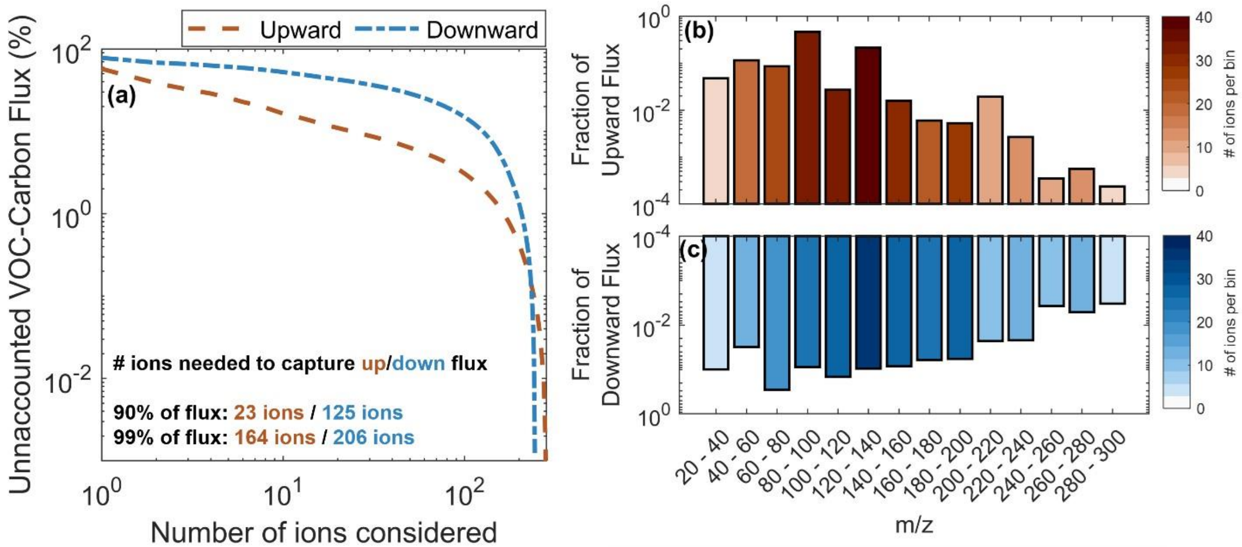

Figure 1: Summary of observed VOC ions undergoing ecosystem-atmosphere exchange. a) Percentage of unaccounted VOC-C upward (orange) and downward (blue) fluxes as a function of the number of ions considered. b) Fractional ion contributions to the total observed upward (top, orange) and downward (bottom, blue) fluxes. Each bin is colored by the number of ions encompassed. 315 total ions with detectable flux are included.

Measured upward VOC-C fluxes at MEFO arise from 283 individual ions, but a large majority of the mass comes from a small number of known species that are commonly simulated in CTMs. 232-MBO (43%) and ΣMT (19%) make up ~60% of the cumulative upward mass flux, with ethanol (C_2H_5OH), methanol (CH_3OH), hydroxyacetone ($C_3H_6O_2$), and isoprene (C_5H_8) contributing an additional 15%. In all, only 23 species account for 90% of the upward VOC-C flux, and these are exclusively hydrocarbons or oxygenated VOC with 3 or fewer oxygen atoms ($n_O \leq 3$). Sesquiterpenes make up 1.7% of the observed upward flux on a carbon basis, but as will be seen later, they make a much larger contribution to the reactivity fluxes. These observations represent one of just a few reported canopy-scale flux datasets for ∑SQT (Fischer et al., 2021; Vermeuel et al., 2022). The remaining 10% of the upward VOC-C flux beyond the 23 dominant compounds is more diverse, with 164 ions needed to capture 99% of the total.

245 total ions had detectable downward fluxes during the campaign. Of these, 125 ions accounted for 90% of the flux—compared to just 23 for the upward fluxes. The two largest contributors to the cumulative downward VOC-C flux were $C_3H_6O_2$ (22%) and HCHO (9.8%). Other key

contributors included acetic acid ($C_2H_4O_2$), other likely organic acids (e.g., succinic acid, $C_4H_6O_4$; lactic acid, $C_3H_6O_3$; pyruvic acid, $C_3H_4O_3$), anhydrides (maleic anhydride, $C_2H_4O_3$; acetic anhydride, $C_4H_6O_3$), and isoprene oxidation products (ISOPOOH/IEPOX, $C_5H_{10}O_3$; IEPOX oxidation product, $C_4H_8O_3$; hydroxymethyl-methyl-a-lactone (HMML), $C_4H_6O_4$; MVK hydroperoxy-carbonyl (MVKPC), $C_4H_6O_3$; isoprene nitrate, $C_5H_9NO_4$). A total of 206 ions are needed to capture 99% of the downward flux. Overall, we see that the total downward VOC-C fluxes are controlled by a far larger set of species than is the case for the upward fluxes, which agrees with findings from Millet et al. (2018) over a mixed temperate forest.

In the following sections (**3.2** and **3.3**) we compare the aggregated VOC fluxes with those predicted by the GEOS-Chem CTM. We then examine the key environmental and chemical drivers of flux variability and of the associated model biases (**3.4**).

3.2 Total upward VOC-C fluxes are well-simulated by GEOS-Chem but downward fluxes are not

Figure 2 compares the total measured and modeled VOC-C fluxes. The observed net and upward VOC-C fluxes are broadly captured by the model, which exhibits a small positive bias (21-32% for the campaign as a whole) in both cases that exceeds the statistical and calibration uncertainties shown in **Fig. 2.** We see that the net observed fluxes (mean $F_{C,net,obs.} = 2.5 \times 10^{12}$ atoms C cm^{-2} s^{-1}) are controlled by and nearly equal to the upward fluxes ($F_{C,up,obs} = 2.8 \times 10^{12}$ atoms C cm^{-2} s^{-1}), revealing this to be a primarily emitting ecosystem—and this feature is also well-represented by the model ($F_{C,net,mod} = 3.3 \times 10^{12}$ atoms C cm^{-2} s^{-1} versus $F_{C,up,mod} = 3.4 \times 10^{12}$ atoms C cm^{-2} s^{-1}). Two daytime peaks are observed in the net and upward flux diel profiles (**Fig. 2d-e**): one between 08:00 and 11:00 MDT that is missing from the model, and one between 12:00 and 15:00 MDT. The morning peak is a consequence of a diurnal mountain-valley flow pattern previously documented at this site (Ortega et al., 2014) (**S6**, **Fig. S12)** while the afternoon peak arises from the temperature and light dependence of VOC emissions.

The GEOS-Chem model successfully represents ~50% of the day-to-day upward flux variability seen in the observations (slope = 1.3; r^2 = 0.48 for the daytime means). This demonstrates some fidelity at reproducing the environmental drivers of VOC-C emissions but leaves over half the day-to-day variability unresolved. The model also exhibits a systematic and sustained terpenoid flux underestimate from 2-7 September during intense rains (**Fig. S13**), and this is discussed further in **Section 3.4**.

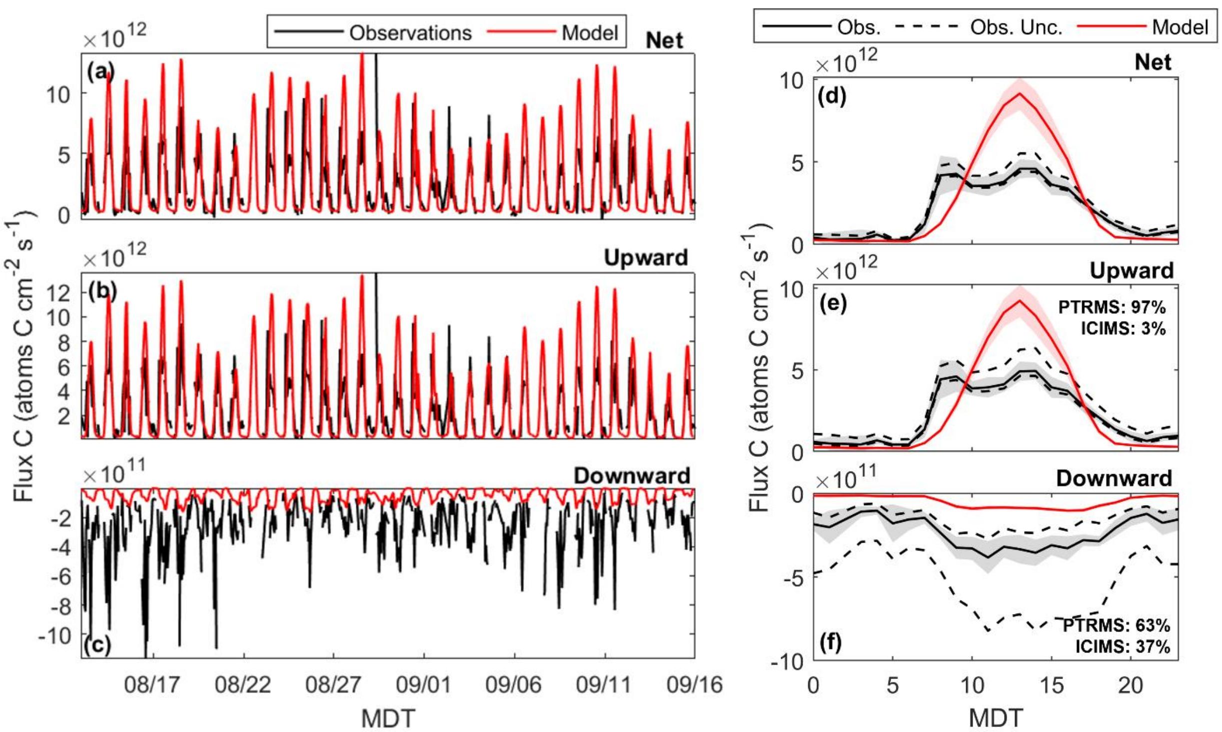

Figure 2: Summary of observed and modeled VOC-C fluxes. a-c) Observed (black) and modeled (red) net, upward, and downward VOC-carbon fluxes. d-f) Corresponding mean diel flux profiles. Shaded regions show 95% confidence intervals. Dashed lines indicate the upper and lower calibration uncertainties. Percentages of the total flux captured by the PTRMS and ICIMS are displayed inset.

The model has far less success at predicting the downward VOC-C fluxes, with a negative model bias that averages more than a factor of four (mean $F_{C,down,mod.}$ = -6.2 x 10^{10} atoms C cm^{-2} s^{-1} versus $F_{C,down,,obs.}$ = -2.6 x 10^{11} atoms C cm^{-2} s^{-1}). Calibration uncertainties (which could increase the observed total by up to 2.5× or decrease it by 1.5×) are insufficient to resolve the disparity. The model also fails to capture any of the observed day-to-day variability in the downward fluxes, with an overall model-measurement r^2 of 0.01 for the daytime means. The observed downward fluxes are greatest during smoky and warm periods (16-19 August, 30 August – 01 September, 07-11 September) when enhanced levels of oxygenated VOCs from advected fire plumes and increased precursor emissions dry deposit to the relatively low-concentration forest canopy below. The model fares significantly worse at representing the downward VOC-C flux variability during these periods (when the two are anti-correlated) compared to the clear sky days ($r^2 = 0.22$). We return to this point in more detail later.

We can explore the causes of the large model $F_{C,down}$ bias by examining the effective deposition velocity ($v_{d,eff.}$) and concentration ($[VOC\text{-}C]_{down}$) for the aggregated species undergoing downward flux ($v_{d,eff.} = F_{C,down} / [VOC\text{-}C]_{down}$). **Figure 3** compares the modeled and observed diel profiles for $v_{d,eff}$ and $[VOC\text{-}C]_{down}$. The modeled and observed diel profile shapes are consistent in each case: $v_{d,\mathrm{eff}}$ peaks with turbulent mixing during daytime whereas $[VOC\text{-}C]_{down}$ shows an afternoon decrease due to oxidative loss. However, the observations reveal sustained deposition through the night when the model predicts near-zero $v_{d,eff}$. This nighttime deposition implies that in-canopy turbulence is sufficient to drive appreciable nonstomatal loss at this time—a process that is absent from the model. Considering both day and night, the model underpredicts both $v_{d,\mathrm{eff}}$ and $[VOC\text{-}C]_{down}$ but the latter disparity is larger (factor of 3.7 for the 24-hour average versus 1.7 for $v_{d,eff}$). While the v_d discrepancy bears further investigation, we conclude that underestimated and missing VOC-C mass is the main driver of the model downward flux bias found here.

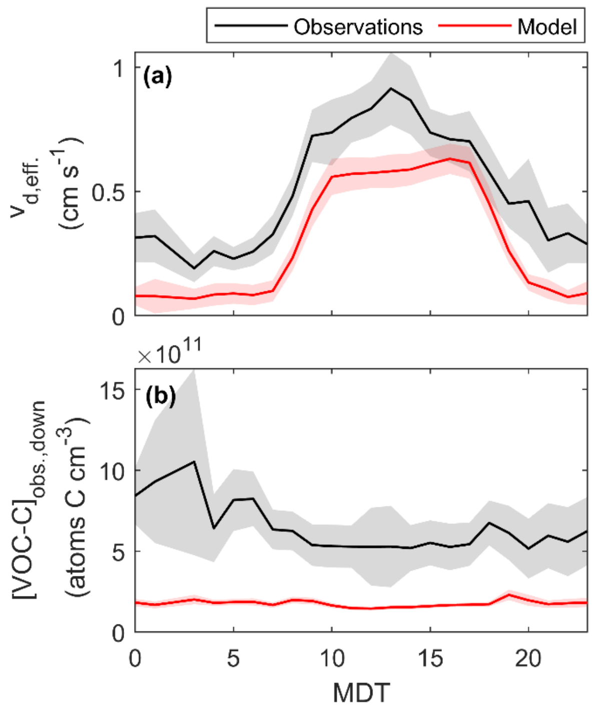

Figure 3: Mean diel profiles for the measured (black) and modeled (red) a) effective deposition velocities ($v_{d,eff}$) and b) concentrations ($[VOC\text{-}C]_{down}$) for all VOCs exhibiting downward fluxes. Shaded areas indicate 95% confidence intervals.

3.3 Total reactivity fluxes are controlled by few, known compounds

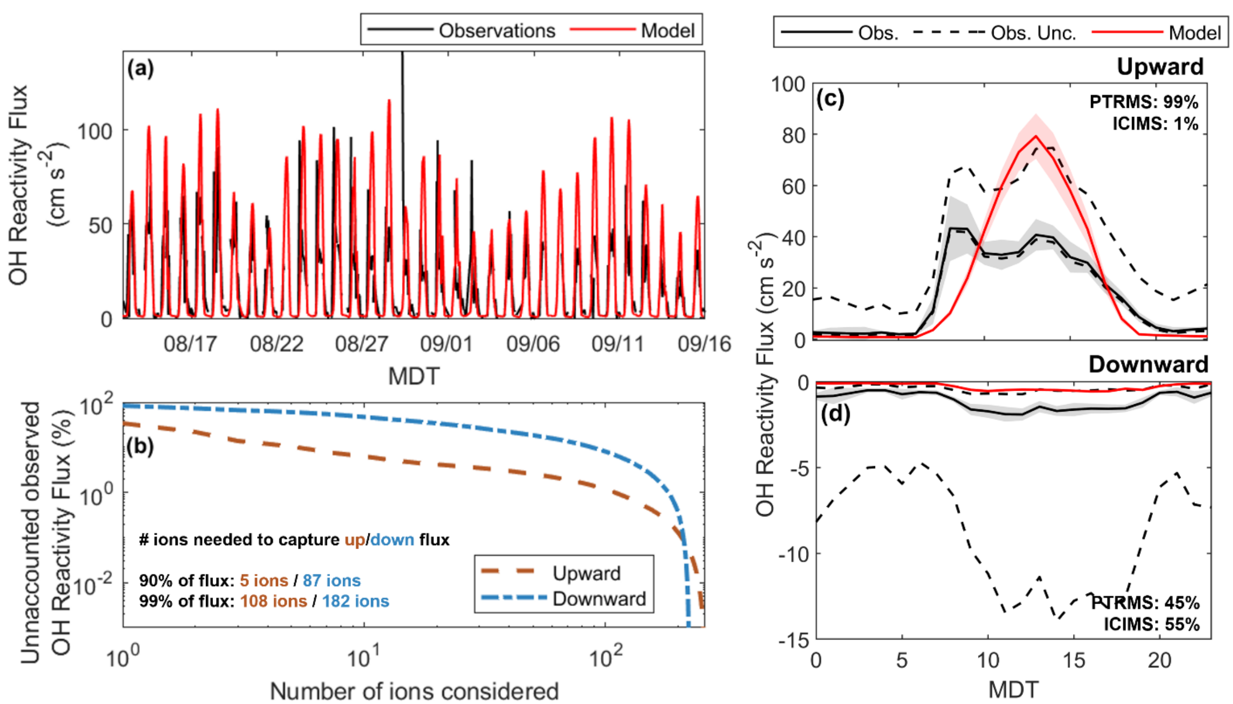

Figure 4: Summary of observed and modeled OH reactivity fluxes. a) Time series of modeled (red) and

observed (black) OH reactivity fluxes (k_{OH+VOC}·F_{VOC}). b) Percentage of unaccounted upward (orange) and downward (blue) OH reactivity flux as a function of the number of ions considered. Mean diel c) upward and d) downward OH reactivity fluxes are also shown. Observed and modeled fluxes are displayed respectively as the solid black and red lines with 95% confidence intervals about the mean. Upper and lower uncertainty bounds associated with VOC calibration and assigned reaction rate coefficients are plotted as the black dashed lines. Percentages of the total reactivity flux captured by the PTRMS and ICIMS are indicated inset.

While the VOC-C fluxes discussed above quantify the exchange of organic mass between the forest canopy and atmosphere, the resulting impact on atmospheric chemistry can be described via the oxidant reactivity fluxes F_{R_Y+VOC} = $\Sigma k_{Y+VOC} \cdot F_{VOC}$. Here, k_{Y+VOC} is the rate coefficient for reaction between a given VOC and an oxidant Y while F_{VOC} is the molar forest-atmosphere flux of that VOC. F_{R_Y+VOC} (cm s^{-2}) is equivalent to the time derivative of reactivity (R_{Y+VOC} = $\Sigma k_{Y+VOC} \cdot X_{VOC}$; s^{-1}), scaled to mixing height ($F_{R_Y+VOC} = h \cdot \frac{dR_{Y+VOC}}{dt}$), and thus directly characterizes the influence of surface fluxes on ambient oxidant reactivity (Millet et al., 2018).

We derive OH and O_3 reactivity fluxes by applying literature rate coefficients to the corresponding measured and modeled VOC fluxes (Atkinson et al., 2006; 1990; Atkinson & Arey, 2003; Chen et al., 2015; Grosjean et al., 1993; Grosjean & Grosjean, 1999; Lee et al., 2006; Reissell et al., 2000; Richters et al., 2015; Stedman & Niki, 1973). For species with known molecular formulae but unknown structure we obtain k_{OH+VOC} using the parameterization introduced by Donahue et al. (2013), and k_{O3+VOC} based on the computed double bond equivalent (DBE) as described in **S7**. A factor of 10 uncertainty in k_{Y+VOC} is estimated for such species by applying the same methodology to all measured species with known structure and k_{Y+VOC}. Further details are provided in **S7** (Chan et al., 2016; Helmig et al., 2007; D. Kim et al., 2011). Total F_{R_Y+VOC} uncertainties are propagated from those in the instrumental sensitivities (as described earlier) and in the assigned *k* values, and are dominated by the latter. Resulting uncertainties for F_{ROH} can change the net, upward, and downward fluxes by up to 55%, 85%, and 8×, respectively. Uncertainties for F_{RO3} can change the net, upward, and downward fluxes by up to 23%, 42%, and 7×.

Figures 4 and 5 summarize the observed and modeled OH and O_3 reactivity fluxes during the study period. In both cases we see a positive model bias of 16-30% in the net reactivity exchange (mean values: $F_{\mathrm{ROH,net}}$ = 27.4 cm s^{-2} versus 21.1 cm s^{-2}, $F_{\mathrm{RO3,net}}$ = 5.0 × 10^{-5} cm s^{-2} versus 4.3 × 10^{-5} cm s^{-2}). Only 5 ions account for over 90% of $F_{\mathrm{ROH,up,obs}}$: 232-MBO (66%), ΣMT (12%), isoprene, ΣSQT, and acetaldehyde. Similarly, only 8 ions account for over 90% of $F_{\mathrm{RO3,up,obs}}$ (**Fig. 5b**) with fluxes in this case primarily driven by ∑SQT (73%) and ΣMT (10%), followed by 232-MBO, isoprene, and butene. Many more ions are required to capture $F_{\mathrm{ROH,down,obs.}}$ and $F_{\mathrm{RO3,down,obs.}}$ (**Fig. 5c+d; Fig. 6c+d**); however, these fluxes are much smaller than the upward reactivity exchange as these more reactive compounds are primarily lost through chemistry rather than deposition. As with the carbon-based fluxes, the model has far more success at predicting day-to-day variability in the upward than in the downward reactivity exchange ($r^2_{R_{OH,up}}$ = 0.39, $r^2_{R_{OH,down}}$ = 0.07; $r^2_{R_{O3,up}}$ = 0.53; $r^2_{R_{O3,down}}$ = 0.02 for the daytime means). Collectively, these findings mirror those for the VOC-C fluxes, where: 1) $F_{R_Y+VOC,net}$ is primarily controlled by few, commonly measured and modeled emitting species; 2) far more ions are required to capture the downward reactivity fluxes; and 3) the GEOS-Chem model captures the general magnitude and much of the day-to-day variability in the upward fluxes but fails at both for the downward fluxes .

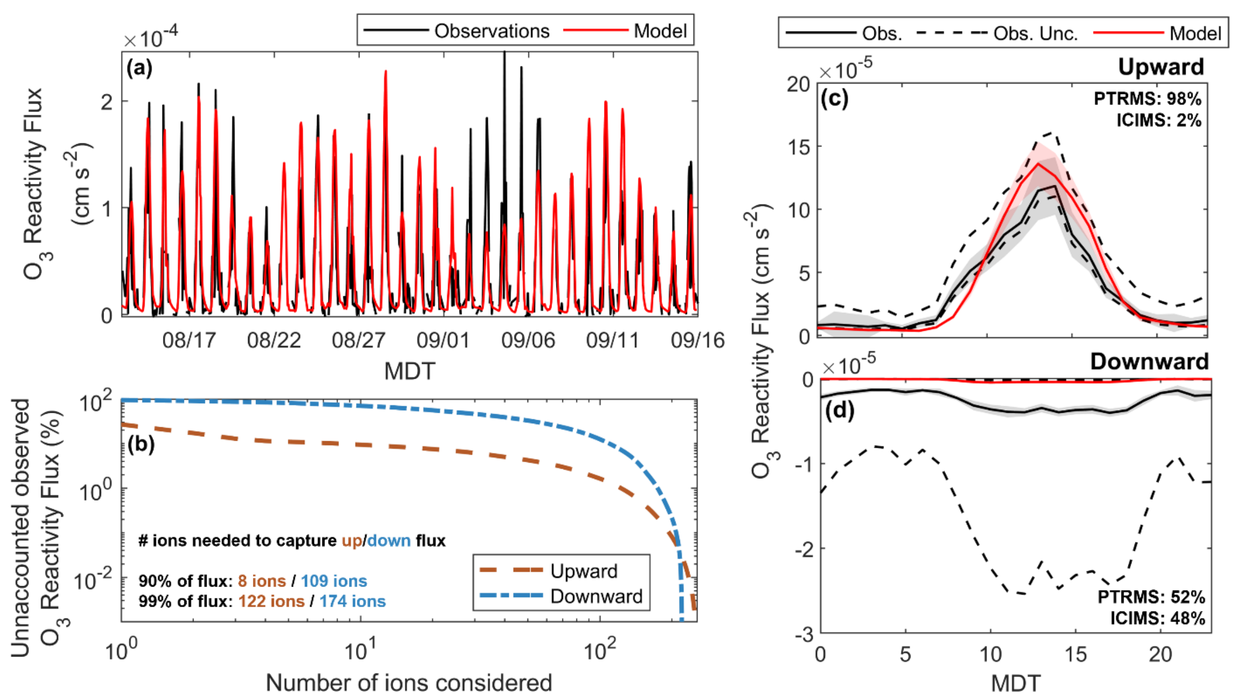

Figure 5: Summary of observed and modeled O_3 reactivity fluxes. a) Time series of modeled (red) and observed (black) O_3 reactivity fluxes ($k_{\mathrm{O3+VOC}} \cdot F_{\mathrm{VOC}}$). b) Percentage of unaccounted upward (orange) and downward (blue) O_3 reactivity flux as a function of the number of ions considered. Mean diel c) upward

and d) downward O_3 reactivity fluxes are also shown. Observed and modeled fluxes are displayed respectively as the solid black and red lines with 95% confidence intervals about the mean. Upper and lower uncertainty bounds associated with VOC calibration and assigned reaction rate coefficients are plotted as the black dashed lines. Percentages of the total reactivity flux captured by the PTRMS and ICIMS are indicated inset.

The above findings highlight some priorities for updating current CTMs. In particular, the standard GEOS-Chem implementation does not feature any explicit chemistry for 232-MBO and ∑SQT; their emissions are only included to compute parameterized yields of acetone and SOA. Our findings here that 232-MBO and ∑SQT respectively account for the bulk of measured OH and O_3 reactivity fluxes demonstrate that this model omission neglects key regional sources of reactivity. We recommend explicit representation of both species in CTMs to reduce such biases and for better predictions of surface-atmosphere exchange and its chemical impacts.

In the following section we discuss the environmental and chemical drivers of flux variability and model-measurement disparities identified above.

3.4 Drivers of flux variability and of model-measurement disparities

3.4.1 Model upward flux biases arise from known species; downward flux biases arise from diverse species

Figure 6 groups the observed and modeled VOC-C fluxes by carbon oxidation state (OS_c) and DBE. DBE estimates the number of double bonds or rings for a given VOC from its molecular formula as DBE = 1 + n_c – n_H/2 + n_N/2, and provides a first-order approximation of reactivity against OH addition or ozonolysis (Pagonis et al., 2019; Yuan et al., 2017). OS_c is computed as $OS_c = 2n_O/n_C - n_H/n_C$ and we use it here as a general marker of oxidation level and volatility (lower OS_c ~ higher volatility) (Isaacman-Vanwertz et al., 2018; Kroll et al., 2011). When there is an assumed nitrate group present ($n_N \geq 1$ and $n_O \geq 3$), OS_C is derived instead as $2n_O/n_C - n_H/n_C + 5n_N/n_C$. Based on these indices, **Figure 6** reveals significantly more chemical diversity in the observations than in the model predictions, with the model missing a large number of species with

DBE ≥ 2 and 2 ≥ OS_c ≥ -2. Below, we discuss how these unrepresented species drive model biases in the carbon and reactivity fluxes.

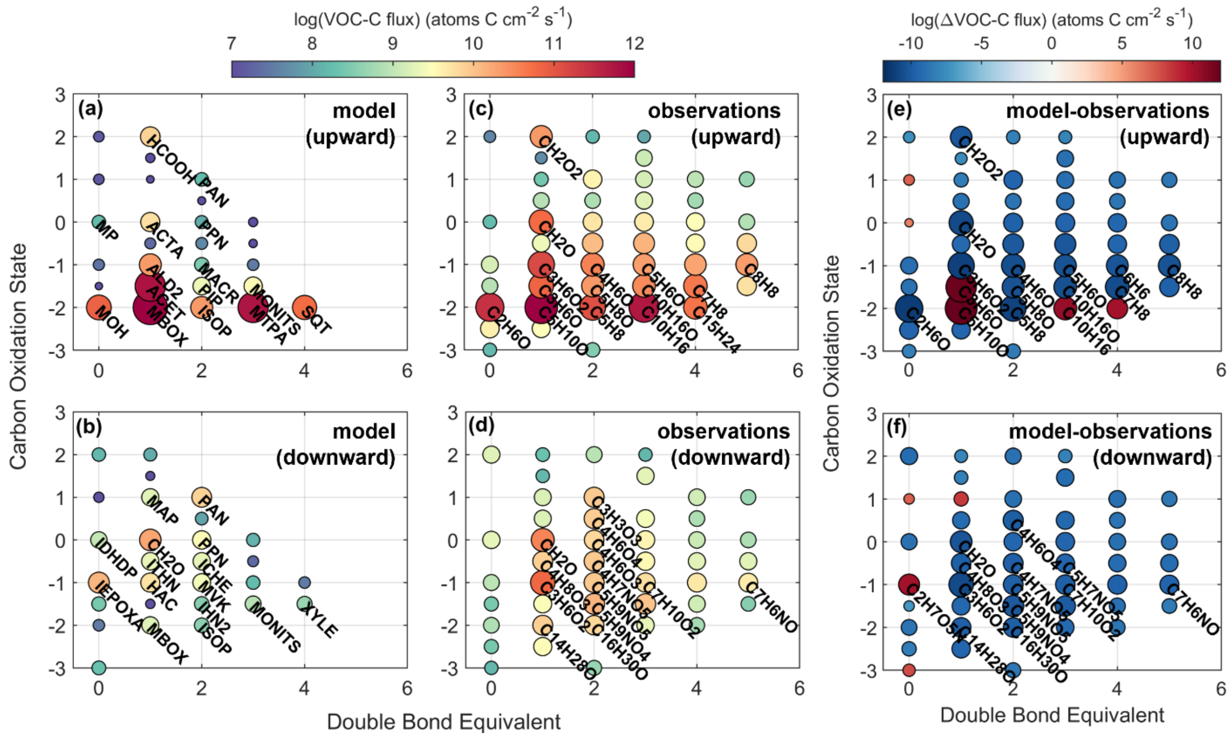

Figure 6: Upward and downward VOC-C fluxes grouped by carbon oxidation state and double bond equivalent. Modeled (a + b) and observed (c + d) fluxes are shown with circles colored and sized by the log of the flux magnitude. Model biases (e + f) are shown with circles colored by the log of the absolute model-measurement flux difference in each case. Circle sizes are proportional to the distance from log(Δflux) = 0. The top contributors to flux or Δflux are labeled on each plot. Names and formulae for GEOS-Chem species are detailed in **Table S5**.

First, we see a lack of species diversity in the predicted upward VOC-C fluxes (**Fig. 6a** versus **Fig. 6c**), with the model placing a higher proportion of the total flux in low-OS_c species. While substantial upward VOC-C fluxes (>10^{10} atoms C cm^{-2} s^{-1}) are observed for species with DBE ≥ 2 and -2 ≤ OS_c ≤ 0 (e.g., monoterpene oxides, $C_{10}H_{16}O$, and potentially unsaturated, oxygen-containing ring structures), these are largely missing from the model (**Fig. 6a**, **6e**). This implies missing emission sources or production routes for intermediate- to low-volatility species in GEOS-Chem.

Despite the above gap, the model nevertheless captures the dominant species controlling the total upward VOC-C flux and nearly all the upward flux bias. Of the 23 compounds making up 90% of the observed upward flux, 15 (85%) are explicitly modeled and the remaining 8 are included as lumped species. Offsetting model errors between these dominant species contribute to the aggregated model-measurement agreement seen in **Fig. 2a**. For example, predictions for 232-MBO and acetone (together 72% of the upward model VOC-C flux) are ~1.6× and ~12× too high, respectively, while those for ethanol, methanol, and isoprene are 3-4× too low. The latter underestimates partly reflect an understory contribution that is not accounted for by the model (**Figure S13**). As with VOC-C, model biases in the upward OH reactivity fluxes (mean $F_{\mathrm{ROH,up}}$ bias = 5.4 cm s^{-2}) arise primarily from known and modeled species—with model overestimates for 232-MBO (+8.0 cm s^{-2}) and ∑MT (+0.2 cm s^{-2}) offset by underestimates for isoprene, acetaldehyde, and other species included in GEOS-Chem (-2.6 cm s^{-2}). Overall, we obtain reasonable model-observation agreement for the upward VOC-C and reactivity fluxes because the model simulates the main species that dominate these fluxes, and because of compensating errors for those species.

Fewer of the species controlling the downward VOC-C fluxes are represented in GEOS-Chem. Explicitly-modeled VOCs (e.g., $C_3H_6O_2$, HCHO, $C_2H_4O_2$) account for only 34% of the observed total, though numerous other species are included in lumped form (e.g., RCOOH, isoprene hydroxynitrates (INP), isoprene nitrates (IHN), and multiple isomers for ISOPOOH and IEPOX). Species completely missing from GEOS-Chem make up ~10% of the measured downward flux; these are chemically diverse, spanning $3 \leq n_C \leq 10$, $2 \leq n_H \leq 15$, and $2 \leq n_O \leq 6$. As with the upward fluxes, we see in the observations a greater contribution from high DBE, high OS_c species than is predicted by the model (**Fig. 6b**, **6d**). These disparities have a greater impact on overall model performance for $F_{C,down}$ because in this case there are not a few, dominant species controlling the overall flux. However, the largest individual model biases are still due to known and modeled VOCs. Together, the explicitly modeled and lumped species (primarily $C_3H_6O_2$, HCHO, $C_5H_9NO_4$) are responsible for a downward flux bias of -1.4×10^{11} atoms C cm^{-2} s^{-1}, compared to -5.8×10^{10} atoms C cm^{-2} s^{-1} for the unmodeled species. The known and modeled VOCs also make up over 85% of the total model $F_{\mathrm{ROH,down}}$ bias (-0.92 cm s^{-2}).

3.4.2 VOC-C flux temperature and light dependence

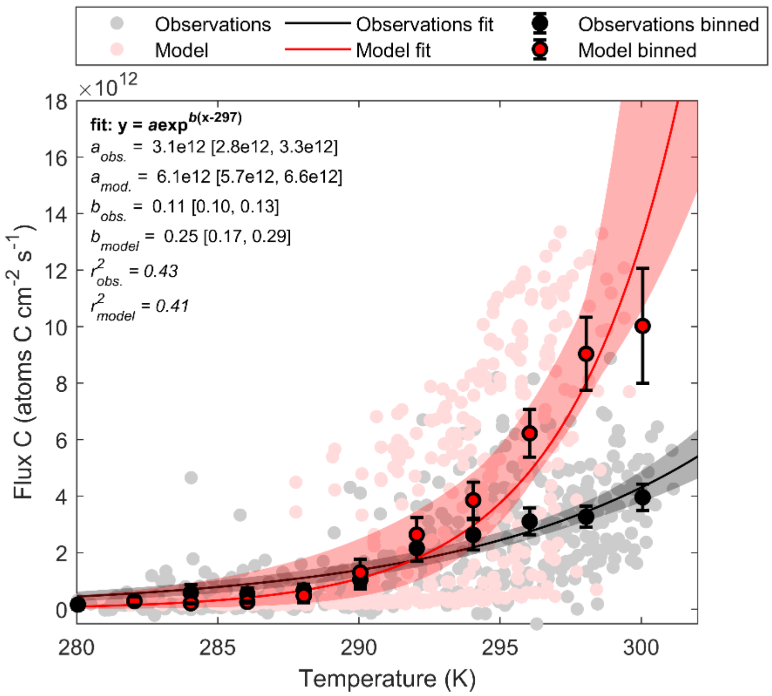

Figure 7: Environmental drivers of total net VOC-C fluxes. Observed (black) and modeled (red) VOC-C fluxes are plotted as a function of temperature. Fitted equations and parameters with associated 95% bootstrapped confidence intervals are shown inset and plotted as the black and red lines. Binned data points are indicated with the 95% confidence intervals about the mean.

We next investigate environmental drivers of the net VOC-C flux variability and model-measurement disparities. We focus in particular on surface temperature and PAR, and exclude data from 08:00-11:00 MDT to avoid the unresolved mountain-valley flow feature discussed earlier (**S6**). **Figure 7** plots the measured and modeled $F_{C,net}$ dependence on surface air temperature (T). Values are fit to $F_{C,net} = a \cdot exp^{b(T-297)}$, where a is the equivalent basal emission rate and b is the effective temperature response factor (K^{-1}) for the aggregated net VOC-C fluxes (A. B. Guenther et al., 2012). The model predicts higher fitted a and b parameters than are observed, explaining the overestimated afternoon peaks in the net and upward fluxes (**Fig. 2**). We saw earlier that the majority of the observed upward fluxes were comprised of directly-emitted VOCs such as 232-MBO, ∑MT, alcohols, and isoprene, and the findings here thus suggest overestimated MEGAN v3.2 emissions factors for these species from ponderosa pine and C3 grasses.

Figure 7 shows that the modeled and observed fluxes have similar temperature dependencies for *T* < 295 K but that the model strongly overpredicts VOC-C fluxes at higher temperatures. This behavior is consistent across all modeled emitting species and for both low and high light levels (**Fig. S14**). The modeled VOC-C flux light dependence is also steeper than suggested by the observations when *T* > 295 K (**Fig. S14**). However, the two relationships are statistically indistinguishable at lower temperatures, indicating that the apparent light-dependence disparity for *T* > 295 K reflects the same temperature-dependence bias shown in **Fig 7**.

3.4.3 Rain and smoke impacts on ecosystem VOC fluxes

Rain and smoke drove large changes in the observed VOC-C and reactivity fluxes and led to the some of the largest model-measurement disparities seen during the study. **Figure 8** summarizes the observed chemical flux anomalies from these periods, which are examined in more detail next. For the following discussion we define rainy days as those with rainfall > 1 mm hr^{-1} and smoky days as those when the observed organic aerosol (OA) mass consistently exceeded 2 μg m^{-3}; remaining days are then denoted as clear-sky periods. The OA mass was confirmed to be primarily fire-derived based on its strong correlation with the biomass burning tracers maleic anhydride ($C_4H_2O_3$), propanenitrile (C_3H_5N), and benzonitrile (C_7H_5N) (Coggon et al., 2019; Gilman et al., 2015) (**Fig. S16**).

Figure 8a shows that rainy periods have strong upward flux enhancements for compounds with DBE ≥ 3 and $OS_c \leq -1$. Specifically, there was an overall enhancement of 61% relative to the clear-sky periods for ΣMT, ΣSQT, monoterpene oxides ($C_{10}H_{16}O$, $C_9H_{14}O$, and $C_{10}H_{14}O$), and species with formulae $C_{10}H_{14}$, C_8H_8, and C_7H_8. Concentration gradient measurements indicate a canopy-level (ponderosa pine) source for all these compounds except ΣSQT, which are also emitted from the understory (**Fig. S15**). Previous studies have reported increased concentrations and emissions of terpenoids and other biogenic VOCs during and after rain at the branch-level (Lamb et al., 1985), above mixed and coniferous forests (Bourtsoukidis et al., 2014; Helmig et al., 1998; Holzinger et al., 2006), and at the MEFO site in particular (Kaser et al., 2013a). The latter study reported a 23× ΣMT flux enhancement during a hailstorm that was accompanied by enhanced emissions of $C_{10}H_{16}O$, $C_{10}H_{14}$, $C_9H_{14}O$, $C_{10}H_{14}O$, C_8H_8, and ΣSQT; the authors invoked mechanical wounding of leaves as a potential cause. Wounding is an unlikely explanation for the rainfall-driven enhancements found here. On the other hand, Schade et al. (1999) documented a positive ∑MT emission dependence on humidity (after rainfall) over a ponderosa pine plantation that they attributed to increased stomatal opening and/or enhanced cuticular permeability. We speculate that such effects are also responsible for the increased VOC emissions observed in our study. Overall, the rain-induced emission enhancements for high DBE, low OS_c compounds indicate a missing source mechanism for reactive terpenoids that should be considered in models over coniferous ecosystems.

In contrast to the terpenoids, all other species exhibited decreased emissions during rainfall due to low temperatures and light levels (**Fig 8a**), leading to a 13% decrease in the aggregated VOC-C upward fluxes on rainy days relative to clear sky days. Wet conditions also allow soluble oxygenated VOCs to partition more effectively to wet surfaces, thus reducing the upward flux component for bidirectional species. The largest emission decreases (>10^{11} atoms C cm^{-2} s^{-1}) were observed for 232-MBO, acetone, ethanol, hydroxyacetone, and acetaldehyde. We also observe decreased downward fluxes during rainfall for many species with higher DBE across a wide OS_c range (**Fig 8b**). These include nitriles, imides, benzoic acid, phenol, and other more hydrophobic compounds that are either fire-derived or photochemically produced and have low concentrations at these times due to reduced upwind emissions.

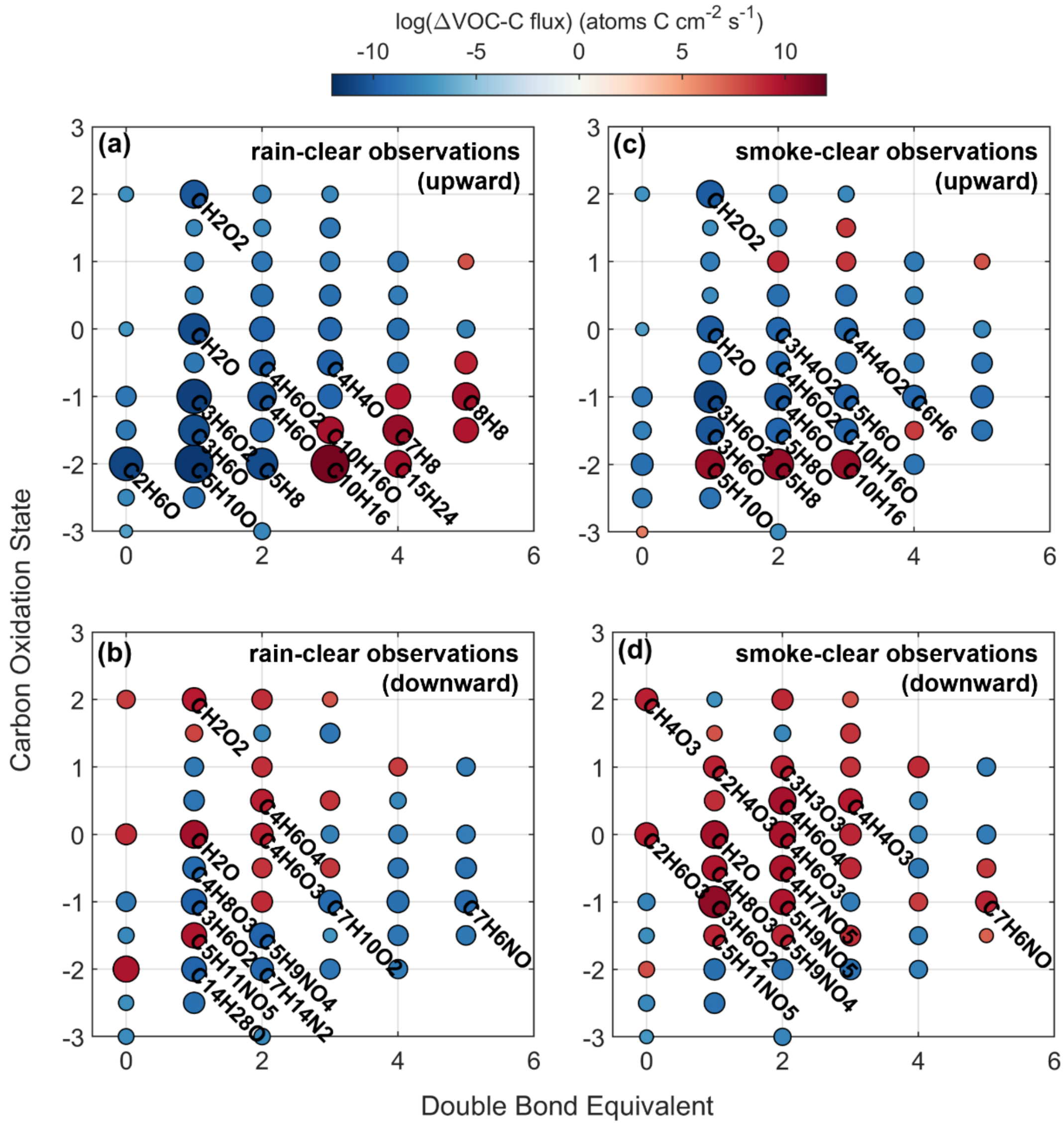

Figure 8: Effects of rain (a, b) and smoke (c, d) on observed upward and downward VOC-C fluxes. The difference in flux magnitude between rainy and clear-sky conditions and between smoky and clear-sky conditions is plotted against carbon oxidation state and double bond equivalent. Circles are colored by the log of the difference in VOC carbon flux magnitudes and sized according to the distance from log(Δflux) = 0. Labeled on each plot are the top contributors to Δflux.

Enhanced upward fluxes of reduced compounds (OS_c = -2; e.g., 232-MBO, isoprene, ΣMT) are observed during smoky days (**Fig. 8c**). This enhancement is only seen for species that are primarily emitted and do not have a strong physical sink, and reflects the higher (by 1.5 °C on average) daytime temperatures on these days relative to the clear days. Meanwhile, oxygenated VOCs that undergo bidirectional exchange, make up a large fraction of the VOC-C mass, and exhibit net emissions on clear days (e.g., acetone, hydroxyacetone, acetaldehyde, HCHO), have their upward fluxes reduced on smoky days due to higher exogeneous concentrations that increase their gross deposition. The warmer temperatures on smoky days also drives a minor change in $F_{ROH,up}$ (of 0.92 cm s^{-2}), largely from isoprene (0.82 cm s^{-2}).

Downward fluxes for many other oxygenated VOCs were enhanced during smoke periods (**Fig. 8d**), in particular for species with DBE ≤ 2 and OS_c ≥ -1. These include acetic acid, >C2 organic acids, anhydrides, a dihydroxycarbonyl compound from IEPOX oxidation ($C_4H_8O_3$) (Bates et al., 2016), isoprene-derived organonitrates ($C_4H_7NO_5$, $C_5H_9NO_4$, $C_5H_9NO_5$) (D'ambro et al., 2017; Tsiligiannis et al., 2022), and hydroxymethyl hydroperoxide (HMHP; CH_4O_3). The >C2 organic acids observed in this study include dicarboxylic acids and ketocarboxylic acids, which are found in smoke aerosol (Kundu et al., 2010) and in SOA generated from ponderosa pine (Tomaz et al., 2018). Species identified here as succinic acid ($C_4H_6O_4$) and acetic anhydride ($C_4H_6O_3$) may also include contributions from hydroxymethyl-methyl-a-lactone (HMML) and MVK hydroperoxyl-carbonyl (MVKPC), respectively, both isoprene oxidation products. Measured isoprene emissions increased during smoke periods, which would increase the abundance of these and other oxidation products. On average, the downward oxygenated VOC-C and OH reactivity fluxes increased by 56% and 49%, respectively, on smoky days.

3.5 Instrumental ion coverage

A novel aspect of this study was the combination of high-resolution PTRMS and ICIMS mass spectra for comprehensive VOC flux characterization over an ecosystem. In this section, we describe the contributions from each instrument to this coverage.

The PTRMS detected 97% of the net upward flux compared to 3% for the ICIMS, with the latter contribution primarily from HCOOH and $C_2H_4O_2$ (**Fig. S17**). Of the 23 top species making up 90% of the upward VOC-C flux, 21 were quantified by PTRMS; the remaining two (HCOOH and

$C_2H_4O_2$) were quantified by both ICIMS and PTRMS. The ICIMS played more of a role for the downward fluxes, capturing 37% of the total, although the PTR-MS still covered the majority (63%). The two largest individual contributors to the downward VOC-C flux ($C_3H_6O_2$ and HCHO; accounting for over 30% of the total) were both detected by PTRMS. The largest downward flux contributors measured by the ICIMS (collectively accounting for 25% of the total) included oxidation products of isoprene and of 232-MBO along with >C2 organic acids.

Meanwhile, the PTRMS captured over 98% of the total upward F_{ROH} and F_{RO3} and therefore a vast majority of the net reactivity flux in both cases. The 5 ions accounting for nearly 90% of $F_{\mathrm{ROH,up,obs}}$ and $F_{\mathrm{RO3,up,obs}}$ were all identified by PTRMS and are commonly reported using this instrument over forest ecosystems. Since the ICIMS detects more soluble oxidized products that undergo efficient deposition, it accounted for a larger share of the downward (55% of $F_{\mathrm{ROH,down,obs}}$ and 48% of $F_{\mathrm{RO3,down,obs}}$) than the upward reactivity fluxes.

In general, we find that the PTRMS detected the hydrocarbons and low molecular weight oxygenated VOCs representing the bulk of the total observed VOC mass and reactivity fluxes. PTRMS measurements can therefore be used alone to provide near-complete coverage of net VOC-C fluxes and their impacts on atmospheric reactivity over this and similar ecosystems. However, ICIMS-detected species made up a significant fraction of the downward VOC fluxes, and therefore provide key information for constraining this major sink of atmospheric reactive carbon. The ICIMS also captured a wide suite of VOC oxidation products for diagnosing the chemical fate of emitted species.

While the combination of PTRMS and ICIMS provides comprehensive observational coverage for VOCs controlling atmospheric reactive carbon abundance and reactivity, the sampling configuration used here would not capture some compounds with very high volatility (e.g., low molecular weight hydrocarbons) or very low volatility (e.g., highly oxygenated organic molecules, HOM). A previous study at this site used relaxed eddy accumulation sampling with gas chromatography-flame ionization detection to quantify summertime emissions of ethene, propene, butene and isoprene (Rhew et al., 2017). Ethene and propene fluxes together averaged ~2 x 10^{11} atoms C cm^{-2} s^{-1}, over an order of magnitude lower than the upward VOC-C fluxes observed in this study, and their associated reactivity fluxes would likewise be small (F_{ROH} ~0.7 cm s^{-2} and F_{RO3} ~4 x 10^{-7} cm s^{-2}). In the case of lower-volatility compounds, Hunter et al. (2017) found that semivolatile and intermediate-volatility organic species not detected by PTRMS or ICIMS accounted for ~10% of the total observed organic carbon concentration at MEFO. Future studies employing atmospheric pressure interface time-of-flight mass spectrometry (Riva et al., 2018) or analogous techniques could help to elucidate the contributions of such species to forest-atmosphere VOC-C exchange.

4. Conclusions

Detailed measurements are needed to understand the two-way flux of VOCs between ecosystems and the atmosphere, the resulting effects on air quality, and how well that exchange is represented in models. This study provided the most comprehensive look yet at terrestrial VOC fluxes by employing two high-resolution mass spectrometers (PTRMS and ICIMS, deployed over a temperate coniferous forest) to calculate EC fluxes across the entire mass spectrum for both instruments. Of the 1261 total ions identified as VOCs, 315 exhibited detectable fluxes; 23 and 125 of these ions were required to capture 90% of the total upward and downward VOC-carbon fluxes, respectively.

Net VOC-C exchange was dominated by the upward fluxes at this site, with PTRMS-detected species accounting for 97% of the total upward flux and 63% of the total downward flux. Comparing the observations to predictions from the GEOS-Chem CTM, we find that the model was able to capture the magnitude and much of the temporal variability in the aggregated net and upward VOC-C fluxes with only modest biases. However, the model underestimated the downward VOC-C fluxes by over a factor of four, primarily due to large concentration underestimates for many relevant oxygenated VOCs. Many of these species were detected by ICIMS, highlighting the need such measurements to fully characterize VOC deposition and fate.

Along with the VOC mass fluxes, OH and O_3 reactivity fluxes were quantified to diagnose the impacts of the measured exchange on atmospheric chemistry. The net OH and O_3 reactivity fluxes (like the mass fluxes) were primarily carried by a small number of emitted species that were detected by the PTRMS and explicitly represented in the GEOS-Chem mechanism. A total of 5 and 108 ions were required to capture 90% of the upward and downward OH reactivity fluxes, respectively, fewer than in the case of the VOC-C fluxes. 232-MBO accounted for ~70% of the OH reactivity flux and should be included in CTMs. Model biases in the simulated OH reactivity fluxes primarily arose from a 232-MBO underestimate and from a missing isoprene source from the forest floor. O_3 reactivity fluxes were dominated by ∑SQT and ∑MT and were overwhelmingly (>98%) composed of PTRMS-measured species. We recommend explicit representation of ∑SQT in CTM mechanisms to correctly represent near-surface O_3 loss.

The GEOS-Chem model was generally successful in simulating the canopy-scale dependence of VOC fluxes on temperature and sunlight for T < 295 K, but strongly overpredicted the flux-temperature sensitivity under hotter conditions. It also failed to capture the enhanced terpenoid emissions that occurred on rainy days. Overall, the main model-measurement disparities identified here were driven by biases for species that are already accounted-for in CTMs rather than by missing species. Better model performance was achieved for the net and upward VOC-C and reactivity fluxes than for the downward fluxes. This is partly because the upward fluxes were dominated by a few major species (all of which have explicit CTM representation), and partly because of offsetting model errors between those major species.

This work has provided a chemically detailed analysis of VOC surface-atmosphere exchange for one pine forest ecosystem, and builds upon a small number of similar studies that relied solely upon PTRMS (Loubet et al., 2022; Millet et al., 2018; Park et al., 2013). Further measurements employing multiple high-resolution mass spectrometers in different ecosystems are required to better understand surface-atmosphere VOC fluxes across the full suite of relevant compounds, diagnose the underlying environmental drivers, and advance the ability of current CTMs to capture the ensuing impact on atmospheric chemistry.

Acknowledgements

This work was supported by NSF AGS 1932771 and 1932849. Measurement capabilities at UMN were also enhanced by support from the Alfred P. Sloan Foundation. The tower used in this project is maintained by NCAR and supported by the USFS. We thank Steven Alton and Paula Fornwalt of USFS for their support with site and logistics. We also thank Glenn M. Wolfe for publicly providing the MATLAB-based FluxToolbox of analysis scripts, portions of which were altered for use in this analysis. Computing resources were provided by the Minnesota Supercomputing Institute (http://www.msi.umn.edu) at the University of Minnesota. We acknowledge that this project occurred on the traditional territory of the Ute and Cheyenne peoples.

Data Availability Statement

Observed and simulated total VOC-C and reactivity fluxes (net, upward, and downward) and associated meteorological observations can be accessed at https://atmoschem.umn.edu/data. This data will be permanently archived with a DOI at https://conservancy.umn.edu/ at the time of publication. GEOS-Chem model code is publicly available at http://www.geos-chem.org. The FluxToolBox code is archived at https://github.com/AirChem.

References

Arneth, A., Schurgers, G., Lathiere, J., Duhl, T., Beerling, D. J., Hewitt, C. N., et al. (2011). Global terrestrial isoprene emission models: Sensitivity to variability in climate and vegetation. *Atmospheric Chemistry and Physics*, *11*(15), 8037–8052. https://doi.org/10.5194/ACP-11-8037-2011

Atkinson, R, Baulch, D. L., Cox, R. A., Crowley, J. N., Hampson, R. F., Hynes, R. G., et al. (2006). Atmospheric Chemistry and Physics Evaluated kinetic and photochemical data for atmospheric chemistry: Volume II-gas phase reactions of organic species The IUPAC Subcommittee on Gas Kinetic Data Evaluation for Atmospheric Chemistry. *Atmos. Chem. Phys*, *6*, 3625–4055. Retrieved from www.atmos-chem-phys.net/6/3625/2006/

Atkinson, R. & Arey, J. (2003). Atmospheric Degradation of Volatile Organic Compounds. *Chemical Reviews*, *103*(12), 4605–4638. https://doi.org/10.1021/CR0206420/ASSET/IMAGES/MEDIUM/CR0206420E00019.GIF

Atkinson, R., Aschmann, S. M., & Arey, J. (1990). Rate constants for the gas-phase reactions of OH and NO3 radicals and O3 with sabinene and camphene at 296±2 K. *Atmospheric Environment Part A, General Topics*, *24*(10), 2647–2654. https://doi.org/10.1016/0960-1686(90)90144-C

Bates, K. H., & Jacob, D. J. (2019). A new model mechanism for atmospheric oxidation of isoprene: Global effects on oxidants, nitrogen oxides, organic products, and secondary organic aerosol. *Atmospheric Chemistry and Physics*, *19*(14), 9613–9640. https://doi.org/10.5194/ACP-19-9613-2019

Bates, K. H., Nguyen, T. B., Teng, A. P., Crounse, J. D., Kjaergaard, H. G., Stoltz, B. M., et al. (2016). Production and Fate of C4 Dihydroxycarbonyl Compounds from Isoprene Oxidation. *Journal of Physical Chemistry A*, *120*(1), 106–117. https://doi.org/10.1021/ACS.JPCA.5B10335/ASSET/IMAGES/LARGE/JP-2015-10335X_0009.JPEG

Bates, K. H., Jacob, D. J., Wang, S., Hornbrook, R. S., Apel, E. C., Kim, M. J., et al. (2021). The Global Budget of Atmospheric Methanol: New Constraints on Secondary, Oceanic, and Terrestrial Sources. *Journal of Geophysical Research: Atmospheres*, *126*(4), e2020JD033439. https://doi.org/10.1029/2020JD033439

Beaver, M. R., St. Clair, J. M., Paulot, F., Spencer, K. M., Crounse, J. D., Lafranchi, B. W., et al. (2012). Importance of biogenic precursors to the budget of organic nitrates: Observations of multifunctional organic nitrates by CIMS and TD-LIF during BEARPEX 2009. *Atmospheric Chemistry and Physics*, *12*(13), 5773–5785. https://doi.org/10.5194/ACP-12-5773-2012

Berkelhammer, M., Noone, D. C., Wong, T. E., Burns, S. P., Knowles, J. F., Kaushik, A., et al. (2016). Convergent approaches to determine an ecosystem's transpiration fraction. *Global Biogeochemical Cycles*, *30*(6), 933–951. https://doi.org/10.1002/2016GB005392

Bertram, T. H., Kimmel, J. R., Crisp, T. a., Ryder, O. S., Yatavelli, R. L. N., Thornton, J. a., et al. (2011). A field-deployable, chemical ionization time-of-flight mass spectrometer. *Atmospheric Measurement Techniques*, *4*(7), 1471–1479. https://doi.org/10.5194/amt-4-1471-2011

Bessagnet, B., Seigneur, C., & Menut, L. (2010). Impact of dry deposition of semi-volatile organic compounds on secondary organic aerosols. *Atmospheric Environment*, *44*, 1781–1787. https://doi.org/10.1016/j.atmosenv.2010.01.027

Bi, C., Krechmer, J. E., Frazier, G. O., Xu, W., Lambe, A. T., Claflin, M. S., et al. (2021). Quantification of isomer-resolved iodide chemical ionization mass spectrometry sensitivity and uncertainty using a voltage-scanning approach. *Atmospheric Measurement Techniques*, *14*(10), 6835–6850. https://doi.org/10.5194/AMT-14-6835-2021

Boucher, O., Randall, D., Artaxo, P., Bretherton, C., Feingold, G., Forster, P., et al. (2013). Climate change 2013: the physical science basis. Contribution of Working Group I to the Fifth Assessment Report of the Intergovernmental Panel on Climate Change. *K., Tignor, M., Allen, SK, Boschung, J., Nauels, A., Xia, Y., Bex, V., and Midgley, PM, Cambridge University Press, Cambridge, UK*.

Bourtsoukidis, E., Williams, J., Kesselmeier, J., Jacobi, S., & Bonn, B. (2014). From emissions to ambient mixing ratios: Online seasonal field measurements of volatile organic compounds over a Norway spruce-dominated forest in central Germany. *Atmospheric Chemistry and Physics*, *14*(13), 6495–6510. https://doi.org/10.5194/acp-14-6495-2014

Brophy, P., & Farmer, D. K. (2015). A switchable reagent ion high resolution time-of-flight chemical ionization mass spectrometer for real-time measurement of gas phase oxidized species: Characterization from the 2013 southern oxidant and aerosol study. *Atmospheric Measurement Techniques*, *8*(7), 2945–2959. https://doi.org/10.5194/AMT-8-2945-2015

Byrne, K. A., Kiely, G., & Leahy, P. (2005). CO2 fluxes in adjacent new and permanent temperate grasslands. *Agricultural and Forest Meteorology*, *135*(1–4), 82–92. https://doi.org/10.1016/J.AGRFORMET.2005.10.005

Canagaratna, M. R., Jimenez, J. L., Kroll, J. H., Chen, Q., Kessler, S. H., Massoli, P., et al. (2015). Elemental ratio measurements of organic compounds using aerosol mass spectrometry: Characterization, improved calibration, and implications. *Atmospheric Chemistry and Physics*, *15*(1), 253–272. https://doi.org/10.5194/ACP-15-253-2015

Chan, A. W. H., Kreisberg, N. M., Hohaus, T., Campuzano-Jost, P., Zhao, Y., Day, D. A., et al. (2016). Speciated measurements of semivolatile and intermediate volatility organic compounds (S/IVOCs) in a pine forest during BEACHON-RoMBAS 2011. *Atmos. Chem. Phys*, *16*, 1187–1205. https://doi.org/10.5194/acp-16-1187-2016

Chen, H., Ren, Y., Cazaunau, M., Daële, V., Hu, Y., Chen, J., & Mellouki, A. (2015). Rate coefficients for the reaction of ozone with 2-and 3-carene. *Chemical Physics Letters*, *621*, 71–77. https://doi.org/10.1016/j.cplett.2014.12.056

Chen, X., Millet, D. B., Singh, H. B., Wisthaler, A., Apel, E. C., Atlas, E. L., et al. (2019). On the sources and sinks of atmospheric VOCs: an integrated analysis of recent aircraft campaigns over North America. *Atmospheric Chemistry and Physics*, *19*(14), 9097–9123. https://doi.org/10.5194/ACP-19-9097-2019

Coggon, M. M., Lim, C. Y., Koss, A. R., Sekimoto, K., Yuan, B., Gilman, J. B., et al. (2019). OH chemistry of non-methane organic gases (NMOGs) emitted from laboratory and ambient biomass burning smoke: Evaluating the influence of furans and oxygenated aromatics on ozone and secondary NMOG formation. *Atmospheric Chemistry and Physics*, *19*(23), 14875–14899. https://doi.org/10.5194/ACP-19-14875-2019

D'ambro, E. L., Lee, B. H., Liu, J., Shilling, J. E., Gaston, C. J., Lopez-Hilfiker, F. D., et al. (2017). Molecular composition and volatility of isoprene photochemical oxidation secondary organic aerosol under low-and high-NO x conditions. *Atmos. Chem. Phys*, *17*, 159–174. https://doi.org/10.5194/acp-17-159-2017

DeCarlo, P. F., Kimmel, J. R., Trimborn, A., Northway, M. J., Jayne, J. T., Aiken, A. C., et al. (2006). Field-deployable, high-resolution, time-of-flight aerosol mass spectrometer. *Analytical Chemistry*, *78*(24), 8281–8289. https://doi.org/10.1021/AC061249N/SUPPL_FILE/AC061249NSI20060905_075156.PDF

Donahue, N. M., Chuang, W., Epstein, S. A., Kroll, J. H., Worsnop, D. R., Robinson, A. L., et al. (2013). Why do organic aerosols exist? Understanding aerosol lifetimes using the two-dimensional volatility basis set. *Environmental Chemistry*, *10*(3), 151–157. https://doi.org/10.1071/EN13022

Fantechi, G., Jensen, N. R., Hjorth, J., & Peeters, J. (1998). Mechanistic studies of the atmospheric oxidation of methyl butenol by OH radicals, ozone and NO3 radicals. *Atmospheric Environment*, *32*(20), 3547–3556. https://doi.org/10.1016/S1352-2310(98)00061-2

Ferronato, C., Orlando, J. J., & Tyndall, G. S. (1998). Rate and mechanism of the reactions of OH and Cl with 2-methyl-3-buten-2-ol. *Journal of Geophysical Research: Atmospheres*, *103*(D19), 25579–25586. https://doi.org/10.1029/98JD00528

Fischer, L., Breitenlechner, M., Canaval, E., Scholz, W., Striednig, M., Graus, M., et al. (2021). First eddy covariance flux measurements of semi-volatile organic compounds with the PTR3-TOF-MS. *Atmospheric Measurement Techniques*, *14*(12), 8019–8039. https://doi.org/10.5194/AMT-14-8019-2021

Fisher, J. A., Atlas, E. L., Barletta, B., Meinardi, S., Blake, D. R., Thompson, C. R., et al. (2018). Methyl, Ethyl, and Propyl Nitrates: Global Distribution and Impacts on Reactive Nitrogen in Remote Marine Environments. *Journal of Geophysical Research: Atmospheres*, *123*(21), 12,429-12,451. https://doi.org/10.1029/2018JD029046

Foken, T., & Wichura, B. (1996). Tools for quality assessment of surface-based flux measurements. *Agricultural and Forest Meteorology*, *78*(1–2), 83–105. https://doi.org/10.1016/0168-1923(95)02248-1

Fulgham, S. R., Brophy, P., Link, M., Ortega, J., Pollack, I., & Farmer, D. K. (2019). Seasonal Flux Measurements over a Colorado Pine Forest Demonstrate a Persistent Source of Organic Acids. *ACS Earth and Space Chemistry*, *3*(9), 2017–2032. research-article. https://doi.org/10.1021/acsearthspacechem.9b00182

Giglio, L., Randerson, J. T., & Van Der Werf, G. R. (2013). Analysis of daily, monthly, and annual burned area using the fourth-generation global fire emissions database (GFED4). *Journal of Geophysical Research: Biogeosciences*, *118*(1), 317–328. https://doi.org/10.1002/JGRG.20042

Gilman, J. B., Lerner, B. M., Kuster, W. C., Goldan, P. D., Warneke, C., Veres, P. R., et al. (2015). Biomass burning emissions and potential air quality impacts of volatile organic compounds and other trace gases from fuels common in the US. *Atmospheric Chemistry and Physics*, *15*(24), 13915–13938. https://doi.org/10.5194/ACP-15-13915-2015

Glasius, M., & Goldstein, A. H. (2016). Recent Discoveries and Future Challenges in Atmospheric Organic Chemistry. *Environmental Science and Technology*, *50*(6), 2754–2764. https://doi.org/10.1021/ACS.EST.5B05105/ASSET/IMAGES/LARGE/ES-2015-051053_0003.JPEG

Goldstein, A. H., & Galbally, I. E. (2007). Known and unexplored organic constituents in the earth's atmosphere. *Environmental Science and Technology*, *41*(5), 1514–1521. https://doi.org/10.1021/es072476p

Grosjean, D., Grosjean, E., & Williams, E. L. (1993). Rate constants for the gas-phase reactions of ozone with unsaturated alcohols, esters, and carbonyls. *International Journal of Chemical Kinetics*, *25*(9), 783–794. https://doi.org/10.1002/KIN.550250909

Grosjean, E., & Grosjean, D. (1999). Rate Constants for the Gas-Phase Reaction of Ozone with Unsaturated Oxygenates. *International Journal of Chemical Kinetics*, *30*, 21–29. https://doi.org/10.1002/(SICI)1097-4601(1998)30:1

Guenther, A., Karl, T., Harley, P., Wiedinmyer, C., Palmer, P. I., & Geron, C. (2006). Estimates of global terrestrial isoprene emissions using MEGAN (Model of Emissions of Gases and Aerosols from Nature). *Atmospheric Chemistry and Physics*, *6*(11), 3181–3210. https://doi.org/10.5194/acp-6-3181-2006

Guenther, A., Jiang, X., Heald, C. L., Sakulyanontvittaya, T., Duhl, T., Emmons, L. K., & Wang, X. (2012). The model of emissions of gases and aerosols from nature version 2.1 (MEGAN2.1): An extended and updated framework for modeling biogenic emissions. *Geoscientific Model Development*, *5*(6), 1471–1492. https://doi.org/10.5194/gmd-5-1471-2012

Guenther, A., Jiang, X., Shah, T., Huang, L., Kemball-Cook, S., & Yarwood, G. (2020). Model of Emissions of Gases and Aerosol from Nature Version 3 (MEGAN3) for Estimating Biogenic Emissions BT - Air Pollution Modeling and its Application XXVI. In C. Mensink, W. Gong, & A. Hakami (Eds.) (pp. 187–192). Cham: Springer International Publishing.

Heikes, B. G. (2002). Atmospheric methanol budget and ocean implication. *Global Biogeochemical Cycles*, *16*(4), 1–13. https://doi.org/10.1029/2002GB001895

Helmig, D., Greenberg, J., Guenther, A., Zimmerman, P., & Geron, C. (1998). Volatile organic compounds and isoprene oxidation products at a temperate deciduous forest site. *Journal of Geophysical Research: Atmospheres*, *103*(D17), 22397–22414. https://doi.org/10.1029/98JD00969

Helmig, D., Ortega, J., Duhl, T., Tanner, D., Guenther, A., Harley, P., et al. (2007). Sesquiterpene emissions from pine trees - Identifications, emission rates and flux estimates for the contiguous United States. *Environmental Science and Technology*, *41*(5), 1545–1553. https://doi.org/10.1021/es0618907

Hoesly, R. M., Smith, S. J., Feng, L., Klimont, Z., Janssens-Maenhout, G., Pitkanen, T., et al. (2018). Historical (1750-2014) anthropogenic emissions of reactive gases and aerosols from the Community Emissions Data System (CEDS). *Geoscientific Model Development*, *11*(1), 369–408. https://doi.org/10.5194/GMD-11-369-2018

Holzinger, R. (2015). PTRwid: A new widget tool for processing PTR-TOF-MS data. *Atmospheric Measurement Techniques*, *8*(9), 3903–3922. https://doi.org/10.5194/AMT-8-3903-2015

Holzinger, R., Lee, A., Mckay, M., & Goldstein, A. H. (2006). *Atmospheric Chemistry and Physics Seasonal variability of monoterpene emission factors for a Ponderosa pine plantation in California*. *Atmos. Chem. Phys* (Vol. 6). Retrieved from www.atmos-chem-phys.net/6/1267/2006/

Hu, L., Millet, D. B., Baasandorj, M., Griffis, T. J., Turner, P., Helmig, D., et al. (2015). Isoprene emissions and impacts over an ecological transition region in the U.S. Upper Midwest inferred from tall tower measurements. *Journal of Geophysical Research: Atmospheres*, *120*(8), 3553–3571. https://doi.org/10.1002/2014JD022732

Huang, G., Brook, R., Crippa, M., Janssens-Maenhout, G., Schieberle, C., Dore, C., et al. (2017). Speciation of anthropogenic emissions of non-methane volatile organic compounds: a global gridded data set for 1970-2012. *Atmospheric Chemistry and Physics Discussions*, 1–36. https://doi.org/10.5194/acp-2017-65

Hunter, J. F., Day, D. A., Palm, B. B., Yatavelli, R. L. N., Chan, A. W. H., Kaser, L., et al. (2017). Comprehensive characterization of atmospheric organic carbon at a forested site. *Nature Geoscience 2017 10:10*, *10*(10), 748–753. https://doi.org/10.1038/ngeo3018

Isaacman-Vanwertz, G., Massoli, P., O'Brien, R., Lim, C., Franklin, J. P., Moss, J. A., et al. (2018). Chemical evolution of atmospheric organic carbon over multiple generations of oxidation. *Nature Chemistry 2018 10:4*, *10*(4), 462–468. https://doi.org/10.1038/s41557-018-0002-2

Iyer, S., Lopez-Hilfiker, F., Lee, B. H., Thornton, J. A., & Kurtén, T. (2016). Modeling the Detection of Organic and Inorganic Compounds Using Iodide-Based Chemical Ionization.

Jacob, D. J., Field, B. D., Jin, E. M., Bey, I., Li, Q., Logan, J. A., et al. (2002). Atmospheric budget of acetone. *Journal of Geophysical Research: Atmospheres*, *107*(9–10). https://doi.org/10.1029/2001jd000694

Karl, T., Hansel, a., Cappellin, L., Kaser, L., Herdlinger-Blatt, I., & Jud, W. (2012). Selective measurements of isoprene and 2-methyl-3-buten-2-ol based on NO^+ ionization mass spectrometry. *Atmospheric Chemistry and Physics*, *12*(24), 11877–11884. https://doi.org/10.5194/acp-12-11877-2012

Karl, T., Kaser, L., & Turnipseed, A. (2014). Eddy covariance measurements of isoprene and 232-MBO based on NO + time-of-flight mass spectrometry. *International Journal of Mass Spectrometry*, *365–366*, 15–19. https://doi.org/10.1016/j.ijms.2013.12.002

Kaser, L., Karl, T., Guenther, A., Graus, M., Schnitzhofer, R., Turnipseed, A., et al. (2013a). Undisturbed and disturbed above canopy ponderosa pine emissions: PTR-TOF-MS measurements and MEGAN 2.1 model results. *Atmospheric Chemistry and Physics*, *13*(23), 11935–11947. https://doi.org/10.5194/acp-13-11935-2013

Kaser, L., Karl, T., Schnitzhofer, R., Graus, M., Herdlinger-Blatt, I. S., DiGangi, J. P., et al. (2013b). Comparison of different real time VOC measurement techniques in a ponderosa pine forest. *Atmospheric Chemistry and Physics*, *13*(5), 2893–2906. https://doi.org/10.5194/acp-13-2893-2013

Kim, D., Stevens, P. S., & Hites, R. A. (2011). Rate constants for the gas-phase reactions of OH and O_3 with β-ocimene,β-myrcene, and α-and β-farnesene as a function of temperature. *Journal of Physical Chemistry A*, *115*(4), 500–506. https://doi.org/10.1021/jp111173s

Kim, S., Karl, T., Guenther, A., Tyndall, G., Orlando, J., Harley, P., et al. (2010). Emissions and ambient distributions of Biogenic Volatile Organic Compounds (BVOC) in a ponderosa pine ecosystem: Interpretation of PTR-MS mass spectra. *Atmospheric Chemistry and Physics*, *10*(4), 1759–1771. https://doi.org/10.5194/acp-10-1759-2010

Kroll, J. H., Donahue, N. M., Jimenez, J. L., Kessler, S. H., Canagaratna, M. R., Wilson, K. R., et al. (2011). Carbon oxidation state as a metric for describing the chemistry of atmospheric organic aerosol. *Nat. Chem.*, *3*(2), 133. https://doi.org/10.1038/nchem.948

Kundu, S., Kawamura, K., Andreae, T. W., Hoffer, A., & Andreae, M. O. (2010). Molecular distributions of dicarboxylic acids, ketocarboxylic acids and α-dicarbonyls in biomass burning aerosols: Implications for photochemical production and degradation in smoke layers. *Atmospheric Chemistry and Physics*, *10*(5), 2209–2225. https://doi.org/10.5194/ACP-10-2209-2010

Lamb, B., Westberg, H., Allwine, G., & Quarles, T. (1985). Biogenic hydrocarbon emissions from deciduous and coniferous trees in the United States. *Journal of Geophysical Research*, *90*, 2380–2390. https://doi.org/10.1029/JD090iD01p02380

Lary, D. J., & Shallcross, D. E. (2000). Central role of carbonyl compounds in atmospheric chemistry. *Journal of Geophysical Research Atmospheres*, *105*(D15), 19771–19778. https://doi.org/10.1029/1999JD901184

Lee, A., Goldstein, A. H., Keywood, M. D., Gao, S., Varutbangkul, V., Bahreini, R., et al. (2006). Gas-phase products and secondary aerosol yields from the ozonolysis of ten different terpenes. *Journal of Geophysical Research Atmospheres*, *111*(7), 1–18. https://doi.org/10.1029/2005JD006437

Lee, B. H., Lopez-hilfiker, F. D., Mohr, C., Kurten, T., Worsnop, D. R., & Joel, A. (2014). An Iodide-Adduct High-Resolution Time-of-Flight Chemical- Ionization Mass Spectrometer: Application to Atmospheric Inorganic and Organic Compounds. *Environ.Sci. Technol.*, *48*, 6309–6317. https://doi.org/10.1021/es500362a

Lee, X., Massman, W. J., & Law, B. (2005). Handbook of Micrometeorology. *Handbook of Micrometeorology*, *29*, 250. Retrieved from https://books.google.com/books/about/Handbook_of_Micrometeorology.html?id=IJ_19RkTfBQC

Lin, H., Jacob, D. J., Lundgren, E. W., Sulprizio, M. P., Keller, C. A., Fritz, T. M., et al. (2021). Harmonized Emissions Component (HEMCO) 3.0 as a versatile emissions component for atmospheric models: Application in the GEOS-Chem, NASA GEOS, WRF-GC, CESM2, NOAA GEFS-Aerosol, and NOAA UFS models. *Geoscientific Model Development*, *14*(9), 5487–5506. https://doi.org/10.5194/GMD-14-5487-2021

Link, M. F., Brophy, P., Fulgham, S. R., Murschell, T., & Farmer, D. K. (2021). Isoprene versus Monoterpenes as Gas-Phase Organic Acid Precursors in the Atmosphere. *ACS Earth and Space Chemistry*, *5*(6), 1600–1612. https://doi.org/10.1021/ACSEARTHSPACECHEM.1C00093/ASSET/IMAGES/LARGE/SP1C00093_0010.JPEG

Lopez-Hilfiker, F. D., Mohr, C., Ehn, M., Rubach, F., Kleist, E., Wildt, J., et al. (2014). A novel method for online analysis of gas and particle composition: Description and evaluation of a filter inlet for gases and AEROsols (FIGAERO). *Atmospheric Measurement Techniques*, *7*(4), 983–1001. https://doi.org/10.5194/AMT-7-983-2014

Lopez-Hilfiker, F. D., Iyer, S., Mohr, C., Lee, B. H., D'Ambro, E. L., Kurtén, T., & Thornton, J. a. (2015). Constraining the sensitivity of iodide adduct chemical ionization mass spectrometry to multifunctional organic molecules using the collision limit and thermodynamic stability of iodide ion adducts. *Atmospheric Measurement Techniques Discussions*, *8*(10), 10875–10896. https://doi.org/10.5194/amtd-8-10875-2015

Loubet, B., Buysse, P., Gonzaga-Gomez, L., Lafouge, F., Ciuraru, R., Decuq, C., et al. (2022). Volatile organic compound fluxes over a winter wheat field by PTR-Qi-TOF-MS and eddy covariance. *Atmospheric Chemistry and Physics*, *22*(4), 2817–2842. https://doi.org/10.5194/ACP-22-2817-2022

Mattila, J. M., Brophy, P., Kirkland, J., Hall, S., Ullmann, K., Fischer, E. V., et al. (2018). Tropospheric sources and sinks of gas-phase acids in the Colorado Front Range. *Atmospheric Chemistry and Physics*, *18*(16), 12315–12327. https://doi.org/10.5194/ACP-18-12315-2018

Mattila, J. M., Lakey, P. S. J., Shiraiwa, M., Wang, C., Abbatt, J. P. D., Arata, C., et al. (2020). Multiphase Chemistry Controls Inorganic Chlorinated and Nitrogenated Compounds in Indoor Air during Bleach Cleaning. *Environmental Science and Technology*, *54*(3), 1730–1739. https://doi.org/10.1021/ACS.EST.9B05767/ASSET/IMAGES/MEDIUM/ES9B05767_M012.GIF

Mauder, M., Cuntz, M., Drüe, C., Graf, A., Rebmann, C., Schmid, H. P., et al. (2013). A strategy for quality and uncertainty assessment of long-term eddy-covariance measurements. *Agricultural and Forest Meteorology*, *169*, 122–135. https://doi.org/10.1016/J.AGRFORMET.2012.09.006

Mellouki, A., Wallington, T. J., & Chen, J. (2015). Atmospheric Chemistry of Oxygenated Volatile Organic Compounds: Impacts on Air Quality and Climate. *Chemical Reviews*, *115*(10), 3984–4014. https://doi.org/10.1021/cr500549n

Millet, D. B., Jacob, D. J., Custer, T. G., De Gouw, J. A., Goldstein, A. H., Karl, T., et al. (2008). New constraints on terrestrial and oceanic sources of atmospheric methanol. *Atmospheric Chemistry and Physics*, *8*(23), 6887–6905. https://doi.org/10.5194/acp-8-6887-2008

Millet, D. B., Baasandorj, M., Farmer, D. K., Thornton, J. A., Baumann, K., Brophy, P., et al. (2015). A large and ubiquitous source of atmospheric formic acid. *Atmospheric Chemistry and Physics*, *15*(11), 6283–6304. https://doi.org/10.5194/acp-15-6283-2015

Millet, D. B., Guenther, A., Siegel, D. A., Nelson, N. B., Singh, H. B., Gouw, J. A. De, et al. (2010). Global atmospheric budget of acetaldehyde : 3-D model analysis and constraints from in-situ and satellite observations. *Atmospheric Chemistry and Physics*, *10*, 3405–3425.

Millet, D. B., Alwe, H. D., Chen, X., Deventer, M. J., Griffis, T. J., Holzinger, R., et al. (2018). Bidirectional Ecosystem-Atmosphere Fluxes of Volatile Organic Compounds Across the Mass Spectrum: How Many Matter? *ACS Earth and Space Chemistry*, *2*(8), 764–777. https://doi.org/10.1021/acsearthspacechem.8b00061

Muller, J.-F., & Brasseur, G. (1999). Source of upper tropospheric HOx: A three-dimensional study. *Journal of Geophysical Research*, *104*, 1705–1715.

Müller, M., Mikoviny, T., Jud, W., D'Anna, B., & Wisthaler, A. (2013). A new software tool for the analysis of high resolution PTR-TOF mass spectra. *Chemometrics and Intelligent Laboratory Systems*, *127*, 158–165. https://doi.org/10.1016/J.CHEMOLAB.2013.06.011

Nguyen, T. B., Crounse, J. D., Teng, A. P., St Clair, J. M., Paulot, F., Wolfe, G. M., & Wennberg, P. O. (2015). Rapid deposition of oxidized biogenic compounds to a temperate forest. *Proceedings of the National Academy of Sciences of the United States of America*, *112*(5), E392-401. https://doi.org/10.1073/pnas.1418702112

Olson, D. M., Dinerstein, E., Wikramanayake, E. D., Burgess, N. D., Powell, G. V. N., Underwood, E. C., et al. (2001). Terrestrial ecoregions of the world: A new map of life on Earth. *BioScience*, *51*(11), 933–938. https://doi.org/10.1641/0006-3568(2001)051[0933:TEOTWA]2.0.CO;2

Ortega, J., Turnipseed, A., Guenther, A. B., Karl, T. G., Day, D. A., Gochis, D., et al. (2014). Overview of the Manitou experimental forest observatory: Site description and selected science results from 2008 to 2013. *Atmospheric Chemistry and Physics*, *14*(12), 6345–6367. https://doi.org/10.5194/acp-14-6345-2014

Pagonis, D., Sekimoto, K., & de Gouw, J. (2019). A Library of Proton-Transfer Reactions of H3O+ Ions Used for Trace Gas Detection. *Journal of the American Society for Mass Spectrometry*, *30*(7), 1330–1335. https://doi.org/10.1007/S13361-019-02209-3/SUPPL_FILE/JS8B06050_SI_001.XLSX

Park, J. H., Goldstein, A. H., Timkovsky, J., Fares, S., Weber, R., Karlik, J., & Holzinger, R. (2013). Active atmosphere-ecosystem exchange of the vast majority of detected volatile organic compounds. *Science*, *341*(6146), 643–647. https://doi.org/10.1126/science.1235053

Philip, S., Martin, R. V., & Keller, C. A. (2016). Sensitivity of chemistry-transport model simulations to the duration of chemical and transport operators: A case study with GEOS-Chem v10-01. *Geoscientific Model Development*, *9*(5), 1683–1695. https://doi.org/10.5194/GMD-9-1683-2016

Reissell, A., Arey, J., & Atkinson, R. (2000). Atmospheric Chemistry of Camphor. *Int J Chem Kinet*, *33*, 56–63. https://doi.org/10.1002/1097-4601

Rhew, R. C., Deventer, M. J., Turnipseed, A. A., Warneke, C., Ortega, J., Shen, S., et al. (2017). Ethene, propene, butene and isoprene emissions from a ponderosa pine forest measured by relaxed eddy accumulation. *Atmospheric Chemistry and Physics*, *17*(21), 13417–13438. https://doi.org/10.5194/acp-17-13417-2017

Riches, M., Lee, D., & Farmer, D. K. (2020). Simultaneous leaf-level measurement of trace gas emissions and photosynthesis with a portable photosynthesis system. *Atmospheric Measurement Techniques*, *13*(8), 4123–4139. https://doi.org/10.5194/AMT-13-4123-2020

Richters, S., Herrmann, H., & Berndt, T. (2015). Gas-phase rate coefficients of the reaction of ozone with four sesquiterpenes at 295 ± 2 K. *Physical Chemistry Chemical Physics*, *17*(17), 11658–11669. https://doi.org/10.1039/c4cp05542j

Riva, M., Rantala, P., Krechmer, J. E., Peräkylä, O., Zhang, Y., Heikkinen, L., et al. (2018). Evaluating the performance of five different chemical ionization techniques for detecting gaseous oxygenated organic species. *Atmospheric Measurement Techniques Discussions*, 1–39. https://doi.org/10.5194/amt-2018-407

Safieddine, S. A., Heald, C. L., & Henderson, B. H. (2017). The global nonmethane reactive organic carbon budget: A modeling perspective. *Geophysical Research Letters*, *44*(8), 3897–3906. https://doi.org/10.1002/2017GL072602

Sander, R. (2015). Compilation of Henry's law constants (version 4.0) for water as solvent. *Atmospheric Chemistry and Physics*, *15*(8), 4399–4981. https://doi.org/10.5194/acp-15-4399-2015

Saunders, S. M., Jenkin, M. E., Derwent, R. G., & Pilling, M. J. (2003). Protocol for the development of the Master Chemical Mechanism, MCM v3 (Part A): Tropospheric degradation of non-aromatic volatile organic compounds. *Atmospheric Chemistry and Physics*, *3*(1), 161–180. https://doi.org/10.5194/acp-3-161-2003

Schade, G. W., Goldstein, A. H., & Lamanna, M. S. (1999). Are Monoterpene Emissions influenced by Humidity? *Geophysical Research Letters*, *26*(14), 2187–2190. https://doi.org/10.1029/1999GL900444

Sindelarova, K., Granier, C., Bouarar, I., Guenther, A., Tilmes, S., Stavrakou, T., et al. (2014). Global data set of biogenic VOC emissions calculated by the MEGAN model over the last 30 years. *Atmospheric Chemistry and Physics*, *14*(17), 9317–9341. https://doi.org/10.5194/acp-14-9317-2014

Singh, H. B., Kanakidou, M., Crutzen, P. J., & Jacob, D. J. (1995). High concentrations and photochemical fate of oxygenated hydrocarbons in the global troposphere. *Nature*, *378*(6552), 50–54. https://doi.org/10.1038/378050a0

Stedman, D. H., & Niki, H. (1973). Ozonolysis Rates of Some Atmospheric Gases. *Http://Dx.Doi.Org/10.1080/00139307309435501*, *4*(4), 303–310. https://doi.org/10.1080/00139307309435501

Stull, R. B. (1988). *An Introduction to Boundary Layer Meteorology*.

Tomaz, S., Cui, T., Chen, Y., Sexton, K. G., Roberts, J. M., Warneke, C., et al. (2018). Photochemical Cloud Processing of Primary Wildfire Emissions as a Potential Source of Secondary Organic Aerosol. *Environmental Science and Technology*, *52*(19), 11027–11037. https://doi.org/10.1021/ACS.EST.8B03293/ASSET/IMAGES/LARGE/ES-2018-032933_0004.JPEG

Tsiligiannis, E., Wu, R., Lee, B. H., Salvador, C. M., Priestley, M., Carlsson, P. T. M., et al. (2022). A Four Carbon Organonitrate as a Significant Product of Secondary Isoprene Chemistry. *Geophysical Research Letters*, *49*(11), e2021GL097366. https://doi.org/10.1029/2021GL097366

Vermeuel, M. P., Novak, G. A., Kilgour, D. B., Claflin, M. S., Lerner, B. M., Trowbridge, A. M., et al. (2022). Observations of biogenic volatile organic compounds over a mixed temperate forest during the summer to autumn transition. *Atmospheric Chemistry and Physics Discussions*. https://doi.org/https://doi.org/10.5194/egusphere-2022-1015

Wang, X., Jacob, D. J., Eastham, S. D., Sulprizio, M. P., Zhu, L., Chen, Q., et al. (2019). The role of chlorine in global tropospheric chemistry. *Atmospheric Chemistry and Physics*, *19*(6), 3981–4003. https://doi.org/10.5194/ACP-19-3981-2019

Wolfe, G. M., Cantrell, C., Kim, S., Mauldin, R. L., Karl, T., Harley, P., et al. (2014). Missing peroxy radical sources within a summertime ponderosa pine forest. *Atmospheric Chemistry and Physics*, *14*(9), 4715–4732. https://doi.org/10.5194/acp-14-4715-2014

Yáñez-Serrano, A. M., Nölscher, A. C., Williams, J., Wolff, S., Alves, E., Martins, G. A., et al. (2015). Diel and seasonal changes of biogenic volatile organic compounds within and above an Amazonian rainforest. *Atmospheric Chemistry and Physics*, *15*(6), 3359–3378. https://doi.org/10.5194/acp-15-3359-2015

Yuan, B., Koss, A. R., Warneke, C., Coggon, M., Sekimoto, K., & De Gouw, J. A. (2017). Proton-Transfer-Reaction Mass Spectrometry: Applications in Atmospheric Sciences. *Chemical Reviews*, *117*(21), 13187–13229. https://doi.org/10.1021/ACS.CHEMREV.7B00325/SUPPL_FILE/CR7B00325_SI_001.PDF

Zhou, L., Gierens, R., Sogachev, A., Mogensen, D., Ortega, J., Smith, J. N., et al. (2015). Contribution from biogenic organic compounds to particle growth during the 2010 BEACHON-ROCS campaign in a Colorado temperate needleleaf forest. *Atmospheric Chemistry and Physics*, *15*(15), 8643–8656. https://doi.org/10.5194/acp-15-8643-2015

Closing the reactive carbon flux budget: Observations from dual mass spectrometers over a coniferous forest

Michael P. Vermeuel[1], Dylan B. Millet[1*,] Delphine K. Farmer[2], Matson A. Pothier[2], Michael F. Link[2^], Mj Riches[2], Sara Williams[2], Lauren A. Garofalo[2]

[1] Department of Soil, Water, and Climate, University of Minnesota – Twin Cities, St. Paul, MN, USA

[2] Department of Chemistry, Colorado State University, Fort Collins, CO, USA

[^]now at Engineering Laboratory, National Institute of Standards and Technology, Gaithersburg, MD, USA

[*]Correspondence to D.B. Millet, dbm@umn.edu

Key Points

1. A small number of known organic compounds dominate the net and upward reactive carbon fluxes over a coniferous forest.
2. PTRMS captures VOCs controlling the net and upward fluxes, while ICIMS measures a range of important depositing species.
3. Far more VOCs contribute to the downward fluxes than are currently modeled, leading to a major sink underestimate.

Abstract

We use observations from dual high-resolution mass spectrometers to characterize ecosystem-atmosphere fluxes of reactive carbon across an extensive range of volatile organic compounds (VOCs) and test how well that exchange is represented in current chemical transport models. Measurements combined proton-transfer reaction mass spectrometry (PTRMS) and iodide chemical ionization mass spectrometry (ICIMS) over a Colorado pine forest; together, these techniques have been shown to capture the majority of ambient VOC abundance and reactivity. Total VOC mass and associated OH reactivity fluxes were dominated by emissions of 2-methyl-3-buten-2-ol, monoterpenes, and small oxygenated VOCs, with a small number of compounds detected by PTRMS driving the majority of both net and upward exchanges. Most of these dominant species are explicitly included in chemical models, and we find here that GEOS-Chem accurately simulates the net and upward VOC mass and OH reactivity fluxes under clear sky conditions. However, large upward terpene fluxes occurred during sustained rainfall, and these are not captured by the model. Far more species contributed to the downward fluxes than are explicitly modeled, leading to a major underestimation of this key sink of atmospheric reactive carbon. This model bias mainly reflects missing and underestimated concentrations of depositing species, though inaccurate deposition velocities also contribute. The deposition underestimate is particularly large for assumed isoprene oxidation products, organic acids, and nitrates—species that are primarily detected by ICIMS. Ecosystem-atmosphere fluxes of ozone reactivity were dominated by sesquiterpenes and monoterpenes, highlighting the importance of these species for predicting near-surface ozone, oxidants, and aerosols.

Plain Language Summary

Reactive carbon species in the atmosphere have a strong influence on air quality and climate and require accurate modeling to understand their global impacts. Natural ecosystems such as forests both emit and take up reactive carbon to and from the atmosphere, acting simultaneously as the largest source and an important sink of these species. We performed the most comprehensive measurements to date of this two-way reactive carbon exchange over a pine forest. We observed that the upward reactive carbon exchange was controlled by just a few known species and was much larger than the downward exchange, which was composed of far more species. We compared

the observations to chemical model predictions and found that the model accurately simulates the net reactive carbon exchange over this forest because the few species dominating that exchange are included in the model. However, the model does not adequately simulate the many depositing species, leading to a large underestimate for this sink of atmospheric reactive carbon.

1. Background

Surface-atmosphere exchange of volatile organic compounds (VOCs) plays a major role in modifying the chemical and physical properties of the atmosphere. In particular, the terrestrial biosphere is a major source of biogenic VOCs to the atmosphere (~1000 Tg C yr^{-1}) that is nearly an order of magnitude larger than the estimated anthropogenic source (90-160 Tg C yr^{-1}) (Boucher et al., 2013; Glasius & Goldstein, 2016; Huang et al., 2017). Emission uncertainties for these biogenic VOCs frequently exceed 200% both globally and regionally (Sindelarova et al., 2014). Even for isoprene, the best-studied biogenic VOC, model disparities can reach a factor of 4 (Arneth et al., 2011). Developing an improved understanding of biosphere VOC emissions is thus an important science priority.

At the same time, terrestrial ecosystems are a primary depositional sink for oxygenated VOCs, which are compounds that can be directly emitted or formed in the atmosphere through VOC oxidation. Additional oxygenated VOC sinks include chemical reactions, wet scavenging, and condensation to form secondary organic aerosol (SOA) (Lary & Shallcross, 2000; Mellouki et al., 2015; Muller & Brasseur, 1999; Singh et al., 1995). Since oxygenated VOCs are ubiquitous and represent the majority of ambient reactive carbon (Bates et al., 2021; Chen et al., 2019; Heikes, 2002; Jacob et al., 2002; Millet et al., 2008, 2010, 2015), uncertainties in their dry deposition limit our understanding both of the overall VOC budget (Safieddine et al., 2017) and of the partitioning between reactive carbon loss pathways. For example, prior studies have shown that deposition uncertainties encompass a range that can change predicted oxygenated VOC and SOA concentrations by as much as 50% (Bessagnet et al., 2010; Nguyen et al., 2015).

With up to 10^5 different organic species thought to exist in the atmosphere (Goldstein & Galbally, 2007), there are open questions regarding the number of VOCs undergoing surface-atmosphere exchange (Park et al., 2013), the main environmental factors driving that exchange (Yáñez-Serrano et al., 2015), and the extent to which those factors are represented in current chemical transport models (CTMs; Millet et al., 2018). To date there have been few direct ecosystem-scale flux observations with comprehensive VOC coverage to address those questions. Park et al. (2013) performed detailed flux measurements over an orange orchard and detected 555 species contributing to the net VOC flux budget—with 10 commonly-known compounds making up 68% of the total flux. A recent study over a winter wheat field measured fluxes for 264 VOCs, with only four ubiquitous oxygenated VOCs accounting for 85% of total emissions (Loubet et al., 2022). A third study over a mixed temperate forest observed 377 VOCs with detectable surface-atmosphere exchange (Millet et al., 2018). While the GEOS-Chem CTM underestimated net fluxes by 40-60%, the exchange was dominated (90% on a carbon basis) by known VOCs included in the CTM—and isoprene alone represented >90% of the OH reactivity-weighted flux.

The aforementioned studies are limited by their reliance on proton-transfer reaction mass spectrometry (PTRMS) alone to characterize total ecosystem VOC fluxes. PTRMS measures a wide but incomplete suite of VOCs; the technique has been shown to capture a large portion of gas-phase VOC carbon (VOC-C) and associated OH reactivity over forests (Hunter et al., 2017), but it misses more oxidized VOCs, organic nitrates, organosulfur compounds, and other species that can undergo bidirectional surface-atmosphere exchange. Field deployable negative-ion chemical ionization mass spectrometry (CIMS) methods (e.g., using iodide, I^-; acetate, CH_3COO^-; or trifluoromethanolate, CF_3O^- ions) can detect molecules not present in the PTRMS spectrum (Beaver et al., 2012; Bertram et al., 2011; Lee et al., 2014; Mattila et al., 2018), thereby better constraining the speciation, direction, and magnitude of total VOC fluxes when paired with PTRMS measurements.

Here we present the most comprehensive ecosystem-scale VOC flux measurements to date, obtained by applying the eddy covariance (EC) technique to spectra collected simultaneously using dual high-resolution time-of-flight mass spectrometers (PTRMS and ICIMS). Measurements were collected over a ponderosa pine plantation and provide a detailed and novel characterization of bidirectional fluxes across the two mass spectra encompassing hydrocarbons, low-to-mid molecular weight oxygenated VOCs, N-containing species, and halogenated species. Detected species are expected to cover the majority of gas-phase VOC-C and associated OH reactivity undergoing surface exchange (Hunter et al., 2017). We quantify the relative contributions of PTRMS- and ICIMS-detected species to the total net, upward, and downward VOC-C fluxes and interpret the combined observations with the GEOS-Chem CTM to test current understanding of VOC flux drivers and the importance of previously unknown or unmodeled compounds. We further determine the total OH and O_3 reactivity fluxes to better constrain the overall influence of two-way ecosystem VOC fluxes on atmospheric chemistry.

2. Methods

2.1 Measurement Site

The Flux Closure Study 2021 (FluCS 2021) took place from 06 August to 25 September 2021 at the Manitou Experimental Forest (39.1006° N,105.0942° W, ~2370 m elevation) in the Colorado Front Range. Chemical and meteorological observations were made at the Manitou Experimental Forest Observatory (MEFO), a semi-arid mountainous site established by the National Center for Atmospheric Research (NCAR) in 2008 (Ortega et al., 2014). The site is surrounded by an open canopy of primarily ponderosa pine (~15 m height), shrubs, and grassland with a summertime leaf area index of ~1.2 m^2 m^{-2} (Berkelhammer et al., 2016). The area is normally unpolluted but is at times impacted by surrounding cities (e.g., Colorado Springs), suburbs, and wildfires. The MEFO site has been previously used for EC studies of 2-methyl-3-buten-2-ol (232-MBO) and isoprene (Thomas Karl et al., 2014), small organic acids (Fulgham et al., 2019), and other oxygenated VOCs (Kaser et al., 2013a; S. Kim et al., 2010). Other detailed atmospheric chemistry studies at MEFO have primarily focused on reactive carbon abundance and chemistry (Karl et al., 2012; Kaser et al., 2013b; Link et al., 2021; Wolfe et al., 2014; Zhou et al., 2015).

FluCS 2021 included ambient observations of VOCs, NO_x, O_3, CO, and OH reactivity from a 28 m walk-up tower, along with HONO and HO_x radical measurements near the tower base. The tower-based PTRMS and ICIMS measurements are described in the following section. VOC speciation was characterized via offline thermal desorption gas chromatography mass spectrometry (GC-MS) analysis of sorbent tubes that sampled ambient air as well as ponderosa pine and understory emissions using a portable photosynthesis system (PPS; LI-6800, LI-COR Biosciences) (Riches et al., 2020) (**S1.1**). A high-resolution aerosol mass spectrometer (HR-AMS; Aerodyne Research, Inc.) sampling 4.5 m above the ground at the instrument building measured submicron nonrefractory aerosol mass and composition (**S1.2**) (Canagaratna et al., 2015; DeCarlo et al., 2006).

Tower sampling employed custom built, identical PFA inlets (I.D. 0.375”, length 45 m) held at 45 °C to minimize wall interactions and avoid water condensation. These inlets were installed at six heights (3.2, 6.9, 10.6, 14.6, 19.8, and 27.8 m) and oriented at 200° into the prevailing wind. 3D winds and temperature were recorded at 10 Hz from 6.9, 14.6, and 27.8 m using sonic anemometers (CSAT 3B, Campbell Scientific) collocated with the corresponding inlets. Inlets with sonic anemometers were mounted on 1.8 m booms to avoid wind modulation by the tower structure; remaining inlets were mounted on 0.9 m booms. A photosynthetically active radiation (PAR) sensor (MQ-100x, Apogee Instruments) positioned on the ground ~20 m in front of the sonic anemometers recorded half hourly photosynthetic photon flux densities (PPFD). **Fig. S1** summarizes the meteorological observations collected during FluCS 2021.

2.2 VOC measurements

VOCs were measured simultaneously using two high-resolution time-of-flight mass spectrometers housed in an air-conditioned trailer at the tower base. Both instruments employed the same custom-built automated sampling manifold to cycle through the six tower inlets every hour. The measurement sequence was offset between the two instruments and included 30 minutes of sampling from 27.8 m (for EC fluxes) followed by 5 minutes of sampling from each of the remaining inlets (for concentration gradients) and a 5 minute zero. Two rotary vane pumps (Model 1023, Gast Manufacturing) were used for sampling, with one dedicated to the 27.8 m inlet (35 standard liters per minute; SLPM) and one backing the remaining 5 inlets (10-15 SLPM each).

Continuous airflow was maintained through all six inlets to reduce surface adhesion. All wetted sampling surfaces upstream of the PTRMS and ICIMS were composed of PFA to avoid surface-catalyzed reactions of ambient compounds.

2.2.1 PTRMS Operation, Calibrations, and Data Processing

The PTRMS (PTR-QiTOF, Ionicon Analytik) time-of-flight analyzer collected ions (m/z 0-351) with a 33.2 μs extraction period; the resulting spectra were coadded to obtain results at 10 Hz. The mass axis was continuously calibrated using peaks for water vapor (m/z 21.022, $H_3{}^{18}O^+$), acetone (m/z 59.049, $C_3H_7O^+$), and an internal diiodobenzene standard (m/z 203.943, $C_6H_5I^+$ and m/z 330.848, $C_6H_5I_2{}^+$). The drift tube was held at 2.9 mbar, 80 °C, and 740 V to maintain E/N = 136 Townsend (Td). The overall operating conditions led to sensitivities and mass resolutions of 2400 cps/ppb (cps counts per second) and 4200 Δm/m for acetone, and of 850 cps/ppb and 4100 Δm/m for β-pinene. PTRMS subsampling details are outlined in **S1.3**.

The PTRMS was zeroed for 5 minutes hourly by passing sampled air through a platinum bead catalyst (3.2 mm diameter; Shimadzu Corp.) heated to 400 °C. Calibrations were performed once daily for 45 minutes between 00:00-03:00 Mountain Daylight Time (MDT) while the PTRMS was sampling from 27.8 m, with uninterrupted sampling of nocturnal gradients on the other inlets. Four-point calibration curves were collected for 27 VOCs via dynamic dilution of compressed ppm-level gas-phase standards into zero air (Apel-Reimer Environmental; **Table S1**). Laboratory calibrations were performed post-study for individual monoterpene (MT) isomers and for oxygenated terpenoids using aspirated cyclohexane solutions (**S2.1**; **Fig. S2-S3**). Formaldehyde (HCHO) calibrations were also performed post-study using a compressed standard, and the HCHO signal was corrected for methanol interference (**S2.2**; **Fig. S4**). Ambient isoprene concentrations and fluxes were derived by removing the 232-MBO contribution to measured signals at m/z 69.069 (**S2.2**). All signals were normalized to 2×10^5 cps of $H_3{}^{18}O^+$.

The total sesquiterpene (ΣSQT; $C_{15}H_{25}^+$, m/z 205.195) signal was calibrated on the last study day using a compressed β-caryophyllene standard. We apply the β-pinene sensitivity to the total monoterpene (ΣMT; $C_{10}H_{17}^+$, m/z 137.133) signal as this compound had the median sensitivity across all MT isomers identified with the offline GC-MS measurements. Sensitivities for other MT isomers were within 30% of β-pinene (**Fig. S2**). Uncalibrated VOCs employ the measured sensitivity for methacrolein (~1100 ncps/ppb), which had the median sensitivity and humidity dependence across all calibrated compounds. We then apply the second lowest and highest measured sensitivities for all VOCs (275-3000 ncps ppb^{-1}) to derive lower and upper uncertainty bounds for the sum of uncalibrated species.

Humidity corrections were derived on the last study day by diluting VOC standards into zero air with varying water vapor concentrations (LI-610 Portable Dew Point Generator, LI-COR Biosciences). Water vapor concentrations were determined from the ratio of $H_2O{\cdot}H_3O^+$ (m/z 37.028) to $H_3{}^{18}O^+$, scaled by isotopic abundance: $(H_2O{\cdot}H_3O^+)/(500 \times H_3{}^{18}O^+)$. Values of this ratio ranged from 0.003 – 0.05 during the study. Calibration curves were collected at dew points ranging from -10 to 15 ^{o}C ($(H_2O{\cdot}H_3O^+)/(500 \times H_3{}^{18}O^+) = 0.002 – 0.2$), with the resulting sensitivity vs. water signal fits used to humidity-correct the field data. These corrections led to only modest (typically <15%) changes in the derived calibrations.

Peak fitting and integration were performed using the Ionicon Data Analyzer v 1.0.0.2 (IDA; Ionicon Analytik) (Müller et al., 2013). A custom table of 1340 peaks for m/z 13-351 was generated from this dataset, with 56 days of continuous 10 Hz data then fitted and integrated in one week on a standard workstation. Of the 1340 ions, 776 species were identified using PTRwid (Holzinger, 2015) and the molecular formula assignment workflow used in Millet et al. (2018). All subsequent data processing was performed in MATLAB (R2021a, MathWorks).

2.2.2 ICIMS Operation, Calibrations, and Data Processing

The ICIMS (Bertram et al., 2011; Brophy & Farmer, 2015) sampled at 5 Hz resolution, measuring ions of mass range m/z 2-491 with an extraction frequency of 40 μs. During measurement, the instrument pulls 1.9 SLPM of ambient air into the ion molecule reactor (IMR) where it mixed with 1.3 SLPM of humidified ultra-high N_2 humidified to 85% (to reduce the instrument water dependence) and 1.0 SLPM of I^- ions in ultrahigh purity N_2, both introduced directly into the IMR. The IMR was held at ambient temperature and 100 mbar pressure. The ICIMS was zeroed for one minute every hour via N_2 overflow, followed by external standard calibrations of C_1-C_5 alkanoic acids via permeation tube over the subsequent four minutes. Tofware (v3.2.0, Aerodyne Research, Inc.) fit the mass spectra to the 578 selected ions, and integrated peak areas. The final reported peaklist (485 analyte ions) used for the data analysis herein was limited to include only organic compounds containing C, H, N, and O. We normalize all ICIMS signal to the average sum of I^- and $I{\cdot}H_2O^-$ during instrument zeros (~1.4 x 10^6 cps). The mass resolution and sensitivity for formic acid (CH_2O_2) were 3500 Δm/m and 7.29 ncps ppt^{-1}, respectively. We estimate sensitivities for uncalibrated species using the log-linear dependence of instrument sensitivity on the gradient in voltages (dV) between adjacent ion optics within the ICIMS that controls collisionally-induced dissociation of I^- adducts (Lopez-Hilfiker et al., 2015). We determined the half-maximum of a sigmoidal fit of dV vs. analyte signal (dV_{50}) for a suite of calibrants to quantify the relationship between sensitivity and dV_{50} (**Fig. S5**), which was then applied to field-determined dV_{50} values for uncalibrated species across the ICIMS spectrum (**S1.4**) (Bi et al., 2021; Iyer et al., 2016; Lopez-Hilfiker et al., 2014; Mattila et al., 2020). Errors in sigmoidal fits were propagated to derive sensitivity uncertainties for uncalibrated ICIMS species.

There was some overlap in species coverage between the PTRMS and ICIMS, including for several organic acids; in these cases, results were employed from a single instrument based on superior flux signal-to-noise and/or availability of in-field calibrations.

2.4 Flux calculations

EC fluxes were calculated from the covariance of concentration (*X*) with vertical wind (*w*) for an ensemble of *n* measurements (Stull, 1988) within a 30-minute period:

$$F_C = \overline{w'X'} = \frac{1}{n}\sum_{i=1}^{n}(w_i - \overline{w})(X_i - \bar{X}) \quad \textbf{(E1)}$$

Fluxes were derived based on the native PTRMS and ICIMS sampling frequencies of 10- and 5-Hz, respectively. Concentrations and winds were first despiked using the median absolute deviation method (Mauder et al., 2013) and detrended by subtracting a linear fit to each 30-minute signal time series. Winds underwent double rotation so that $\overline{w}$ = 0 for each averaging period (X. Lee et al., 2005). The time lag between the sonic wind measurements and the corresponding VOC detection within the mass spectrometer was quantified from the maximum *w*-*X* cross-covariance. Lag times derived in this way for ΣMT and formic acid (HCOOH) were employed for all PTRMS and ICIMS compounds, respectively (**Fig. S6**), due to the high flux signal-to-noise in each case.

Flux uncertainties were determined for each averaging period as 1.96× the standard deviation of the outer 30 points within a 600-point lag time window centered around the peak in *w*-*X* cross-covariance. The resulting flux uncertainties averaged 16%, 21%, and 8% for 232-MBO, ΣMT, and HCOOH, respectively. Species whose mean fluxes were lower than their uncertainty calculated in this way were removed from the following analyses. Sensitivity tests described later assess how the inclusion versus exclusion of these compounds affects our overall findings. Additional recommended EC filtering criteria were applied based on wind shear and stationarity (**S3**) (Foken & Wichura, 1996).

Figure S7 shows examples of frequency-normalized cospectra for VOCs measured by PTRMS and by ICIMS as well as for sensible heat. High frequency attenuation through the sampling line was estimated for each VOC using the empirical model of Horst (1997) (**S4**), resulting in cumulative corrections of 8.2% and 43%, respectively, for the total upward and downward fluxes, and a 5.5% correction for the net flux (**Fig. S8**).

2.5 Model runs

Model simulations for the study period were performed using GEOS-Chem v13.3.0 (https://geos-chem.org/). The model uses assimilated meteorological data (Goddard Earth Observation System

Forward Processing product; GEOS-FP) from the NASA Global Modeling and Assimilation Office (GMAO), which have native horizontal resolution of 0.25° × 0.3125°, 72 vertical layers, 3-h temporal resolution for 3-D meteorological parameters, and 1-h resolution for surface quantities and mixing depths. We performed a nested, full-chemistry simulation at 0.25° × 0.3125° using the FlexGrid functionality for 06 July to 01 October 2021 within a custom domain surrounding MEFO (±3° latitude and longitude). Boundary conditions were taken from a 2° × 2.5° global model run for the same time period that was itself initialized using output from a year-long global simulation at 4° × 5°. Nested simulations employed 5 and 10 min timesteps for transport and chemistry, respectively, while global simulations used 15 and 30 min timesteps (Philip et al., 2016).

The full-chemistry GEOS-Chem chemical mechanism used here features comprehensive HO_x-NO_x-O_x-VOC-Br-Cl-I chemistry coupled to aerosols and incorporates the most recent JPL/IUPAC recommendations. GEOS-Chem v13 also incorporates recent chemical updates for isoprene oxidation (Bates & Jacob, 2019), small oxygenated VOCs (Bates et al., 2021; Chen et al., 2019), halogens (Wang et al., 2019), and small alkyl nitrates (Fisher et al., 2018). For the present analysis we added simplified oxidation schemes for 232-MBO, ∑SQT, and >C2 organic acids (lumped as RCOOH and treated as propanoic acid) to the chemical mechanism (**Table S2**), with RCOOH dry deposition also included (**Table S3**) using a Henry's law constant for propanoic acid from Sander (2015). Rate coefficients for the updated mechanisms are taken from the Master Chemical Mechanism (Saunders et al., 2003) and product yields from published laboratory studies (Fantechi et al., 1998; Ferronato et al., 1998).

Land cover in the 0.25° × 0.3125° model grid cell containing the MEFO site is heterogenous, with 6 Community Land Model (CLM) classifications and cropland plus bare ground accounting for 46% of the total area. This is not representative of the 1 × 1 km^2 measurement footprint, which primarily consists of ponderosa pine, grass, and shrubs (**Fig S9-S10**). We therefore modified the model land cover and leaf area to more realistically reflect the MEFO site as described in **S5** (Byrne et al., 2005; Guenther et al., 2006; Olson et al., 2001).

Model emissions use the Harmonized Emissions Component module version v3 (HEMCO v3) (Lin et al., 2021), with biogenic emissions from terrestrial plants computed online using the Model of Emissions of Gases from Nature (Guenther et al., 2012) as implemented in GEOS-Chem by Hu et al. (2015). For simulations here we implemented 232-MBO and ∑SQT emissions and updated the plant species-specific basal emissions for all VOC to the latest available MEGAN values (MEGAN v3.2; Guenther et al., 2020) within the nested domain. Global anthropogenic emissions are from the Community Emissions Data Systems (CEDS, year-2019) inventory (Hoesly et al., 2018) and biomass burning emissions from the Global Fire Emissions Database v4 (GFED4, year-2019) (Giglio et al., 2013).

In analyses that follow, cumulative model fluxes are calculated by summing the simulated emissions, dry deposition, and net chemical production/loss scaled to the height of the first model layer (**Fig. S11**). The net chemical production/loss is then the average of two limiting cases where either all or none of the production/loss in this grid cell occurs below our sensor.

3. Results and Discussion

3.1 Contributions to VOC carbon flux

Many species contributed to the measured VOC-C fluxes over the sampled ecosystem. Of the 744 PTRMS and 485 ICIMS ions identified as VOCs, 230 and 85 had detectable fluxes, respectively, based on an S/N threshold of 1.96. This drops to 65 (PTRMS) and 25 (ICIMS) when instead using S/N =3 (**Figure S8**). **Figure 1** shows the contribution of individual ions to the total detected VOC-C mass flux. Net fluxes were partitioned into upward and downward components based on the exchange direction for each molecule and averaging period (**Figure 1a**), allowing bidirectional ions to contribute to both upward and downward fractions. **Table S4** shows the top ten contributors to upward and downward VOC-C fluxes, as well as to the reactivity fluxes discussed later.

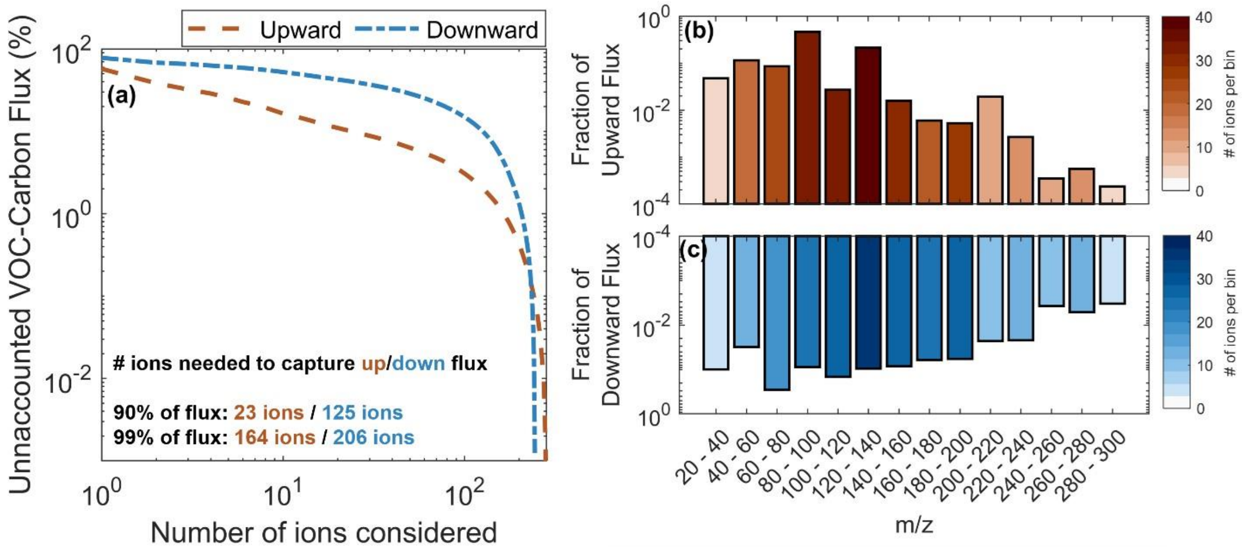

Figure 1: Summary of observed VOC ions undergoing ecosystem-atmosphere exchange. a) Percentage of unaccounted VOC-C upward (orange) and downward (blue) fluxes as a function of the number of ions considered. b) Fractional ion contributions to the total observed upward (top, orange) and downward (bottom, blue) fluxes. Each bin is colored by the number of ions encompassed. 315 total ions with detectable flux are included.

Measured upward VOC-C fluxes at MEFO arise from 283 individual ions, but a large majority of the mass comes from a small number of known species that are commonly simulated in CTMs. 232-MBO (43%) and ΣMT (19%) make up ~60% of the cumulative upward mass flux, with ethanol (C_2H_5OH), methanol (CH_3OH), hydroxyacetone ($C_3H_6O_2$), and isoprene (C_5H_8) contributing an additional 15%. In all, only 23 species account for 90% of the upward VOC-C flux, and these are exclusively hydrocarbons or oxygenated VOC with 3 or fewer oxygen atoms ($n_O \leq 3$). Sesquiterpenes make up 1.7% of the observed upward flux on a carbon basis, but as will be seen later, they make a much larger contribution to the reactivity fluxes. These observations represent one of just a few reported canopy-scale flux datasets for ∑SQT (Fischer et al., 2021; Vermeuel et al., 2022). The remaining 10% of the upward VOC-C flux beyond the 23 dominant compounds is more diverse, with 164 ions needed to capture 99% of the total.

245 total ions had detectable downward fluxes during the campaign. Of these, 125 ions accounted for 90% of the flux—compared to just 23 for the upward fluxes. The two largest contributors to the cumulative downward VOC-C flux were $C_3H_6O_2$ (22%) and HCHO (9.8%). Other key

contributors included acetic acid ($C_2H_4O_2$), other likely organic acids (e.g., succinic acid, $C_4H_6O_4$; lactic acid, $C_3H_6O_3$; pyruvic acid, $C_3H_4O_3$), anhydrides (maleic anhydride, $C_2H_4O_3$; acetic anhydride, $C_4H_6O_3$), and isoprene oxidation products (ISOPOOH/IEPOX, $C_5H_{10}O_3$; IEPOX oxidation product, $C_4H_8O_3$; hydroxymethyl-methyl-a-lactone (HMML), $C_4H_6O_4$; MVK hydroperoxy-carbonyl (MVKPC), $C_4H_6O_3$; isoprene nitrate, $C_5H_9NO_4$). A total of 206 ions are needed to capture 99% of the downward flux. Overall, we see that the total downward VOC-C fluxes are controlled by a far larger set of species than is the case for the upward fluxes, which agrees with findings from Millet et al. (2018) over a mixed temperate forest.

In the following sections (**3.2** and **3.3**) we compare the aggregated VOC fluxes with those predicted by the GEOS-Chem CTM. We then examine the key environmental and chemical drivers of flux variability and of the associated model biases (**3.4**).

3.2 Total upward VOC-C fluxes are well-simulated by GEOS-Chem but downward fluxes are not

Figure 2 compares the total measured and modeled VOC-C fluxes. The observed net and upward VOC-C fluxes are broadly captured by the model, which exhibits a small positive bias (21-32% for the campaign as a whole) in both cases that exceeds the statistical and calibration uncertainties shown in **Fig. 2.** We see that the net observed fluxes (mean $F_{C,net,obs.} = 2.5 \times 10^{12}$ atoms C cm^{-2} s^{-1}) are controlled by and nearly equal to the upward fluxes ($F_{C,up,obs} = 2.8 \times 10^{12}$ atoms C cm^{-2} s^{-1}), revealing this to be a primarily emitting ecosystem—and this feature is also well-represented by the model ($F_{C,net,mod} = 3.3 \times 10^{12}$ atoms C cm^{-2} s^{-1} versus $F_{C,up,mod} = 3.4 \times 10^{12}$ atoms C cm^{-2} s^{-1}). Two daytime peaks are observed in the net and upward flux diel profiles (**Fig. 2d-e**): one between 08:00 and 11:00 MDT that is missing from the model, and one between 12:00 and 15:00 MDT. The morning peak is a consequence of a diurnal mountain-valley flow pattern previously documented at this site (Ortega et al., 2014) (**S6**, **Fig. S12)** while the afternoon peak arises from the temperature and light dependence of VOC emissions.

The GEOS-Chem model successfully represents ~50% of the day-to-day upward flux variability seen in the observations (slope = 1.3; r^2 = 0.48 for the daytime means). This demonstrates some fidelity at reproducing the environmental drivers of VOC-C emissions but leaves over half the day-to-day variability unresolved. The model also exhibits a systematic and sustained terpenoid flux underestimate from 2-7 September during intense rains (**Fig. S13**), and this is discussed further in **Section 3.4**.

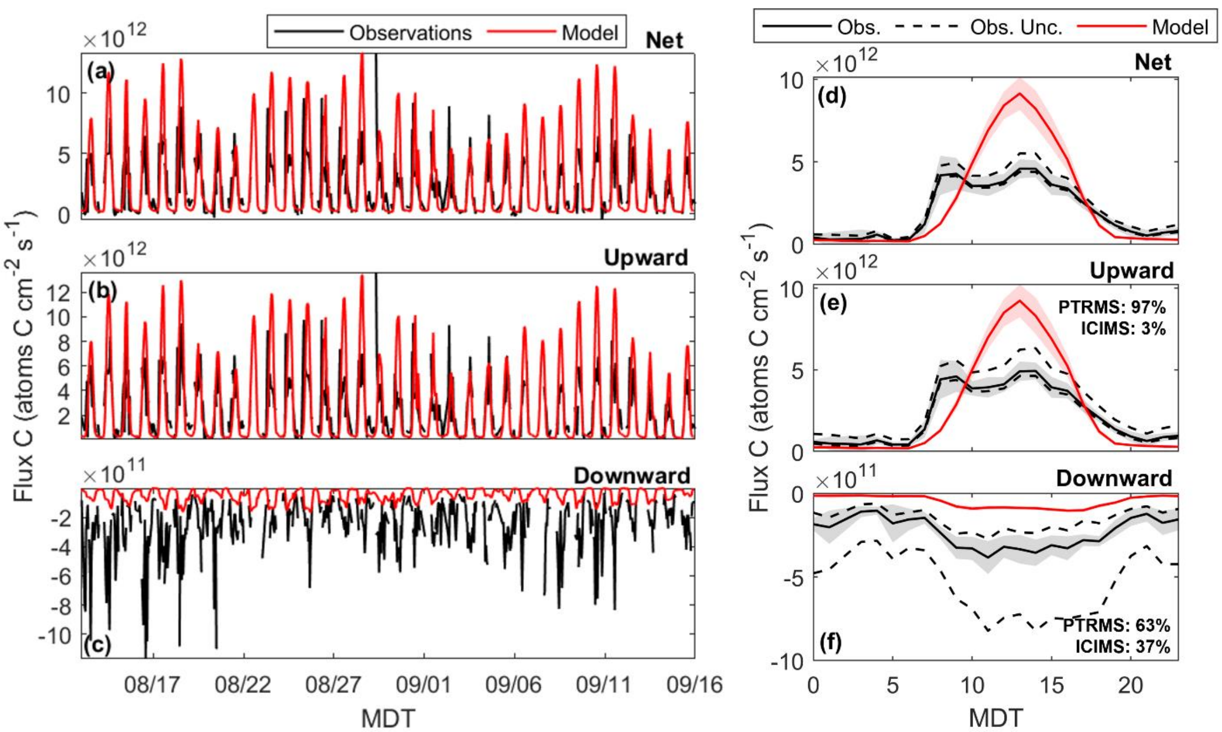

Figure 2: Summary of observed and modeled VOC-C fluxes. a-c) Observed (black) and modeled (red) net, upward, and downward VOC-carbon fluxes. d-f) Corresponding mean diel flux profiles. Shaded regions show 95% confidence intervals. Dashed lines indicate the upper and lower calibration uncertainties. Percentages of the total flux captured by the PTRMS and ICIMS are displayed inset.

The model has far less success at predicting the downward VOC-C fluxes, with a negative model bias that averages more than a factor of four (mean $F_{C,down,mod.}$ = -6.2 x 10^{10} atoms C cm^{-2} s^{-1} versus $F_{C,down,,obs.}$ = -2.6 x 10^{11} atoms C cm^{-2} s^{-1}). Calibration uncertainties (which could increase the observed total by up to 2.5× or decrease it by 1.5×) are insufficient to resolve the disparity. The model also fails to capture any of the observed day-to-day variability in the downward fluxes, with an overall model-measurement r^2 of 0.01 for the daytime means. The observed downward fluxes are greatest during smoky and warm periods (16-19 August, 30 August – 01 September, 07-11 September) when enhanced levels of oxygenated VOCs from advected fire plumes and increased precursor emissions dry deposit to the relatively low-concentration forest canopy below. The model fares significantly worse at representing the downward VOC-C flux variability during these periods (when the two are anti-correlated) compared to the clear sky days ($r^2 = 0.22$). We return to this point in more detail later.

We can explore the causes of the large model $F_{C,down}$ bias by examining the effective deposition velocity ($v_{d,eff.}$) and concentration ($[VOC\text{-}C]_{down}$) for the aggregated species undergoing downward flux ($v_{d,eff.} = F_{C,down} / [VOC\text{-}C]_{down}$). **Figure 3** compares the modeled and observed diel profiles for $v_{d,eff}$ and $[VOC\text{-}C]_{down}$. The modeled and observed diel profile shapes are consistent in each case: $v_{d,\mathrm{eff}}$ peaks with turbulent mixing during daytime whereas $[VOC\text{-}C]_{down}$ shows an afternoon decrease due to oxidative loss. However, the observations reveal sustained deposition through the night when the model predicts near-zero $v_{d,eff}$. This nighttime deposition implies that in-canopy turbulence is sufficient to drive appreciable nonstomatal loss at this time—a process that is absent from the model. Considering both day and night, the model underpredicts both $v_{d,\mathrm{eff}}$ and $[VOC\text{-}C]_{down}$ but the latter disparity is larger (factor of 3.7 for the 24-hour average versus 1.7 for $v_{d,eff}$). While the v_d discrepancy bears further investigation, we conclude that underestimated and missing VOC-C mass is the main driver of the model downward flux bias found here.

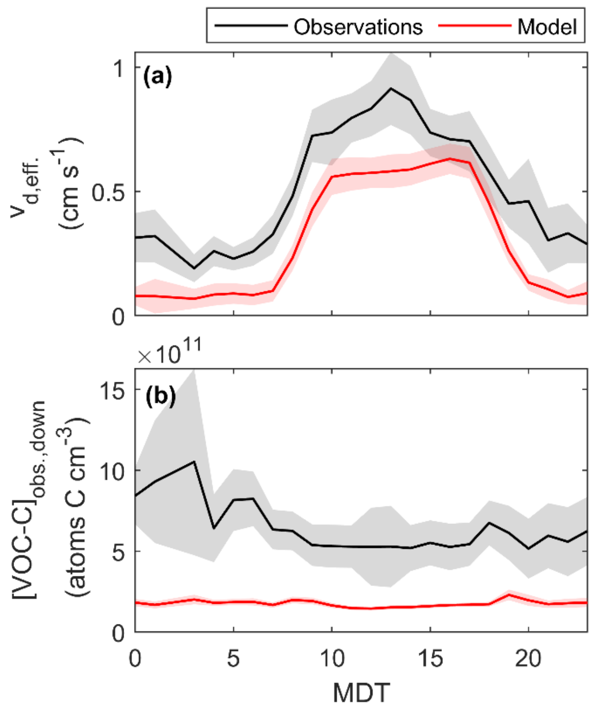

Figure 3: Mean diel profiles for the measured (black) and modeled (red) a) effective deposition velocities ($v_{d,eff}$) and b) concentrations ([VOC-C]$_{down}$) for all VOCs exhibiting downward fluxes. Shaded areas indicate 95% confidence intervals.

3.3 Total reactivity fluxes are controlled by few, known compounds

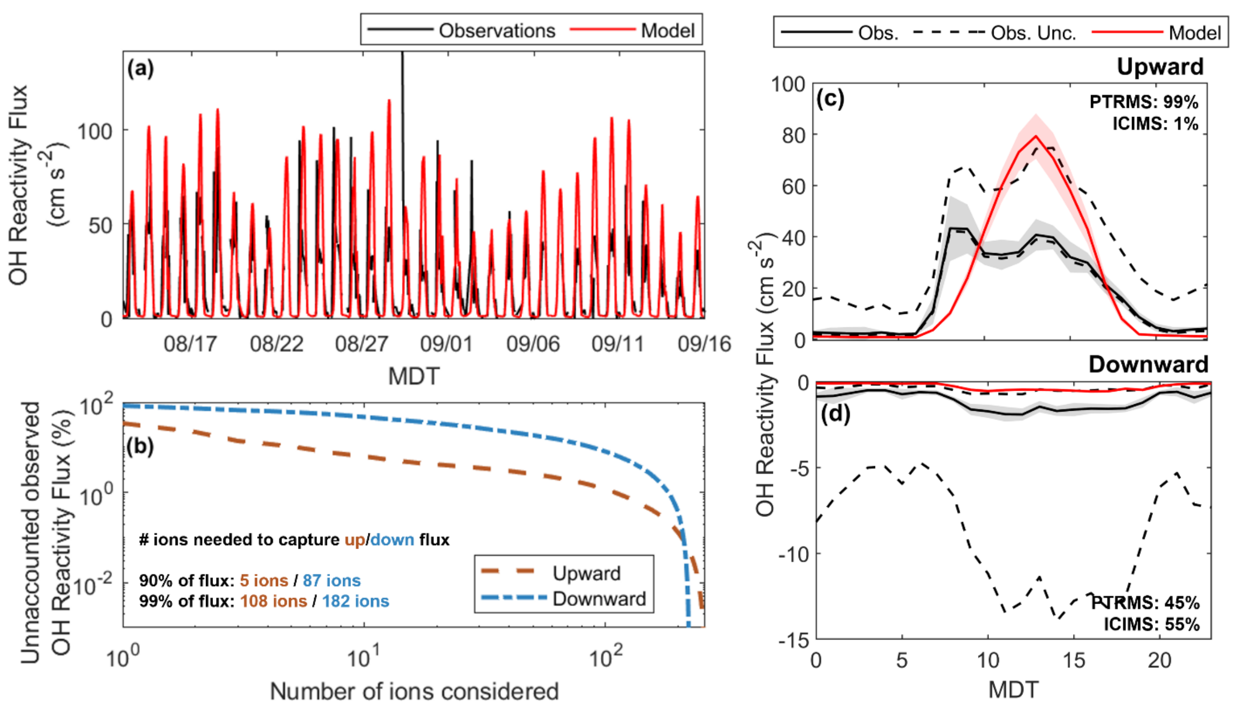

Figure 4: Summary of observed and modeled OH reactivity fluxes. a) Time series of modeled (red) and

observed (black) OH reactivity fluxes (k_{OH+VOC}·F_{VOC}). b) Percentage of unaccounted upward (orange) and downward (blue) OH reactivity flux as a function of the number of ions considered. Mean diel c) upward and d) downward OH reactivity fluxes are also shown. Observed and modeled fluxes are displayed respectively as the solid black and red lines with 95% confidence intervals about the mean. Upper and lower uncertainty bounds associated with VOC calibration and assigned reaction rate coefficients are plotted as the black dashed lines. Percentages of the total reactivity flux captured by the PTRMS and ICIMS are indicated inset.

While the VOC-C fluxes discussed above quantify the exchange of organic mass between the forest canopy and atmosphere, the resulting impact on atmospheric chemistry can be described via the oxidant reactivity fluxes F_{R_Y+VOC} = $\Sigma k_{Y+VOC} \cdot F_{VOC}$. Here, k_{Y+VOC} is the rate coefficient for reaction between a given VOC and an oxidant Y while F_{VOC} is the molar forest-atmosphere flux of that VOC. F_{R_Y+VOC} (cm s^{-2}) is equivalent to the time derivative of reactivity (R_{Y+VOC} = $\Sigma k_{Y+VOC} \cdot X_{VOC}$; s^{-1}), scaled to mixing height ($F_{R_Y+VOC} = h \cdot \frac{dR_{Y+VOC}}{dt}$), and thus directly characterizes the influence of surface fluxes on ambient oxidant reactivity (Millet et al., 2018).

We derive OH and O_3 reactivity fluxes by applying literature rate coefficients to the corresponding measured and modeled VOC fluxes (Atkinson et al., 2006; 1990; Atkinson & Arey, 2003; Chen et al., 2015; Grosjean et al., 1993; Grosjean & Grosjean, 1999; Lee et al., 2006; Reissell et al., 2000; Richters et al., 2015; Stedman & Niki, 1973). For species with known molecular formulae but unknown structure we obtain k_{OH+VOC} using the parameterization introduced by Donahue et al. (2013), and k_{O3+VOC} based on the computed double bond equivalent (DBE) as described in **S7**. A factor of 10 uncertainty in k_{Y+VOC} is estimated for such species by applying the same methodology to all measured species with known structure and k_{Y+VOC}. Further details are provided in **S7** (Chan et al., 2016; Helmig et al., 2007; D. Kim et al., 2011). Total F_{R_Y+VOC} uncertainties are propagated from those in the instrumental sensitivities (as described earlier) and in the assigned k values, and are dominated by the latter. Resulting uncertainties for F_{ROH} can change the net, upward, and downward fluxes by up to 55%, 85%, and 8×, respectively. Uncertainties for F_{RO3} can change the net, upward, and downward fluxes by up to 23%, 42%, and 7×.

Figures 4 and 5 summarize the observed and modeled OH and O_3 reactivity fluxes during the study period. In both cases we see a positive model bias of 16-30% in the net reactivity exchange (mean values: $F_{ROH,net}$ = 27.4 cm s^{-2} versus 21.1 cm s^{-2}, $F_{RO3,net}$ = 5.0 × 10^{-5} cm s^{-2} versus 4.3 × 10^{-5} cm s^{-2}). Only 5 ions account for over 90% of $F_{ROH,up,obs}$: 232-MBO (66%), ΣMT (12%), isoprene, ΣSQT, and acetaldehyde. Similarly, only 8 ions account for over 90% of $F_{RO3,up,obs}$ (**Fig. 5b**) with fluxes in this case primarily driven by ∑SQT (73%) and ΣMT (10%), followed by 232-MBO, isoprene, and butene. Many more ions are required to capture $F_{ROH,down,obs.}$ and $F_{RO3,down,obs.}$ (**Fig. 5c+d; Fig. 6c+d**); however, these fluxes are much smaller than the upward reactivity exchange as these more reactive compounds are primarily lost through chemistry rather than deposition. As with the carbon-based fluxes, the model has far more success at predicting day-to-day variability in the upward than in the downward reactivity exchange ($r^2_{R_{OH,up}}$ = 0.39, $r^2_{R_{OH,down}}$ = 0.07; $r^2_{R_{O3,up}}$ = 0.53; $r^2_{R_{O3,down}}$ = 0.02 for the daytime means). Collectively, these findings mirror those for the VOC-C fluxes, where: 1) $F_{R_{Y+VOC,net}}$ is primarily controlled by few, commonly measured and modeled emitting species; 2) far more ions are required to capture the downward reactivity fluxes; and 3) the GEOS-Chem model captures the general magnitude and much of the day-to-day variability in the upward fluxes but fails at both for the downward fluxes .

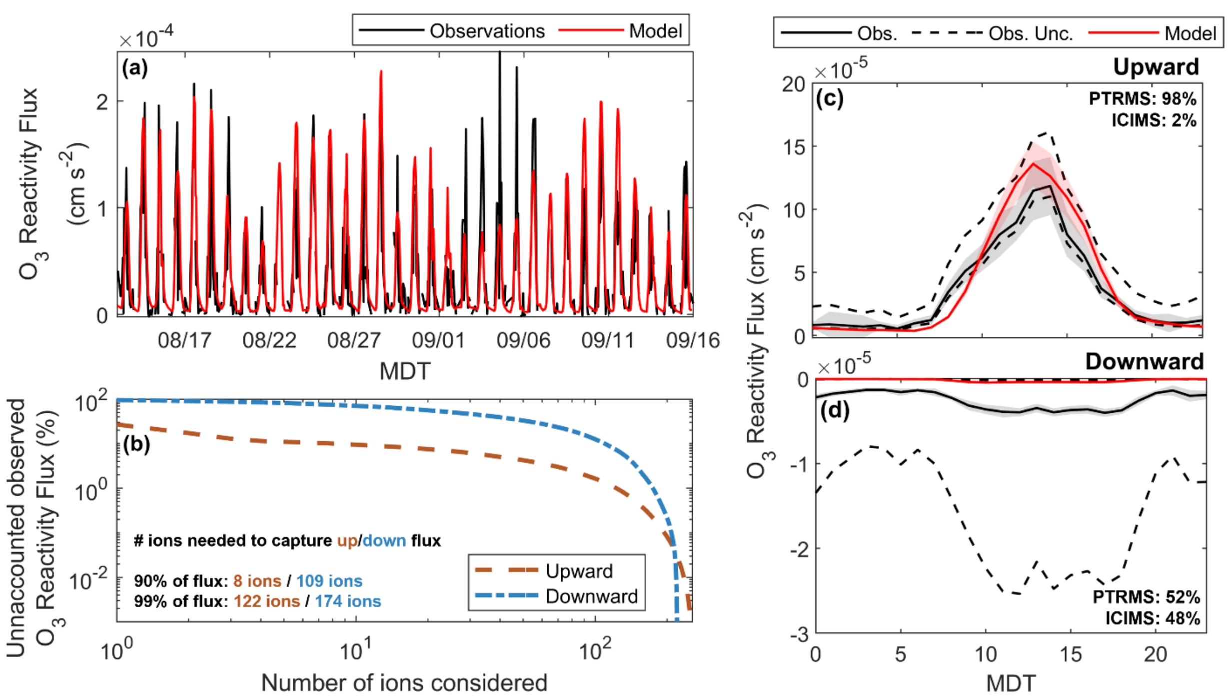

Figure 5: Summary of observed and modeled O_3 reactivity fluxes. a) Time series of modeled (red) and observed (black) O_3 reactivity fluxes (k_{O3+VOC}·F_{VOC}). b) Percentage of unaccounted upward (orange) and downward (blue) O_3 reactivity flux as a function of the number of ions considered. Mean diel c) upward

and d) downward O_3 reactivity fluxes are also shown. Observed and modeled fluxes are displayed respectively as the solid black and red lines with 95% confidence intervals about the mean. Upper and lower uncertainty bounds associated with VOC calibration and assigned reaction rate coefficients are plotted as the black dashed lines. Percentages of the total reactivity flux captured by the PTRMS and ICIMS are indicated inset.

The above findings highlight some priorities for updating current CTMs. In particular, the standard GEOS-Chem implementation does not feature any explicit chemistry for 232-MBO and ∑SQT; their emissions are only included to compute parameterized yields of acetone and SOA. Our findings here that 232-MBO and ∑SQT respectively account for the bulk of measured OH and O_3 reactivity fluxes demonstrate that this model omission neglects key regional sources of reactivity. We recommend explicit representation of both species in CTMs to reduce such biases and for better predictions of surface-atmosphere exchange and its chemical impacts.

In the following section we discuss the environmental and chemical drivers of flux variability and model-measurement disparities identified above.

3.4 Drivers of flux variability and of model-measurement disparities

3.4.1 Model upward flux biases arise from known species; downward flux biases arise from diverse species

Figure 6 groups the observed and modeled VOC-C fluxes by carbon oxidation state (OS_c) and DBE. DBE estimates the number of double bonds or rings for a given VOC from its molecular formula as DBE = $1 + n_c - n_H/2 + n_N/2$, and provides a first-order approximation of reactivity against OH addition or ozonolysis (Pagonis et al., 2019; Yuan et al., 2017). OS_c is computed as $OS_c = 2n_O/n_C - n_H/n_C$ and we use it here as a general marker of oxidation level and volatility (lower OS_c ~ higher volatility) (Isaacman-Vanwertz et al., 2018; Kroll et al., 2011). When there is an assumed nitrate group present ($n_N \geq 1$ and $n_O \geq 3$), OS_C is derived instead as $2n_O/n_C - n_H/n_C + 5n_N/n_C$. Based on these indices, **Figure 6** reveals significantly more chemical diversity in the observations than in the model predictions, with the model missing a large number of species with

DBE ≥ 2 and 2 ≥ OS_c ≥ -2. Below, we discuss how these unrepresented species drive model biases in the carbon and reactivity fluxes.

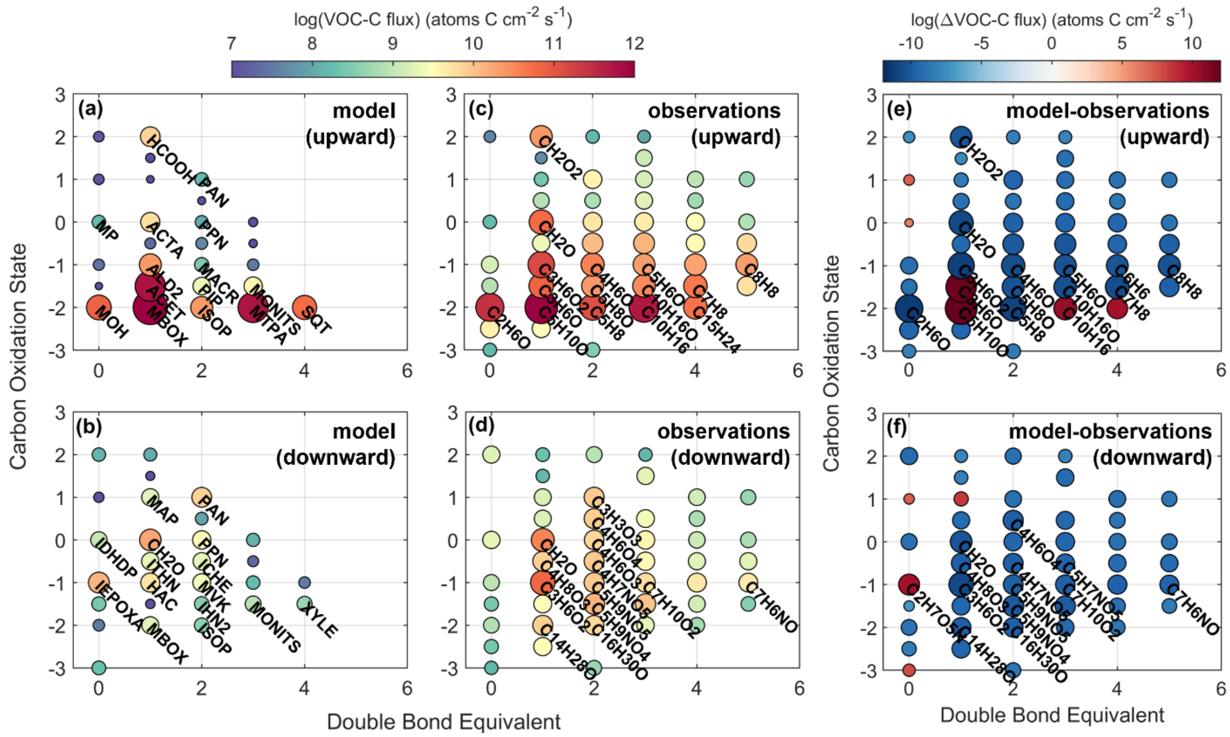

Figure 6: Upward and downward VOC-C fluxes grouped by carbon oxidation state and double bond equivalent. Modeled (a + b) and observed (c + d) fluxes are shown with circles colored and sized by the log of the flux magnitude. Model biases (e + f) are shown with circles colored by the log of the absolute model-measurement flux difference in each case. Circle sizes are proportional to the distance from log(Δflux) = 0. The top contributors to flux or Δflux are labeled on each plot. Names and formulae for GEOS-Chem species are detailed in **Table S5**.

First, we see a lack of species diversity in the predicted upward VOC-C fluxes (**Fig. 6a** versus **Fig. 6c**), with the model placing a higher proportion of the total flux in low-OS_c species. While substantial upward VOC-C fluxes (>10^{10} atoms C cm^{-2} s^{-1}) are observed for species with DBE ≥ 2 and -2 ≤ OS_c ≤ 0 (e.g., monoterpene oxides, $C_{10}H_{16}O$, and potentially unsaturated, oxygen-containing ring structures), these are largely missing from the model (**Fig. 6a**, **6e**). This implies missing emission sources or production routes for intermediate- to low-volatility species in GEOS-Chem.

Despite the above gap, the model nevertheless captures the dominant species controlling the total upward VOC-C flux and nearly all the upward flux bias. Of the 23 compounds making up 90% of the observed upward flux, 15 (85%) are explicitly modeled and the remaining 8 are included as lumped species. Offsetting model errors between these dominant species contribute to the aggregated model-measurement agreement seen in **Fig. 2a**. For example, predictions for 232-MBO and acetone (together 72% of the upward model VOC-C flux) are ~1.6× and ~12× too high, respectively, while those for ethanol, methanol, and isoprene are 3-4× too low. The latter underestimates partly reflect an understory contribution that is not accounted for by the model (**Figure S13**). As with VOC-C, model biases in the upward OH reactivity fluxes (mean $F_{\mathrm{ROH,up}}$ bias = 5.4 cm s^{-2}) arise primarily from known and modeled species—with model overestimates for 232-MBO (+8.0 cm s^{-2}) and ∑MT (+0.2 cm s^{-2}) offset by underestimates for isoprene, acetaldehyde, and other species included in GEOS-Chem (-2.6 cm s^{-2}). Overall, we obtain reasonable model-observation agreement for the upward VOC-C and reactivity fluxes because the model simulates the main species that dominate these fluxes, and because of compensating errors for those species.

Fewer of the species controlling the downward VOC-C fluxes are represented in GEOS-Chem. Explicitly-modeled VOCs (e.g., $C_3H_6O_2$, HCHO, $C_2H_4O_2$) account for only 34% of the observed total, though numerous other species are included in lumped form (e.g., RCOOH, isoprene hydroxynitrates (INP), isoprene nitrates (IHN), and multiple isomers for ISOPOOH and IEPOX). Species completely missing from GEOS-Chem make up ~10% of the measured downward flux; these are chemically diverse, spanning $3 \leq n_C \leq 10$, $2 \leq n_H \leq 15$, and $2 \leq n_O \leq 6$. As with the upward fluxes, we see in the observations a greater contribution from high DBE, high OS_c species than is predicted by the model (**Fig. 6b**, **6d**)**.** These disparities have a greater impact on overall model performance for $F_{C,down}$ because in this case there are not a few, dominant species controlling the overall flux. However, the largest individual model biases are still due to known and modeled VOCs. Together, the explicitly modeled and lumped species (primarily $C_3H_6O_2$, HCHO, $C_5H_9NO_4$) are responsible for a downward flux bias of -1.4×10^{11} atoms C cm^{-2} s^{-1}, compared to -5.8×10^{10} atoms C cm^{-2} s^{-1} for the unmodeled species. The known and modeled VOCs also make up over 85% of the total model $F_{\mathrm{ROH,down}}$ bias (-0.92 cm s^{-2}).

3.4.2 VOC-C flux temperature and light dependence

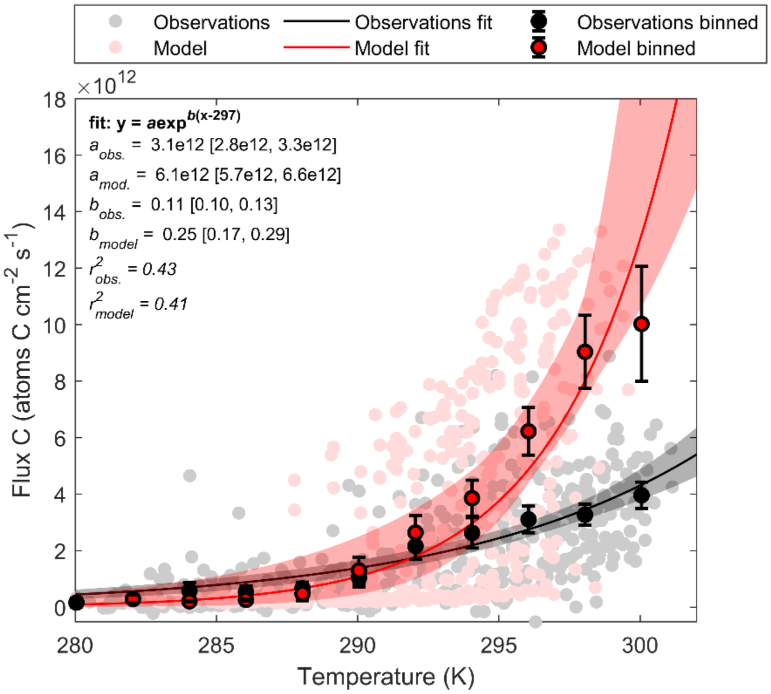

Figure 7: Environmental drivers of total net VOC-C fluxes. Observed (black) and modeled (red) VOC-C fluxes are plotted as a function of temperature. Fitted equations and parameters with associated 95% bootstrapped confidence intervals are shown inset and plotted as the black and red lines. Binned data points are indicated with the 95% confidence intervals about the mean.

We next investigate environmental drivers of the net VOC-C flux variability and model-measurement disparities. We focus in particular on surface temperature and PAR, and exclude data from 08:00-11:00 MDT to avoid the unresolved mountain-valley flow feature discussed earlier (**S6**). **Figure 7** plots the measured and modeled $F_{C,net}$ dependence on surface air temperature (T). Values are fit to $F_{C,net} = a \cdot exp^{b(T-297)}$, where a is the equivalent basal emission rate and b is the effective temperature response factor (K^{-1}) for the aggregated net VOC-C fluxes (A. B. Guenther et al., 2012). The model predicts higher fitted a and b parameters than are observed, explaining the overestimated afternoon peaks in the net and upward fluxes (**Fig. 2**). We saw earlier that the majority of the observed upward fluxes were comprised of directly-emitted VOCs such as 232-MBO, ∑MT, alcohols, and isoprene, and the findings here thus suggest overestimated MEGAN v3.2 emissions factors for these species from ponderosa pine and C3 grasses.

Figure 7 shows that the modeled and observed fluxes have similar temperature dependencies for $T < 295$ K but that the model strongly overpredicts VOC-C fluxes at higher temperatures. This behavior is consistent across all modeled emitting species and for both low and high light levels (**Fig. S14**). The modeled VOC-C flux light dependence is also steeper than suggested by the observations when $T > 295$ K (**Fig. S14**). However, the two relationships are statistically indistinguishable at lower temperatures, indicating that the apparent light-dependence disparity for $T > 295$ K reflects the same temperature-dependence bias shown in **Fig 7**.

3.4.3 Rain and smoke impacts on ecosystem VOC fluxes

Rain and smoke drove large changes in the observed VOC-C and reactivity fluxes and led to the some of the largest model-measurement disparities seen during the study. **Figure 8** summarizes the observed chemical flux anomalies from these periods, which are examined in more detail next. For the following discussion we define rainy days as those with rainfall > 1 mm hr^{-1} and smoky days as those when the observed organic aerosol (OA) mass consistently exceeded 2 μg m^{-3}; remaining days are then denoted as clear-sky periods. The OA mass was confirmed to be primarily fire-derived based on its strong correlation with the biomass burning tracers maleic anhydride ($C_4H_2O_3$), propanenitrile (C_3H_5N), and benzonitrile (C_7H_5N) (Coggon et al., 2019; Gilman et al., 2015) (**Fig. S16**).

Figure 8a shows that rainy periods have strong upward flux enhancements for compounds with DBE ≥ 3 and $OS_c \leq -1$. Specifically, there was an overall enhancement of 61% relative to the clear-sky periods for ΣMT, ΣSQT, monoterpene oxides ($C_{10}H_{16}O$, $C_9H_{14}O$, and $C_{10}H_{14}O$), and species with formulae $C_{10}H_{14}$, C_8H_8, and C_7H_8. Concentration gradient measurements indicate a canopy-level (ponderosa pine) source for all these compounds except ΣSQT, which are also emitted from the understory (**Fig. S15**). Previous studies have reported increased concentrations and emissions of terpenoids and other biogenic VOCs during and after rain at the branch-level (Lamb et al., 1985), above mixed and coniferous forests (Bourtsoukidis et al., 2014; Helmig et al., 1998; Holzinger et al., 2006), and at the MEFO site in particular (Kaser et al., 2013a). The latter study reported a 23× ΣMT flux enhancement during a hailstorm that was accompanied by enhanced emissions of $C_{10}H_{16}O$, $C_{10}H_{14}$, $C_9H_{14}O$, $C_{10}H_{14}O$, C_8H_8, and ΣSQT; the authors invoked mechanical wounding of leaves as a potential cause. Wounding is an unlikely explanation for the rainfall-driven enhancements found here. On the other hand, Schade et al. (1999) documented a positive ∑MT emission dependence on humidity (after rainfall) over a ponderosa pine plantation that they attributed to increased stomatal opening and/or enhanced cuticular permeability. We speculate that such effects are also responsible for the increased VOC emissions observed in our study. Overall, the rain-induced emission enhancements for high DBE, low OS_c compounds indicate a missing source mechanism for reactive terpenoids that should be considered in models over coniferous ecosystems.

In contrast to the terpenoids, all other species exhibited decreased emissions during rainfall due to low temperatures and light levels (**Fig 8a**), leading to a 13% decrease in the aggregated VOC-C upward fluxes on rainy days relative to clear sky days. Wet conditions also allow soluble oxygenated VOCs to partition more effectively to wet surfaces, thus reducing the upward flux component for bidirectional species. The largest emission decreases (>10^{11} atoms C cm^{-2} s^{-1}) were observed for 232-MBO, acetone, ethanol, hydroxyacetone, and acetaldehyde. We also observe decreased downward fluxes during rainfall for many species with higher DBE across a wide OS_c range (**Fig 8b**). These include nitriles, imides, benzoic acid, phenol, and other more hydrophobic compounds that are either fire-derived or photochemically produced and have low concentrations at these times due to reduced upwind emissions.

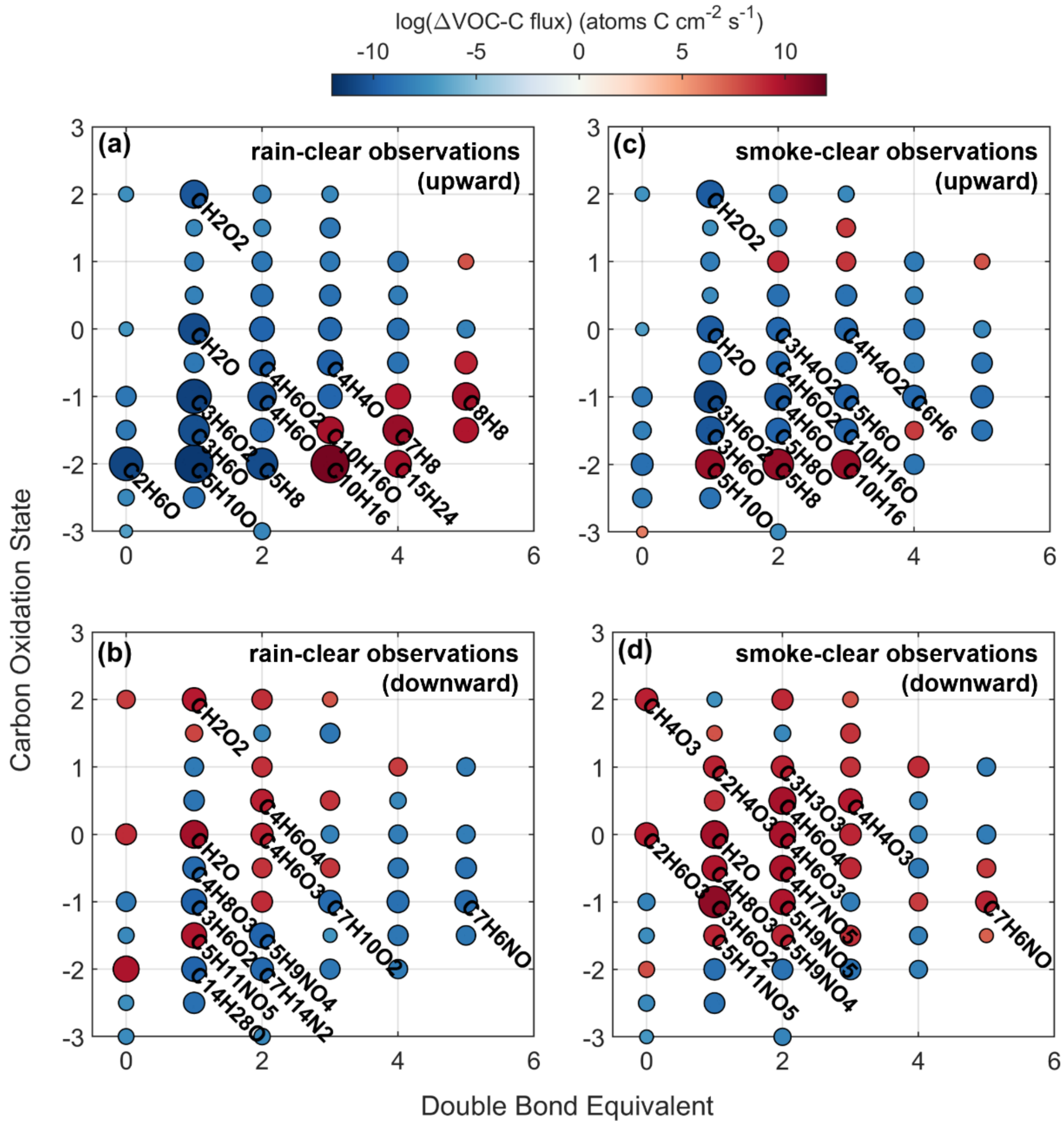

Figure 8: Effects of rain (a, b) and smoke (c, d) on observed upward and downward VOC-C fluxes. The difference in flux magnitude between rainy and clear-sky conditions and between smoky and clear-sky conditions is plotted against carbon oxidation state and double bond equivalent. Circles are colored by the log of the difference in VOC carbon flux magnitudes and sized according to the distance from log(Δflux) = 0. Labeled on each plot are the top contributors to Δflux.

Enhanced upward fluxes of reduced compounds (OS_c = -2; e.g., 232-MBO, isoprene, ΣMT) are observed during smoky days (**Fig. 8c**). This enhancement is only seen for species that are primarily emitted and do not have a strong physical sink, and reflects the higher (by 1.5 °C on average) daytime temperatures on these days relative to the clear days. Meanwhile, oxygenated VOCs that undergo bidirectional exchange, make up a large fraction of the VOC-C mass, and exhibit net emissions on clear days (e.g., acetone, hydroxyacetone, acetaldehyde, HCHO), have their upward fluxes reduced on smoky days due to higher exogeneous concentrations that increase their gross deposition. The warmer temperatures on smoky days also drives a minor change in $F_{\mathrm{ROH,up}}$ (of 0.92 cm s^{-2}), largely from isoprene (0.82 cm s^{-2}).

Downward fluxes for many other oxygenated VOCs were enhanced during smoke periods (**Fig. 8d**), in particular for species with DBE ≤ 2 and $OS_c \geq -1$. These include acetic acid, >C2 organic acids, anhydrides, a dihydroxycarbonyl compound from IEPOX oxidation ($C_4H_8O_3$) (Bates et al., 2016), isoprene-derived organonitrates ($C_4H_7NO_5$, $C_5H_9NO_4$, $C_5H_9NO_5$) (D'ambro et al., 2017; Tsiligiannis et al., 2022), and hydroxymethyl hydroperoxide (HMHP; CH_4O_3). The >C2 organic acids observed in this study include dicarboxylic acids and ketocarboxylic acids, which are found in smoke aerosol (Kundu et al., 2010) and in SOA generated from ponderosa pine (Tomaz et al., 2018). Species identified here as succinic acid ($C_4H_6O_4$) and acetic anhydride ($C_4H_6O_3$) may also include contributions from hydroxymethyl-methyl-a-lactone (HMML) and MVK hydroperoxyl-carbonyl (MVKPC), respectively, both isoprene oxidation products. Measured isoprene emissions increased during smoke periods, which would increase the abundance of these and other oxidation products. On average, the downward oxygenated VOC-C and OH reactivity fluxes increased by 56% and 49%, respectively, on smoky days.

3.5 Instrumental ion coverage

A novel aspect of this study was the combination of high-resolution PTRMS and ICIMS mass spectra for comprehensive VOC flux characterization over an ecosystem. In this section, we describe the contributions from each instrument to this coverage.

The PTRMS detected 97% of the net upward flux compared to 3% for the ICIMS, with the latter contribution primarily from HCOOH and $C_2H_4O_2$ (**Fig. S17**). Of the 23 top species making up 90% of the upward VOC-C flux, 21 were quantified by PTRMS; the remaining two (HCOOH and

$C_2H_4O_2$) were quantified by both ICIMS and PTRMS. The ICIMS played more of a role for the downward fluxes, capturing 37% of the total, although the PTR-MS still covered the majority (63%). The two largest individual contributors to the downward VOC-C flux ($C_3H_6O_2$ and HCHO; accounting for over 30% of the total) were both detected by PTRMS. The largest downward flux contributors measured by the ICIMS (collectively accounting for 25% of the total) included oxidation products of isoprene and of 232-MBO along with >C2 organic acids.

Meanwhile, the PTRMS captured over 98% of the total upward F_{ROH} and F_{RO3} and therefore a vast majority of the net reactivity flux in both cases. The 5 ions accounting for nearly 90% of $F_{\mathrm{ROH,up,obs}}$ and $F_{\mathrm{RO3,up,obs}}$ were all identified by PTRMS and are commonly reported using this instrument over forest ecosystems. Since the ICIMS detects more soluble oxidized products that undergo efficient deposition, it accounted for a larger share of the downward (55% of $F_{\mathrm{ROH,down,obs}}$ and 48% of $F_{\mathrm{RO3,down,obs}}$) than the upward reactivity fluxes.

In general, we find that the PTRMS detected the hydrocarbons and low molecular weight oxygenated VOCs representing the bulk of the total observed VOC mass and reactivity fluxes. PTRMS measurements can therefore be used alone to provide near-complete coverage of net VOC-C fluxes and their impacts on atmospheric reactivity over this and similar ecosystems. However, ICIMS-detected species made up a significant fraction of the downward VOC fluxes, and therefore provide key information for constraining this major sink of atmospheric reactive carbon. The ICIMS also captured a wide suite of VOC oxidation products for diagnosing the chemical fate of emitted species.

While the combination of PTRMS and ICIMS provides comprehensive observational coverage for VOCs controlling atmospheric reactive carbon abundance and reactivity, the sampling configuration used here would not capture some compounds with very high volatility (e.g., low molecular weight hydrocarbons) or very low volatility (e.g., highly oxygenated organic molecules, HOM). A previous study at this site used relaxed eddy accumulation sampling with gas chromatography-flame ionization detection to quantify summertime emissions of ethene, propene, butene and isoprene (Rhew et al., 2017). Ethene and propene fluxes together averaged ~2 x 10^{11} atoms C cm^{-2} s^{-1}, over an order of magnitude lower than the upward VOC-C fluxes observed in this study, and their associated reactivity fluxes would likewise be small (F_{ROH} ~0.7 cm s^{-2} and F_{RO3} ~4 x 10^{-7} cm s^{-2}). In the case of lower-volatility compounds, Hunter et al. (2017) found that semivolatile and intermediate-volatility organic species not detected by PTRMS or ICIMS accounted for ~10% of the total observed organic carbon concentration at MEFO. Future studies employing atmospheric pressure interface time-of-flight mass spectrometry (Riva et al., 2018) or analogous techniques could help to elucidate the contributions of such species to forest-atmosphere VOC-C exchange.

4. Conclusions

Detailed measurements are needed to understand the two-way flux of VOCs between ecosystems and the atmosphere, the resulting effects on air quality, and how well that exchange is represented in models. This study provided the most comprehensive look yet at terrestrial VOC fluxes by employing two high-resolution mass spectrometers (PTRMS and ICIMS, deployed over a temperate coniferous forest) to calculate EC fluxes across the entire mass spectrum for both instruments. Of the 1261 total ions identified as VOCs, 315 exhibited detectable fluxes; 23 and 125 of these ions were required to capture 90% of the total upward and downward VOC-carbon fluxes, respectively.

Net VOC-C exchange was dominated by the upward fluxes at this site, with PTRMS-detected species accounting for 97% of the total upward flux and 63% of the total downward flux. Comparing the observations to predictions from the GEOS-Chem CTM, we find that the model was able to capture the magnitude and much of the temporal variability in the aggregated net and upward VOC-C fluxes with only modest biases. However, the model underestimated the downward VOC-C fluxes by over a factor of four, primarily due to large concentration underestimates for many relevant oxygenated VOCs. Many of these species were detected by ICIMS, highlighting the need such measurements to fully characterize VOC deposition and fate.

Along with the VOC mass fluxes, OH and O_3 reactivity fluxes were quantified to diagnose the impacts of the measured exchange on atmospheric chemistry. The net OH and O_3 reactivity fluxes (like the mass fluxes) were primarily carried by a small number of emitted species that were detected by the PTRMS and explicitly represented in the GEOS-Chem mechanism. A total of 5 and 108 ions were required to capture 90% of the upward and downward OH reactivity fluxes, respectively, fewer than in the case of the VOC-C fluxes. 232-MBO accounted for ~70% of the OH reactivity flux and should be included in CTMs. Model biases in the simulated OH reactivity fluxes primarily arose from a 232-MBO underestimate and from a missing isoprene source from the forest floor. O_3 reactivity fluxes were dominated by ∑SQT and ∑MT and were overwhelmingly (>98%) composed of PTRMS-measured species. We recommend explicit representation of ∑SQT in CTM mechanisms to correctly represent near-surface O_3 loss.

The GEOS-Chem model was generally successful in simulating the canopy-scale dependence of VOC fluxes on temperature and sunlight for T < 295 K, but strongly overpredicted the flux-temperature sensitivity under hotter conditions. It also failed to capture the enhanced terpenoid emissions that occurred on rainy days. Overall, the main model-measurement disparities identified here were driven by biases for species that are already accounted-for in CTMs rather than by missing species. Better model performance was achieved for the net and upward VOC-C and reactivity fluxes than for the downward fluxes. This is partly because the upward fluxes were dominated by a few major species (all of which have explicit CTM representation), and partly because of offsetting model errors between those major species.

This work has provided a chemically detailed analysis of VOC surface-atmosphere exchange for one pine forest ecosystem, and builds upon a small number of similar studies that relied solely upon PTRMS (Loubet et al., 2022; Millet et al., 2018; Park et al., 2013). Further measurements employing multiple high-resolution mass spectrometers in different ecosystems are required to better understand surface-atmosphere VOC fluxes across the full suite of relevant compounds, diagnose the underlying environmental drivers, and advance the ability of current CTMs to capture the ensuing impact on atmospheric chemistry.

Acknowledgements

This work was supported by NSF AGS 1932771 and 1932849. Measurement capabilities at UMN were also enhanced by support from the Alfred P. Sloan Foundation. The tower used in this project is maintained by NCAR and supported by the USFS. We thank Steven Alton and Paula Fornwalt of USFS for their support with site and logistics. We also thank Glenn M. Wolfe for publicly providing the MATLAB-based FluxToolbox of analysis scripts, portions of which were altered for use in this analysis. Computing resources were provided by the Minnesota Supercomputing Institute (http://www.msi.umn.edu) at the University of Minnesota. We acknowledge that this project occurred on the traditional territory of the Ute and Cheyenne peoples.

Data Availability Statement

Observed and simulated total VOC-C and reactivity fluxes (net, upward, and downward) and associated meteorological observations can be accessed at https://atmoschem.umn.edu/data. This data will be permanently archived with a DOI at https://conservancy.umn.edu/ at the time of publication. GEOS-Chem model code is publicly available at http://www.geos-chem.org. The FluxToolBox code is archived at https://github.com/AirChem.

References

Arneth, A., Schurgers, G., Lathiere, J., Duhl, T., Beerling, D. J., Hewitt, C. N., et al. (2011). Global terrestrial isoprene emission models: Sensitivity to variability in climate and vegetation. *Atmospheric Chemistry and Physics*, *11*(15), 8037–8052. https://doi.org/10.5194/ACP-11-8037-2011

Atkinson, R, Baulch, D. L., Cox, R. A., Crowley, J. N., Hampson, R. F., Hynes, R. G., et al. (2006). Atmospheric Chemistry and Physics Evaluated kinetic and photochemical data for atmospheric chemistry: Volume II-gas phase reactions of organic species The IUPAC Subcommittee on Gas Kinetic Data Evaluation for Atmospheric Chemistry. *Atmos. Chem. Phys*, *6*, 3625–4055. Retrieved from www.atmos-chem-phys.net/6/3625/2006/

Atkinson, R. & Arey, J. (2003). Atmospheric Degradation of Volatile Organic Compounds. *Chemical Reviews*, *103*(12), 4605–4638. https://doi.org/10.1021/CR0206420/ASSET/IMAGES/MEDIUM/CR0206420E00019.GIF

Atkinson, R., Aschmann, S. M., & Arey, J. (1990). Rate constants for the gas-phase reactions of OH and NO3 radicals and O3 with sabinene and camphene at 296±2 K. *Atmospheric Environment Part A, General Topics*, *24*(10), 2647–2654. https://doi.org/10.1016/0960-1686(90)90144-C

Bates, K. H., & Jacob, D. J. (2019). A new model mechanism for atmospheric oxidation of isoprene: Global effects on oxidants, nitrogen oxides, organic products, and secondary organic aerosol. *Atmospheric Chemistry and Physics*, *19*(14), 9613–9640. https://doi.org/10.5194/ACP-19-9613-2019

Bates, K. H., Nguyen, T. B., Teng, A. P., Crounse, J. D., Kjaergaard, H. G., Stoltz, B. M., et al. (2016). Production and Fate of C4 Dihydroxycarbonyl Compounds from Isoprene Oxidation. *Journal of Physical Chemistry A*, *120*(1), 106–117. https://doi.org/10.1021/ACS.JPCA.5B10335/ASSET/IMAGES/LARGE/JP-2015-10335X_0009.JPEG

Bates, K. H., Jacob, D. J., Wang, S., Hornbrook, R. S., Apel, E. C., Kim, M. J., et al. (2021). The Global Budget of Atmospheric Methanol: New Constraints on Secondary, Oceanic, and Terrestrial Sources. *Journal of Geophysical Research: Atmospheres*, *126*(4), e2020JD033439. https://doi.org/10.1029/2020JD033439

Beaver, M. R., St. Clair, J. M., Paulot, F., Spencer, K. M., Crounse, J. D., Lafranchi, B. W., et al. (2012). Importance of biogenic precursors to the budget of organic nitrates: Observations of multifunctional organic nitrates by CIMS and TD-LIF during BEARPEX 2009. *Atmospheric Chemistry and Physics*, *12*(13), 5773–5785. https://doi.org/10.5194/ACP-12-5773-2012

Berkelhammer, M., Noone, D. C., Wong, T. E., Burns, S. P., Knowles, J. F., Kaushik, A., et al. (2016). Convergent approaches to determine an ecosystem's transpiration fraction. *Global Biogeochemical Cycles*, *30*(6), 933–951. https://doi.org/10.1002/2016GB005392

Bertram, T. H., Kimmel, J. R., Crisp, T. a., Ryder, O. S., Yatavelli, R. L. N., Thornton, J. a., et al. (2011). A field-deployable, chemical ionization time-of-flight mass spectrometer. *Atmospheric Measurement Techniques*, *4*(7), 1471–1479. https://doi.org/10.5194/amt-4-1471-2011

Bessagnet, B., Seigneur, C., & Menut, L. (2010). Impact of dry deposition of semi-volatile organic compounds on secondary organic aerosols. *Atmospheric Environment*, *44*, 1781–1787. https://doi.org/10.1016/j.atmosenv.2010.01.027

Bi, C., Krechmer, J. E., Frazier, G. O., Xu, W., Lambe, A. T., Claflin, M. S., et al. (2021). Quantification of isomer-resolved iodide chemical ionization mass spectrometry sensitivity and uncertainty using a voltage-scanning approach. *Atmospheric Measurement Techniques*, *14*(10), 6835–6850. https://doi.org/10.5194/AMT-14-6835-2021

Boucher, O., Randall, D., Artaxo, P., Bretherton, C., Feingold, G., Forster, P., et al. (2013). Climate change 2013: the physical science basis. Contribution of Working Group I to the Fifth Assessment Report of the Intergovernmental Panel on Climate Change. *K., Tignor, M., Allen, SK, Boschung, J., Nauels, A., Xia, Y., Bex, V., and Midgley, PM, Cambridge University Press, Cambridge, UK*.

Bourtsoukidis, E., Williams, J., Kesselmeier, J., Jacobi, S., & Bonn, B. (2014). From emissions to ambient mixing ratios: Online seasonal field measurements of volatile organic compounds over a Norway spruce-dominated forest in central Germany. *Atmospheric Chemistry and Physics*, *14*(13), 6495–6510. https://doi.org/10.5194/acp-14-6495-2014

Brophy, P., & Farmer, D. K. (2015). A switchable reagent ion high resolution time-of-flight chemical ionization mass spectrometer for real-time measurement of gas phase oxidized species: Characterization from the 2013 southern oxidant and aerosol study. *Atmospheric Measurement Techniques*, *8*(7), 2945–2959. https://doi.org/10.5194/AMT-8-2945-2015

Byrne, K. A., Kiely, G., & Leahy, P. (2005). CO_2 fluxes in adjacent new and permanent temperate grasslands. *Agricultural and Forest Meteorology*, *135*(1–4), 82–92. https://doi.org/10.1016/J.AGRFORMET.2005.10.005

Canagaratna, M. R., Jimenez, J. L., Kroll, J. H., Chen, Q., Kessler, S. H., Massoli, P., et al. (2015). Elemental ratio measurements of organic compounds using aerosol mass spectrometry: Characterization, improved calibration, and implications. *Atmospheric Chemistry and Physics*, *15*(1), 253–272. https://doi.org/10.5194/ACP-15-253-2015

Chan, A. W. H., Kreisberg, N. M., Hohaus, T., Campuzano-Jost, P., Zhao, Y., Day, D. A., et al. (2016). Speciated measurements of semivolatile and intermediate volatility organic compounds (S/IVOCs) in a pine forest during BEACHON-RoMBAS 2011. *Atmos. Chem. Phys*, *16*, 1187–1205. https://doi.org/10.5194/acp-16-1187-2016

Chen, H., Ren, Y., Cazaunau, M., Daële, V., Hu, Y., Chen, J., & Mellouki, A. (2015). Rate coefficients for the reaction of ozone with 2-and 3-carene. *Chemical Physics Letters*, *621*, 71–77. https://doi.org/10.1016/j.cplett.2014.12.056

Chen, X., Millet, D. B., Singh, H. B., Wisthaler, A., Apel, E. C., Atlas, E. L., et al. (2019). On the sources and sinks of atmospheric VOCs: an integrated analysis of recent aircraft campaigns over North America. *Atmospheric Chemistry and Physics*, *19*(14), 9097–9123. https://doi.org/10.5194/ACP-19-9097-2019

Coggon, M. M., Lim, C. Y., Koss, A. R., Sekimoto, K., Yuan, B., Gilman, J. B., et al. (2019). OH chemistry of non-methane organic gases (NMOGs) emitted from laboratory and ambient biomass burning smoke: Evaluating the influence of furans and oxygenated aromatics on ozone and secondary NMOG formation. *Atmospheric Chemistry and Physics*, *19*(23), 14875–14899. https://doi.org/10.5194/ACP-19-14875-2019

D'ambro, E. L., Lee, B. H., Liu, J., Shilling, J. E., Gaston, C. J., Lopez-Hilfiker, F. D., et al. (2017). Molecular composition and volatility of isoprene photochemical oxidation secondary organic aerosol under low-and high-NO x conditions. *Atmos. Chem. Phys*, *17*, 159–174. https://doi.org/10.5194/acp-17-159-2017

DeCarlo, P. F., Kimmel, J. R., Trimborn, A., Northway, M. J., Jayne, J. T., Aiken, A. C., et al. (2006). Field-deployable, high-resolution, time-of-flight aerosol mass spectrometer. *Analytical Chemistry*, *78*(24), 8281–8289. https://doi.org/10.1021/AC061249N/SUPPL_FILE/AC061249NSI20060905_075156.PDF

Donahue, N. M., Chuang, W., Epstein, S. A., Kroll, J. H., Worsnop, D. R., Robinson, A. L., et al. (2013). Why do organic aerosols exist? Understanding aerosol lifetimes using the two-dimensional volatility basis set. *Environmental Chemistry*, *10*(3), 151–157. https://doi.org/10.1071/EN13022

Fantechi, G., Jensen, N. R., Hjorth, J., & Peeters, J. (1998). Mechanistic studies of the atmospheric oxidation of methyl butenol by OH radicals, ozone and NO3 radicals. *Atmospheric Environment*, *32*(20), 3547–3556. https://doi.org/10.1016/S1352-2310(98)00061-2

Ferronato, C., Orlando, J. J., & Tyndall, G. S. (1998). Rate and mechanism of the reactions of OH and Cl with 2-methyl-3-buten-2-ol. *Journal of Geophysical Research: Atmospheres*, *103*(D19), 25579–25586. https://doi.org/10.1029/98JD00528

Fischer, L., Breitenlechner, M., Canaval, E., Scholz, W., Striednig, M., Graus, M., et al. (2021). First eddy covariance flux measurements of semi-volatile organic compounds with the PTR3-TOF-MS. *Atmospheric Measurement Techniques*, *14*(12), 8019–8039. https://doi.org/10.5194/AMT-14-8019-2021

Fisher, J. A., Atlas, E. L., Barletta, B., Meinardi, S., Blake, D. R., Thompson, C. R., et al. (2018). Methyl, Ethyl, and Propyl Nitrates: Global Distribution and Impacts on Reactive Nitrogen in Remote Marine Environments. *Journal of Geophysical Research: Atmospheres*, *123*(21), 12,429-12,451. https://doi.org/10.1029/2018JD029046

Foken, T., & Wichura, B. (1996). Tools for quality assessment of surface-based flux measurements. *Agricultural and Forest Meteorology*, *78*(1–2), 83–105. https://doi.org/10.1016/0168-1923(95)02248-1

Fulgham, S. R., Brophy, P., Link, M., Ortega, J., Pollack, I., & Farmer, D. K. (2019). Seasonal Flux Measurements over a Colorado Pine Forest Demonstrate a Persistent Source of Organic Acids. *ACS Earth and Space Chemistry*, *3*(9), 2017–2032. research-article. https://doi.org/10.1021/acsearthspacechem.9b00182

Giglio, L., Randerson, J. T., & Van Der Werf, G. R. (2013). Analysis of daily, monthly, and annual burned area using the fourth-generation global fire emissions database (GFED4). *Journal of Geophysical Research: Biogeosciences*, *118*(1), 317–328. https://doi.org/10.1002/JGRG.20042

Gilman, J. B., Lerner, B. M., Kuster, W. C., Goldan, P. D., Warneke, C., Veres, P. R., et al. (2015). Biomass burning emissions and potential air quality impacts of volatile organic compounds and other trace gases from fuels common in the US. *Atmospheric Chemistry and Physics*, *15*(24), 13915–13938. https://doi.org/10.5194/ACP-15-13915-2015

Glasius, M., & Goldstein, A. H. (2016). Recent Discoveries and Future Challenges in Atmospheric Organic Chemistry. *Environmental Science and Technology*, *50*(6), 2754–2764. https://doi.org/10.1021/ACS.EST.5B05105/ASSET/IMAGES/LARGE/ES-2015-051053_0003.JPEG

Goldstein, A. H., & Galbally, I. E. (2007). Known and unexplored organic constituents in the earth's atmosphere. *Environmental Science and Technology*, *41*(5), 1514–1521. https://doi.org/10.1021/es072476p

Grosjean, D., Grosjean, E., & Williams, E. L. (1993). Rate constants for the gas-phase reactions of ozone with unsaturated alcohols, esters, and carbonyls. *International Journal of Chemical Kinetics*, *25*(9), 783–794. https://doi.org/10.1002/KIN.550250909

Grosjean, E., & Grosjean, D. (1999). Rate Constants for the Gas-Phase Reaction of Ozone with Unsaturated Oxygenates. *International Journal of Chemical Kinetics*, *30*, 21–29. https://doi.org/10.1002/(SICI)1097-4601(1998)30:1

Guenther, A., Karl, T., Harley, P., Wiedinmyer, C., Palmer, P. I., & Geron, C. (2006). Estimates of global terrestrial isoprene emissions using MEGAN (Model of Emissions of Gases and Aerosols from Nature). *Atmospheric Chemistry and Physics*, *6*(11), 3181–3210. https://doi.org/10.5194/acp-6-3181-2006

Guenther, A., Jiang, X., Heald, C. L., Sakulyanontvittaya, T., Duhl, T., Emmons, L. K., & Wang, X. (2012). The model of emissions of gases and aerosols from nature version 2.1 (MEGAN2.1): An extended and updated framework for modeling biogenic emissions. *Geoscientific Model Development*, *5*(6), 1471–1492. https://doi.org/10.5194/gmd-5-1471-2012

Guenther, A., Jiang, X., Shah, T., Huang, L., Kemball-Cook, S., & Yarwood, G. (2020). Model of Emissions of Gases and Aerosol from Nature Version 3 (MEGAN3) for Estimating Biogenic Emissions BT - Air Pollution Modeling and its Application XXVI. In C. Mensink, W. Gong, & A. Hakami (Eds.) (pp. 187–192). Cham: Springer International Publishing.

Heikes, B. G. (2002). Atmospheric methanol budget and ocean implication. *Global Biogeochemical Cycles*, *16*(4), 1–13. https://doi.org/10.1029/2002GB001895

Helmig, D., Greenberg, J., Guenther, A., Zimmerman, P., & Geron, C. (1998). Volatile organic compounds and isoprene oxidation products at a temperate deciduous forest site. *Journal of Geophysical Research: Atmospheres*, *103*(D17), 22397–22414. https://doi.org/10.1029/98JD00969

Helmig, D., Ortega, J., Duhl, T., Tanner, D., Guenther, A., Harley, P., et al. (2007). Sesquiterpene emissions from pine trees - Identifications, emission rates and flux estimates for the contiguous United States. *Environmental Science and Technology*, *41*(5), 1545–1553. https://doi.org/10.1021/es0618907

Hoesly, R. M., Smith, S. J., Feng, L., Klimont, Z., Janssens-Maenhout, G., Pitkanen, T., et al. (2018). Historical (1750-2014) anthropogenic emissions of reactive gases and aerosols from the Community Emissions Data System (CEDS). *Geoscientific Model Development*, *11*(1), 369–408. https://doi.org/10.5194/GMD-11-369-2018

Holzinger, R. (2015). PTRwid: A new widget tool for processing PTR-TOF-MS data. *Atmospheric Measurement Techniques*, *8*(9), 3903–3922. https://doi.org/10.5194/AMT-8-3903-2015

Holzinger, R., Lee, A., Mckay, M., & Goldstein, A. H. (2006). *Atmospheric Chemistry and Physics Seasonal variability of monoterpene emission factors for a Ponderosa pine plantation in California*. *Atmos. Chem. Phys* (Vol. 6). Retrieved from www.atmos-chem-phys.net/6/1267/2006/

Hu, L., Millet, D. B., Baasandorj, M., Griffis, T. J., Turner, P., Helmig, D., et al. (2015). Isoprene emissions and impacts over an ecological transition region in the U.S. Upper Midwest inferred from tall tower measurements. *Journal of Geophysical Research: Atmospheres*, *120*(8), 3553–3571. https://doi.org/10.1002/2014JD022732

Huang, G., Brook, R., Crippa, M., Janssens-Maenhout, G., Schieberle, C., Dore, C., et al. (2017). Speciation of anthropogenic emissions of non-methane volatile organic compounds: a global gridded data set for 1970-2012. *Atmospheric Chemistry and Physics Discussions*, 1–36. https://doi.org/10.5194/acp-2017-65

Hunter, J. F., Day, D. A., Palm, B. B., Yatavelli, R. L. N., Chan, A. W. H., Kaser, L., et al. (2017). Comprehensive characterization of atmospheric organic carbon at a forested site. *Nature Geoscience 2017 10:10*, *10*(10), 748–753. https://doi.org/10.1038/ngeo3018

Isaacman-Vanwertz, G., Massoli, P., O'Brien, R., Lim, C., Franklin, J. P., Moss, J. A., et al. (2018). Chemical evolution of atmospheric organic carbon over multiple generations of oxidation. *Nature Chemistry 2018 10:4*, *10*(4), 462–468. https://doi.org/10.1038/s41557-018-0002-2

Iyer, S., Lopez-Hilfiker, F., Lee, B. H., Thornton, J. A., & Kurtén, T. (2016). Modeling the Detection of Organic and Inorganic Compounds Using Iodide-Based Chemical Ionization.

Jacob, D. J., Field, B. D., Jin, E. M., Bey, I., Li, Q., Logan, J. A., et al. (2002). Atmospheric budget of acetone. *Journal of Geophysical Research: Atmospheres*, *107*(9–10). https://doi.org/10.1029/2001jd000694

Karl, T., Hansel, a., Cappellin, L., Kaser, L., Herdlinger-Blatt, I., & Jud, W. (2012). Selective measurements of isoprene and 2-methyl-3-buten-2-ol based on NO+ ionization mass spectrometry. *Atmospheric Chemistry and Physics*, *12*(24), 11877–11884. https://doi.org/10.5194/acp-12-11877-2012

Karl, T., Kaser, L., & Turnipseed, A. (2014). Eddy covariance measurements of isoprene and 232-MBO based on NO + time-of-flight mass spectrometry. *International Journal of Mass Spectrometry*, *365–366*, 15–19. https://doi.org/10.1016/j.ijms.2013.12.002

Kaser, L., Karl, T., Guenther, A., Graus, M., Schnitzhofer, R., Turnipseed, A., et al. (2013a). Undisturbed and disturbed above canopy ponderosa pine emissions: PTR-TOF-MS measurements and MEGAN 2.1 model results. *Atmospheric Chemistry and Physics*, *13*(23), 11935–11947. https://doi.org/10.5194/acp-13-11935-2013

Kaser, L., Karl, T., Schnitzhofer, R., Graus, M., Herdlinger-Blatt, I. S., DiGangi, J. P., et al. (2013b). Comparison of different real time VOC measurement techniques in a ponderosa pine forest. *Atmospheric Chemistry and Physics*, *13*(5), 2893–2906. https://doi.org/10.5194/acp-13-2893-2013

Kim, D., Stevens, P. S., & Hites, R. A. (2011). Rate constants for the gas-phase reactions of OH and O 3 with β-ocimene,β-myrcene, and α-and β-farnesene as a function of temperature. *Journal of Physical Chemistry A*, *115*(4), 500–506. https://doi.org/10.1021/jp111173s

Kim, S., Karl, T., Guenther, A., Tyndall, G., Orlando, J., Harley, P., et al. (2010). Emissions and ambient distributions of Biogenic Volatile Organic Compounds (BVOC) in a ponderosa pine ecosystem: Interpretation of PTR-MS mass spectra. *Atmospheric Chemistry and Physics*, *10*(4), 1759–1771. https://doi.org/10.5194/acp-10-1759-2010

Kroll, J. H., Donahue, N. M., Jimenez, J. L., Kessler, S. H., Canagaratna, M. R., Wilson, K. R., et al. (2011). Carbon oxidation state as a metric for describing the chemistry of atmospheric organic aerosol. *Nat. Chem.*, *3*(2), 133. https://doi.org/10.1038/nchem.948

Kundu, S., Kawamura, K., Andreae, T. W., Hoffer, A., & Andreae, M. O. (2010). Molecular distributions of dicarboxylic acids, ketocarboxylic acids and α-dicarbonyls in biomass burning aerosols: Implications for photochemical production and degradation in smoke layers. *Atmospheric Chemistry and Physics*, *10*(5), 2209–2225. https://doi.org/10.5194/ACP-10-2209-2010

Lamb, B., Westberg, H., Allwine, G., & Quarles, T. (1985). Biogenic hydrocarbon emissions from deciduous and coniferous trees in the United States. *Journal of Geophysical Research*, *90*, 2380–2390. https://doi.org/10.1029/JD090iD01p02380

Lary, D. J., & Shallcross, D. E. (2000). Central role of carbonyl compounds in atmospheric chemistry. *Journal of Geophysical Research Atmospheres*, *105*(D15), 19771–19778. https://doi.org/10.1029/1999JD901184

Lee, A., Goldstein, A. H., Keywood, M. D., Gao, S., Varutbangkul, V., Bahreini, R., et al. (2006). Gas-phase products and secondary aerosol yields from the ozonolysis of ten different terpenes. *Journal of Geophysical Research Atmospheres*, *111*(7), 1–18. https://doi.org/10.1029/2005JD006437

Lee, B. H., Lopez-hilfiker, F. D., Mohr, C., Kurten, T., Worsnop, D. R., & Joel, A. (2014). An Iodide-Adduct High-Resolution Time-of-Flight Chemical- Ionization Mass Spectrometer: Application to Atmospheric Inorganic and Organic Compounds. *Environ.Sci. Technol.*, *48*, 6309–6317. https://doi.org/10.1021/es500362a

Lee, X., Massman, W. J., & Law, B. (2005). Handbook of Micrometeorology. *Handbook of Micrometeorology*, *29*, 250. Retrieved from https://books.google.com/books/about/Handbook_of_Micrometeorology.html?id=IJ_19RkTfBQC

Lin, H., Jacob, D. J., Lundgren, E. W., Sulprizio, M. P., Keller, C. A., Fritz, T. M., et al. (2021). Harmonized Emissions Component (HEMCO) 3.0 as a versatile emissions component for atmospheric models: Application in the GEOS-Chem, NASA GEOS, WRF-GC, CESM2, NOAA GEFS-Aerosol, and NOAA UFS models. *Geoscientific Model Development*, *14*(9), 5487–5506. https://doi.org/10.5194/GMD-14-5487-2021

Link, M. F., Brophy, P., Fulgham, S. R., Murschell, T., & Farmer, D. K. (2021). Isoprene versus Monoterpenes as Gas-Phase Organic Acid Precursors in the Atmosphere. *ACS Earth and Space Chemistry*, *5*(6), 1600–1612. https://doi.org/10.1021/ACSEARTHSPACECHEM.1C00093/ASSET/IMAGES/LARGE/SP1C00093_0010.JPEG

Lopez-Hilfiker, F. D., Mohr, C., Ehn, M., Rubach, F., Kleist, E., Wildt, J., et al. (2014). A novel method for online analysis of gas and particle composition: Description and evaluation of a filter inlet for gases and AEROsols (FIGAERO). *Atmospheric Measurement Techniques*, *7*(4), 983–1001. https://doi.org/10.5194/AMT-7-983-2014

Lopez-Hilfiker, F. D., Iyer, S., Mohr, C., Lee, B. H., D'Ambro, E. L., Kurtén, T., & Thornton, J. a. (2015). Constraining the sensitivity of iodide adduct chemical ionization mass spectrometry to multifunctional organic molecules using the collision limit and thermodynamic stability of iodide ion adducts. *Atmospheric Measurement Techniques Discussions*, *8*(10), 10875–10896. https://doi.org/10.5194/amtd-8-10875-2015

Loubet, B., Buysse, P., Gonzaga-Gomez, L., Lafouge, F., Ciuraru, R., Decuq, C., et al. (2022). Volatile organic compound fluxes over a winter wheat field by PTR-Qi-TOF-MS and eddy covariance. *Atmospheric Chemistry and Physics*, *22*(4), 2817–2842. https://doi.org/10.5194/ACP-22-2817-2022

Mattila, J. M., Brophy, P., Kirkland, J., Hall, S., Ullmann, K., Fischer, E. V., et al. (2018). Tropospheric sources and sinks of gas-phase acids in the Colorado Front Range. *Atmospheric Chemistry and Physics*, *18*(16), 12315–12327. https://doi.org/10.5194/ACP-18-12315-2018

Mattila, J. M., Lakey, P. S. J., Shiraiwa, M., Wang, C., Abbatt, J. P. D., Arata, C., et al. (2020). Multiphase Chemistry Controls Inorganic Chlorinated and Nitrogenated Compounds in Indoor Air during Bleach Cleaning. *Environmental Science and Technology*, *54*(3), 1730–1739. https://doi.org/10.1021/ACS.EST.9B05767/ASSET/IMAGES/MEDIUM/ES9B05767_M012.GIF

Mauder, M., Cuntz, M., Drüe, C., Graf, A., Rebmann, C., Schmid, H. P., et al. (2013). A strategy for quality and uncertainty assessment of long-term eddy-covariance measurements. *Agricultural and Forest Meteorology*, *169*, 122–135. https://doi.org/10.1016/J.AGRFORMET.2012.09.006

Mellouki, A., Wallington, T. J., & Chen, J. (2015). Atmospheric Chemistry of Oxygenated Volatile Organic Compounds: Impacts on Air Quality and Climate. *Chemical Reviews*, *115*(10), 3984–4014. https://doi.org/10.1021/cr500549n

Millet, D. B., Jacob, D. J., Custer, T. G., De Gouw, J. A., Goldstein, A. H., Karl, T., et al. (2008). New constraints on terrestrial and oceanic sources of atmospheric methanol. *Atmospheric Chemistry and Physics*, *8*(23), 6887–6905. https://doi.org/10.5194/acp-8-6887-2008

Millet, D. B., Baasandorj, M., Farmer, D. K., Thornton, J. A., Baumann, K., Brophy, P., et al. (2015). A large and ubiquitous source of atmospheric formic acid. *Atmospheric Chemistry and Physics*, *15*(11), 6283–6304. https://doi.org/10.5194/acp-15-6283-2015

Millet, D. B., Guenther, A., Siegel, D. A., Nelson, N. B., Singh, H. B., Gouw, J. A. De, et al. (2010). Global atmospheric budget of acetaldehyde : 3-D model analysis and constraints from in-situ and satellite observations. *Atmospheric Chemistry and Physics*, *10*, 3405–3425.

Millet, D. B., Alwe, H. D., Chen, X., Deventer, M. J., Griffis, T. J., Holzinger, R., et al. (2018). Bidirectional Ecosystem-Atmosphere Fluxes of Volatile Organic Compounds Across the Mass Spectrum: How Many Matter? *ACS Earth and Space Chemistry*, *2*(8), 764–777. https://doi.org/10.1021/acsearthspacechem.8b00061

Muller, J.-F., & Brasseur, G. (1999). Source of upper tropospheric HOx: A three-dimensional study. *Journal of Geophysical Research*, *104*, 1705–1715.

Müller, M., Mikoviny, T., Jud, W., D'Anna, B., & Wisthaler, A. (2013). A new software tool for the analysis of high resolution PTR-TOF mass spectra. *Chemometrics and Intelligent Laboratory Systems*, *127*, 158–165. https://doi.org/10.1016/J.CHEMOLAB.2013.06.011

Nguyen, T. B., Crounse, J. D., Teng, A. P., St Clair, J. M., Paulot, F., Wolfe, G. M., & Wennberg, P. O. (2015). Rapid deposition of oxidized biogenic compounds to a temperate forest. *Proceedings of the National Academy of Sciences of the United States of America*, *112*(5), E392-401. https://doi.org/10.1073/pnas.1418702112

Olson, D. M., Dinerstein, E., Wikramanayake, E. D., Burgess, N. D., Powell, G. V. N., Underwood, E. C., et al. (2001). Terrestrial ecoregions of the world: A new map of life on Earth. *BioScience*, *51*(11), 933–938. https://doi.org/10.1641/0006-3568(2001)051[0933:TEOTWA]2.0.CO;2

Ortega, J., Turnipseed, A., Guenther, A. B., Karl, T. G., Day, D. A., Gochis, D., et al. (2014). Overview of the Manitou experimental forest observatory: Site description and selected science results from 2008 to 2013. *Atmospheric Chemistry and Physics*, *14*(12), 6345–6367. https://doi.org/10.5194/acp-14-6345-2014

Pagonis, D., Sekimoto, K., & de Gouw, J. (2019). A Library of Proton-Transfer Reactions of H3O+ Ions Used for Trace Gas Detection. *Journal of the American Society for Mass Spectrometry*, *30*(7), 1330–1335. https://doi.org/10.1007/S13361-019-02209-3/SUPPL_FILE/JS8B06050_SI_001.XLSX

Park, J. H., Goldstein, A. H., Timkovsky, J., Fares, S., Weber, R., Karlik, J., & Holzinger, R. (2013). Active atmosphere-ecosystem exchange of the vast majority of detected volatile organic compounds. *Science*, *341*(6146), 643–647. https://doi.org/10.1126/science.1235053

Philip, S., Martin, R. V., & Keller, C. A. (2016). Sensitivity of chemistry-transport model simulations to the duration of chemical and transport operators: A case study with GEOS-Chem v10-01. *Geoscientific Model Development*, *9*(5), 1683–1695. https://doi.org/10.5194/GMD-9-1683-2016

Reissell, A., Arey, J., & Atkinson, R. (2000). Atmospheric Chemistry of Camphor. *Int J Chem Kinet*, *33*, 56–63. https://doi.org/10.1002/1097-4601

Rhew, R. C., Deventer, M. J., Turnipseed, A. A., Warneke, C., Ortega, J., Shen, S., et al. (2017). Ethene, propene, butene and isoprene emissions from a ponderosa pine forest measured by relaxed eddy accumulation. *Atmospheric Chemistry and Physics*, *17*(21), 13417–13438. https://doi.org/10.5194/acp-17-13417-2017

Riches, M., Lee, D., & Farmer, D. K. (2020). Simultaneous leaf-level measurement of trace gas emissions and photosynthesis with a portable photosynthesis system. *Atmospheric Measurement Techniques*, *13*(8), 4123–4139. https://doi.org/10.5194/AMT-13-4123-2020

Richters, S., Herrmann, H., & Berndt, T. (2015). Gas-phase rate coefficients of the reaction of ozone with four sesquiterpenes at 295 ± 2 K. *Physical Chemistry Chemical Physics*, *17*(17), 11658–11669. https://doi.org/10.1039/c4cp05542j

Riva, M., Rantala, P., Krechmer, J. E., Peräkylä, O., Zhang, Y., Heikkinen, L., et al. (2018). Evaluating the performance of five different chemical ionization techniques for detecting gaseous oxygenated organic species. *Atmospheric Measurement Techniques Discussions*, 1–39. https://doi.org/10.5194/amt-2018-407

Safieddine, S. A., Heald, C. L., & Henderson, B. H. (2017). The global nonmethane reactive organic carbon budget: A modeling perspective. *Geophysical Research Letters*, *44*(8), 3897–3906. https://doi.org/10.1002/2017GL072602

Sander, R. (2015). Compilation of Henry's law constants (version 4.0) for water as solvent. *Atmospheric Chemistry and Physics*, *15*(8), 4399–4981. https://doi.org/10.5194/acp-15-4399-2015

Saunders, S. M., Jenkin, M. E., Derwent, R. G., & Pilling, M. J. (2003). Protocol for the development of the Master Chemical Mechanism, MCM v3 (Part A): Tropospheric degradation of non-aromatic volatile organic compounds. *Atmospheric Chemistry and Physics*, *3*(1), 161–180. https://doi.org/10.5194/acp-3-161-2003

Schade, G. W., Goldstein, A. H., & Lamanna, M. S. (1999). Are Monoterpene Emissions influenced by Humidity? *Geophysical Research Letters*, *26*(14), 2187–2190. https://doi.org/10.1029/1999GL900444

Sindelarova, K., Granier, C., Bouarar, I., Guenther, A., Tilmes, S., Stavrakou, T., et al. (2014). Global data set of biogenic VOC emissions calculated by the MEGAN model over the last 30 years. *Atmospheric Chemistry and Physics*, *14*(17), 9317–9341. https://doi.org/10.5194/acp-14-9317-2014

Singh, H. B., Kanakidou, M., Crutzen, P. J., & Jacob, D. J. (1995). High concentrations and photochemical fate of oxygenated hydrocarbons in the global troposphere. *Nature*, *378*(6552), 50–54. https://doi.org/10.1038/378050a0

Stedman, D. H., & Niki, H. (1973). Ozonolysis Rates of Some Atmospheric Gases. *Http://Dx.Doi.Org/10.1080/00139307309435501*, *4*(4), 303–310. https://doi.org/10.1080/00139307309435501

Stull, R. B. (1988). *An Introduction to Boundary Layer Meteorology*.

Tomaz, S., Cui, T., Chen, Y., Sexton, K. G., Roberts, J. M., Warneke, C., et al. (2018). Photochemical Cloud Processing of Primary Wildfire Emissions as a Potential Source of Secondary Organic Aerosol. *Environmental Science and Technology*, *52*(19), 11027–11037. https://doi.org/10.1021/ACS.EST.8B03293/ASSET/IMAGES/LARGE/ES-2018-032933_0004.JPEG

Tsiligiannis, E., Wu, R., Lee, B. H., Salvador, C. M., Priestley, M., Carlsson, P. T. M., et al. (2022). A Four Carbon Organonitrate as a Significant Product of Secondary Isoprene Chemistry. *Geophysical Research Letters*, *49*(11), e2021GL097366. https://doi.org/10.1029/2021GL097366

Vermeuel, M. P., Novak, G. A., Kilgour, D. B., Claflin, M. S., Lerner, B. M., Trowbridge, A. M., et al. (2022). Observations of biogenic volatile organic compounds over a mixed temperate forest during the summer to autumn transition. *Atmospheric Chemistry and Physics Discussions*. https://doi.org/https://doi.org/10.5194/egusphere-2022-1015

Wang, X., Jacob, D. J., Eastham, S. D., Sulprizio, M. P., Zhu, L., Chen, Q., et al. (2019). The role of chlorine in global tropospheric chemistry. *Atmospheric Chemistry and Physics*, *19*(6), 3981–4003. https://doi.org/10.5194/ACP-19-3981-2019

Wolfe, G. M., Cantrell, C., Kim, S., Mauldin, R. L., Karl, T., Harley, P., et al. (2014). Missing peroxy radical sources within a summertime ponderosa pine forest. *Atmospheric Chemistry and Physics*, *14*(9), 4715–4732. https://doi.org/10.5194/acp-14-4715-2014

Yáñez-Serrano, A. M., Nölscher, A. C., Williams, J., Wolff, S., Alves, E., Martins, G. A., et al. (2015). Diel and seasonal changes of biogenic volatile organic compounds within and above an Amazonian rainforest. *Atmospheric Chemistry and Physics*, *15*(6), 3359–3378. https://doi.org/10.5194/acp-15-3359-2015

Yuan, B., Koss, A. R., Warneke, C., Coggon, M., Sekimoto, K., & De Gouw, J. A. (2017). Proton-Transfer-Reaction Mass Spectrometry: Applications in Atmospheric Sciences. *Chemical Reviews*, *117*(21), 13187–13229. https://doi.org/10.1021/ACS.CHEMREV.7B00325/SUPPL_FILE/CR7B00325_SI_001.PDF

Zhou, L., Gierens, R., Sogachev, A., Mogensen, D., Ortega, J., Smith, J. N., et al. (2015). Contribution from biogenic organic compounds to particle growth during the 2010 BEACHON-ROCS campaign in a Colorado temperate needleleaf forest. *Atmospheric Chemistry and Physics*, *15*(15), 8643–8656. https://doi.org/10.5194/acp-15-8643-2015

Journal of Geophysical Research: Atmospheres

Supporting Information for:

Closing the reactive carbon flux budget: Observations from dual mass spectrometers over a coniferous forest

Michael P. Vermeuel[1], Dylan B. Millet[1*], Delphine K. Farmer[2], Matson A. Pothier[2], Michael F. Link[2^], Mj Riches[2], Sara Williams[2], Lauren A. Garofalo[2]

[1] Department of Soil, Water, and Climate, University of Minnesota – Twin Cities, St. Paul, MN, USA

[2] Department of Chemistry, Colorado State University, Fort Collins, CO, USA

[^]now at Engineering Laboratory, National Institute of Standards and Technology, Gaithersburg, MD, USA

[*]Correspondence to D.B. Millet, dbm@umn.edu

Contents of this file

Text S1 to S7

Tables S1 to S5

Figures S1 to S17

Introduction

This document provides information on the following:

S1. Additional field measurement details;

S2. PTRMS laboratory calibrations and signal corrections;

S3. Flux covariance quality control;

S4. Flux spectral corrections;

S5. Modifications to land cover in the GEOS-Chem simulation;

S6. The effect of mountain-valley flow on morning MBO observations; and

S7. The assignment of rate constants to isomers and unknown species.

S1. Field collections

S1.1 Offline VOC speciation

Speciation of select VOCs emitted from ponderosa pine needles and understory species was determined using offline thermal desorption gas chromatography mass spectrometry (GC-MS) performed on sorbent tubes coupled to an online portable photosynthesis system (PPS; LI-6800, LI-COR Biosciences) (Riches et al. 2020) equipped with a 36 cm^2 needle chamber (6800-13, LI-COR Biosciences) and a large light source (6800-03, LI-COR Biosciences). Gas sampling began after plant acclimation to the PPS chamber, determined based on the stabilization of CO_2 assimilation and stomatal conductance. Two handheld pumps simultaneously pulled 4 L of air through subsampling ports up- and downstream of the PPS leaf chamber through passivated sorbent tubes packed with Tenax-TA. Tubes were analyzed offline for identification and quantification of speciated monoterpenes via thermal desorption (UNITY-xr, Markes International) and GC-MS (TRACE 1310 and ISQ, Thermo Scientific).

S1.2 HR-AMS measurements

Submicron non-refractory aerosol mass concentrations were quantified by high-resolution time-of-flight aerosol mass spectrometry (HR-AMS; Aerodyne Research Inc.) (Canagaratna et al., 2015; DeCarlo et al., 2006). The HR-AMS sampled through a ¼" OD copper inlet shared with a scanning mobility sizing spectrometer (SMPS; TSI) with a total 1.1 LPM flow rate. We operated the HR-AMS in V-mode with 5 min time resolution. The sample averaging period included 15 cycles between mass spectrometer (MS) mode (2.5s open/2.5 closed) and particle time-of-flight (PTOF) mode (15s). Organic mass is reported at ambient temperature and pressure with collection efficiency (CE) = 1. We used the ToF-AMS Analysis Toolkits v1.65B (SQUIRREL) and v1.25B (PIKA) (Aerodyne Research Inc.) in Igor Pro (Wavemetrics, Inc) for data processing. The ionization efficiency was calculated by mass comparison of 350 nm size-selected ammonium nitrate particles counted via CPC (TSI, Inc.) Relative ionization efficiencies for ammonium and sulfate were determined with ammonium sulfate and ammonium nitrate. The lower limit of detection (3× the standard deviation of in-field measurements of air collected through a HEPA filter) for OA was 0.11 $\mu g\ m^{-3}$.

S1.3 PTRMS sampling conditions

The PTRMS inlet was teed into a 1.0 m bypass (composed of 1/8" ID PFA tubing) that subsampled from the sampling manifold at 4000 standard cubic centimeters per minute (sccm). Bypass pressure was held at 660 mbar, allowing the instrument drift tube to draw an 80 sccm mass flow, and a supplemental bypass was used to draw an additional 150 sccm through the heated (80°C) 1.5 m, 1/16" ID PFA PTRMS inlet. An inline 47 mm diameter, 5 μm pore-size filter was installed within the sampling bypass, with routine replacements approximately every three days.

S1.4 ICIMS – In-field voltage scanning (dV_{50}) and laboratory calibrations to determine bulk sensitivity

While permeation tubes provided the sensitivity for select organic acids for the I^-CIMS, we determined the sensitivity for other measured ions using voltage scanning. On the evening of 22 August , we systematically changed internal voltage settings within the ion focusing region of the atmospheric pressure interface of the I^-CIMS to create a voltage differential (dV) between the "Q2-Front" and "Skimmer". During the voltage scan, we maintain the voltage differential downstream of the "Skimmer". The resulting decline of analyte signal was then subjected to an optimized sigmoidal fit algorithm to determine the representative dV_{50} value of each analyte ion (dV_{50} = inflection point in sigmoidal curve). The dV_{50} value correlates with the binding strength between I^- and the analyte molecules to form ion-molecule clusters. These dV_{50} values can thus be used to estimate sensitivities of analytes for which there are no standards (Bi et al., 2021; Iyer et al., 2016).

Following the FluCS campaign, we conducted a series of laboratory experiments to quantify the relationship between log(sensitivity) and dV_{50} (**Fig. S5**). We use this relationship to estimate the sensitivities of analyte ions measured in-field using the dV_{50} calculated for each ion. Sensitivities of calibrant compounds were determined in two ways: 1) standard addition experiments using permeation tubes of C_1-C_5 alkanoic acids; and 2) triplicate liquid injections using a Filter Inlet for Gases and AEROsols (FIGAERO) of tropic ($C_9H_{10}O_3$), myristic ($C_{14}H_{28}O_2$), and palmitic ($C_{16}H_{32}O_2$) organic acids (Lopez-Hilfiker et al., 2014). We determine the dV_{50} values of the above eight calibrants in an identical manner as the in-field voltage scanning experiments.

For determination of I^-CIMS sensitivities in the field, species that could not be fit via voltage scanning experiments or had dV_{50} values lower than 2 V and higher than 9 V were assigned the median sensitivity value of 4.9 ncps ppt^{-1}. Species that had sensitivities higher than the collision-limit sensitivities as determined for this instrument (50 ncps ppt^{-1}) were assigned the collision-limit sensitivity (Mattila et al., 2020).

S2. Laboratory calibrations and data corrections

S2.1 Liquid calibrations

Liquid calibrations were performed for MT isomers ($C_{10}H_{16}$: α-pinene, β-pinene, limonene, ocimene), monoterpenoids ($C_{10}H_{16}O$: camphor, α-pinene oxide; $C_{10}H_{14}O$: carvone, myrtenal, perillaldehyde, verbenone) and a sesquiterpene oxide (caryophyllene oxide: $C_{15}H_{24}O$). All liquid standards were obtained from Sigma Aldrich. Species were detected within the PTRMS as the protonated parent ion, except α-pinene oxide which was detected as $C_{10}H_{17}O^+$ and $C_{10}H_{15}^+$. Liquid standards were diluted in cyclohexane and delivered via a syringe pump. 5 SLPM of zero air flowing orthogonally to the syringe passed over the needle and aspirated the calibrant droplet. The PTRMS measurement line (~0.5 m length, 1/8" ID, 80 ^{o}C) was configured to minimize residence times and VOC partitioning to inlet walls. The zero air flow was held constant while the syringe pump speed was varied to produce a calibration curve for each species. Sensitivities were obtained as a function of humidity across the range of field-measured $H_2O{\cdot}H_3O^+$:H_3O^+ ratios (where H_3O^+ ~ 500 × $H_3{}^{18}O^+$). All humidity-dependent sensitivities were calculated relative to β-pinene, a species calibrated in the field, enabling dynamic calibration corrections based on field conditions. **Figure S2** shows the range of measured sensitivities for monoterpenes, while **Figure S3** summarizes the sensitivities for all calibrated species for a typical humidity level.

S2.2 Formaldehyde calibrations and signal corrections for formulae containing multiple species

Formaldehyde calibrations were performed following the field study by diluting a 4958 ppb standard (certified 19 September 2022) into across relevant humidity (i.e., $H_2O{\cdot}H_3O^+$:H_3O^+) levels. The low ambient water vapor concentrations in this semi-arid ecosystem enabled reliable formaldehyde detection at CH_3O^+. The associated humidity dependence led to a 2-fold sensitivity decrease across the encountered water vapor concentrations (**Fig. S4a**), and this dependence was accounted for during calibration.

Prior work has shown that other VOCs (namely methanol and methyl hydroperoxide; Inomata et al., 2008) can fragment to also produce CH_3O^+ ions. Analysis of our VOC cylinders and liquid standards (**Table S1**) indeed revealed a CH_3O^+ interference from methanol (~0.2:1 CH_3O^+:CH_5O^+) and, weakly, from limonene (~0.05:1 CH_3O^+: $C_{10}H_{17}^+$). Since the raw MT signal at $C_{10}H_{17}^+$ (along with that for methyl hydroperoxide at $CH_5O_2^+$) was very low compared to CH_5O^+, only the methanol correction was applied here.

In general, interference corrections for calibrated species proceeded as described below for formaldehyde:

1. The CH_3O^+ signal including both the analyte of interest (formaldehyde) and a fragment species (methanol), was calibrated for the fragment species (methanol).
2. The concentration difference between the fragment mass (CH_3O^+) and the parent mass for the same species (CH_5O^+) was then calculated to obtain a residual concentration.
3. That residual concentration was converted back to signal units based on the methanol sensitivity.
4. The residual signal was then calibrated for formaldehyde.

The corrected formaldehyde timeseries exhibits a different diel cycle and concentration range than the uncorrected version (**Fig. S4b**). Removal of the fluctuating methanol signal also changed the inferred net formaldehyde flux from primarily upward to bidirectional (**Fig. S4c**). The above procedure was similarly performed for isoprene to correct for $C_5H_9^+$ interference from 232-MBO. The α-pinene oxide contribution to $C_{10}H_{17}O^+$ was likewise removed by attributing the entire $C_{10}H_{15}^+$ signal to that species.

S3 Flux quality control

In addition to the QA/QC described in the main text, flux data were filtered for wind shear and stationarity. Flux periods were discarded if either of the following conditions were met:

1. friction velocity (u_*) < 0.15 m s^{-1}, where

$$u_* = \left(\overline{w'u'}^2 + \overline{w'v'}^2\right)^{\frac{1}{4}} \tag{E1}$$

2. the mean flux for five encompassed sub-periods differed from that for the entire 30-minute window by more than 30% (i.e. stationarity test) (Foken & Wichura, 1996):

$$1-\frac{\overline{\overline{w'C'}}_{sub-period}}{\overline{w'C'}_{full\,period}}>0.3 \quad \text{(E2)}$$

S4 Spectral corrections

Flux attenuation due to inlet damping, instrument response, and sensor separation was calculated from an empirical model (Horst, 1997) that employs an attenuation time constant, τ_c, also known as the response time. A correction factor is then calculated as:

$$\frac{F_m}{F}=\frac{1}{1+(2\pi n_m \tau_c U/z)^{\alpha}} \quad \text{(E3)}$$

where F_m/F is the ratio of the measured to the unattenuated flux, U is wind speed, z is measurement height, and n_m and α are scaling factors for an unstable boundary layer (taken as 0.085 and 7/8, respectively). The response time can be determined empirically from the ratio of the attenuated scalar normalized cospectra to the unattenuated *w'T'* cospectra and is calculated as the frequency where the attenuated signal is reduced by $1/\sqrt{2}$. For the PTRMS species ΣMT and 232-MBO the resulting τ_c ~ 1 s, requiring a 6% flux correction at the campaign-mean daytime windspeed of 2.1 m s^{-1}, while for ΣSQT and MTO τ_c ~ 5 s, requiring a 25% correction. For the ICIMS species HCOOH τ_c ~ 0.4 s (2.7% correction).

S5 GEOS-Chem land cover updates

The 0.25° × 0.3125° model grid cell containing the MEFO site has heterogenous land cover made up of 6 Community Land Model (CLM) classifications, with 48% of the surface designated as crop cover or bare ground. This is not representative of the 1 x 1 km^2 measurement footprint which primarily consists of ponderosa pine, grass, and shrubs (**Fig S10**). We therefore modified the model land cover and leaf area to simulate biosphere-atmosphere exchange more accurately.

Updates employed Landsat imagery from the United States Geological Survey (USGS) EarthExplorer tool (https://earthexplorer.usgs.gov/). Imagery was obtained encompassing the site and the surrounding land area (300 m in the prevailing wind directions) to capture the highest density portions of the flux footprint. This imagery then underwent k-means clustering-based image segmentation as part of the MATLAB Statistics and Machine Learning Toolbox, with pixels separated into three clusters representing "tree crowns", "tree base and shadows", and grass". The corresponding pixel fractions then yielded a ponderosa pine fraction of 0.7 and a grass fraction of 0.3, the latter of which we treat in the model as C3 non-arctic grass.

A model LAI of 2.36 m^2 m^{-2} was then obtained by assuming a standard LAI of 3 m^2 m^{-2} for needleleaf evergreen temperate trees (as applied for a MEGAN v2.1 analysis at the same site; Kaser et al., 2013a) and 1 m^2 m^{-2} for grass (a median estimate for temperate 15-25 cm grasses; Byrne et al., 2005). The resulting value is higher than the MODIS-derived ecosystem average (1.4 m^2 m^{-2}) as well as previous estimates for the entire Manitou Experimental Forest (1.2 m^2 m^{-2}; Berkelhammer et al., 2016) but was found to be more appropriate for our site based on a comparisons of our leaf- and canopy-level flux observations.

Basal VOC emissions were obtained by combining MEGAN v3.2 leaf area emission factors (mg compound m^{-2} leaf hr^{-1}) with the fractional ponderosa pine and C3 non-arctic grass coverage scaled by species-specific LAI. The site LAI of 2.36 m^2 m^{-2} was used in the Parameterized Canopy Environment Emission Activity (PCEEA) algorithms (Guenther et al., 2006). The site LAI was also used in the model dry deposition routines with the Olson et al. (2001) “dry evergreen woods” land cover classification.

S6 The effect of mountain-valley flow on morning 232-MBO observations

A mountain-valley flow pattern causes a nighttime south-to-north drainage flow of cold, dense air from higher elevations that leads to stratification at the MEFO site and suppresses vertical mixing. During the day, high-pressure conditions lead to upslope flow from the north, destratification, dynamic instability, and turbulent vertical mixing. The morning transition from mountain- to valley-flow features a unique set of environmental conditions that creates the early flux peak seen in **Fig. 2**. Chemical species with light-dependent leaf-level emissions (e.g., 232-MBO and some MT isomers) are emitted in the pre-transition daylight hours but not yet vertically mixed, so that concentrations build up near the surface. During the subsequent transition, the developing vertical mixing coupled to a large concentration gradient causes a large but short-lived upward flux as the canopy vents. This is illustrated in **Fig. S12**, where the turbulent vertical mixing strength is approximated as the standard deviation in vertical wind (σ_w), and the short-term 232-MBO flux enhancements are seen to coincide with low but increasing σ_w. This behavior was not reported previously by Kaser et al. (2013a) based on long term 232-MBO flux measurements at this site, which could be due to their use of strict shear stress filters that removed this period of low σ_w and low u_* (~ 0.1-0.15 m/s). Karl et al. (2014) reported a morning build up in 232-MBO concentrations but not flux during a week-long study at this site; the difference could reflect their limited study timeframe or more strict flux filtering.

S7 Rate constant assignments for MT, SQT, and species with unknown k_{O3}

For ΣMT we applied the α-pinene rate coefficents (k_{OH} = 5.2 x 10^{-11} cm^3 $molecules^{-1}$ s^{-1} and k_{O3} = 8.7 x 10^{-17} cm^3 $molecule^{-1}$ s^{-1} at 298 K) (Atkinson et al., 1990; Atkinson & Arey, 2003) since those were the median values across observed MT. For ΣSQT we employed a k_{OH} that represents the average across five isomers (α-cedrene; α-copaene; β-caryophyllene; α-humulene; longifolene; 1.4 x 10^{-10} cm^3 $molecules^{-1}$ s^{-1} at 298 K) (Atkinson & Arey, 2003) and the β-caryophyllene k_{O3} value (1.1 x 10^{-14} cm^3 $molecule^{-1}$ s^{-1} at 298 K) (Richters et al., 2015). Understory measurements during our study pointed to important contributions from β-farnesene, sesquisabinene, and β-sesquiphellandrene, of which only β-farnesene has a published ozone rate coefficient (7 x 10^{-16} cm^3 $molecule^{-1}$ s^{-1} at 298 K) (Kim et al., 2011). Since the other two quantified SQTs contain rings and endo- and exocylic double bonds we assume the collective rate constant is closer to that for β-caryophyllene (1.1 x 10^{-14} cm^3 $molecule^{-1}$ s^{-1} at 298 K). Furthermore, prior GC measurements at this site found β-caryophyllene to be the largest contributor to ambient ΣSQT concentrations (Chan et al., 2016), while other leaf level measurements for ponderosa pine have identified β-caryophyllene as a contributing isomer (Helmig et al., 2017). For consistency, the same ΣMT and ΣSQT rate coefficients were applied to both observations and model.

Molecules with known formulae but unknown rate coefficients for reaction with ozone were assigned k_{O3} values based on their DBE, with k_{O3} = 0, 8.6 × 10^{-18}, 8.1 × 10^{-17}, and 1.5 × 10^{-16} cm^3 $molecule^{-1}$ s^{-1} for DBE = 0, 1, 2, and ≥3. These values were obtained as the median in each case across observed species with known k_{O3}.

We estimate the uncertainties in k_{OH} and k_{O3} for unknown species at a factor of 10 by applying the same methodology to all measured species with known structure and k_{Y+VOC}. The resulting upper limits for each unknown VOC are capped at k_{OH} = 1.39 × 10^{-10} (the value for ΣSQT) and k_{O3} = 1.9 × 10^{-6} (the value for butene).

Supplementary Tables

Species name	Formula	Concentration (ppb)
Acetaldehyde	CH_3CHO	1028
Methanol	CH_3OH	4969
Acetonitrile	CH_3CN	1008
Acetone	CH_3COCH_3	2439
Isoprene	C_5H_8	2477
Methyl ethyl ketone	C_4H_8O	1049
Hydroxyacetone	$C_3H_6O_2$	1280
Benzene	C_6H_6	1047
Toluene	C_7H_8	1042
m-Xylene	C_8H_{10}	1018
1,3,5-Trimethylbenzene	C_9H_{12}	950
1,2,4,5-Tetramethylbenzene	$C_{10}H_{14}$	990
Propene	C_3H_6	1001
Furan	C_4H_4O	1037
DMS	C_2H_6S	1065
Methacrolein	C_4H_6O	1047
2-Methyl-3-Buten-2-ol	$C_5H_{10}O$	1040
3-Hexanone	$C_6H_{12}O$	1003
β-pinene	$C_{10}H_{16}$	1009
Propyne	C_3H_4	970
1-Butene	C_4H_8	982
Ethanol	C_2H_6O	1032
Methyl Vinyl Ketone	C_4H_6O	979
3-Methyl Furan	C_5H_6O	973
3-Pentanone	$C_5H_{10}O$	1025
Ethyl Benzene	C_8H_{10}	991
α-pinene	$C_{10}H_{16}$	997

Table S1: Species and concentrations contained in VOC cylinders used for in-field PTRMS calibration. All species certified 5 November 2021 with an uncertainty of +/- 5%.

Reaction[a]	***k*** **(cm^3 molecule^{-1} s^{-1})**[b]
MBO + OH → 0.52ACET + 0.35CH_2O + 0.50ACTA	8.1×10^{-12}*exp(610/*T*)
MBO + NO_3 → 0.68ACET + 0.13ITHN	4.6×10^{-14}*exp(-400/*T*)
MBO + O_3 → 0.08ACET + 0.47CH_2O	1.0×10^{-17}
RCOOH + OH → OTHRO2	1.2×10^{-12}
SESQ + OH → KO_2 + products	1.97×10^{-10}
SESQ + O_3 → KO_2 + OH + products	1.2×10^{-14}
SESQ + NO_3 → INDIOL	1.90×10^{-11}

Table S2: Additions to the GEOS-Chem chemical mechanism.
[a] molar yields for MBO reactions taken from Fantechi et al. (1998) and Ferronato et al. (1998)
[b]all rate constants taken from MCM v3.3.1 (Saunders et al., 2003)

Species	***H**** **(M atm^{-1})**	***f_0***
RCOOH	5×10^{-3}	1

Table S3: Additions to the GEOS-Chem dry deposition scheme. Henry's law constants are taken from Sander (2015) and reactivity factors for oxygenated VOCs are set to 1 following Karl et. al (2010)

	Upward VOC-Carbon	Downward VOC-Carbon	Upward OH Reactivity	Downward OH Reactivity	Upward O_3 Reactivity	Downward O_3 Reactivity
1.	$C_5H_{10}O$	$C_3H_6O_2$	$C_5H_{10}O$	CH_2O	$C_{15}H_{24}$	CHON
2.	$C_{10}H_{16}$	CH_2O	$C_{10}H_{16}$	*$C_5H_{10}O_3$*	$C_{10}H_{16}$	*$C_3H_3O_3$*
3.	C_2H_6O	*$C_5H_{10}O_3$*	C_5H_8	$C_3H_6O_2$	$C_5H_{10}O$	*$C_4H_6O_3$*
4.	CH_4O	*$C_4H_8O_3$*	$C_{15}H_{24}$	*$C_4H_6O_3$*	C_4H_8	*$C_4H_6O_4$*
5.	C_5H_8	*$C_4H_6O_3$*	C_2H_4O	*$C_5H_9NO_4$*	C_5H_8	*$C_3H_4O_3$*
6.	$C_3H_6O_2$	*$C_5H_9NO_4$*	CH_2O	*$C_3H_3O_3$*	C_3H_4O	*$C_4H_4O_3$*
7.	$C_{15}H_{24}$	*$C_3H_3O_3$*	C_2H_6O	*$C_4H_6O_4$*	C_6H_6	*$C_5H_9NO_4$*
8.	C_3H_6O	$C_2H_4O_2$	$C_3H_6O_2$	*$C_5H_9NO_5$*	C_5H_6O	*$C_4H_7NO_5$*
9.	C_2H_4O	*$C_3H_6O_3$*	$C_4H_8O_2$	*$C_3H_6O_3$*	C_4H_4	*$C_2H_3NO_2$*
10.	CH_2O	*$C_4H_6O_4$*	C_4H_6O	*$C_4H_7NO_5$*	C_8H_8	*$C_5H_9NO_5$*

Table S4: Top ten contributors to the observed upward and downward fluxes. Species detected with the ICIMS are in *italics*; others were detected by PTRMS. PTRMS compounds were detected as protonated species (MH^+) and ICIMS species were detected as iodide adducts (IM^-)

Species	Formula	Full name
ACET	C_3H_6O	Acetone
ACTA	$C_2H_4O_2$	Acetic acid
ALD2	CH_3CHO	Acetaldehyde
C2H6	C_2H_6	Ethane
CH2O	CH_2O	Formaldehyde
EOH	C_2H_6O	Ethanol
GLYC	$C_2H_4O_2$	Glycoaldehyde
HCOOH	HCOOH	Formic acid
HMHP	CH_4O_3	Hydroxymethyl hydroperoxide
HMML	$C_4H_6O_3$	hydroxymethyl-methyl-a-lactone
ICHE	$C_5H_8O_3$	Isoprene hydroxy-carbonyl-epoxides
IDHDP	$C_5H_{12}O_6$	Isoprene dihydroxy dihydroperoxide
IDN	$C_5H_8N_2O_6$	Lumped isoprene dinitrates
IEPOX	$C_5H_{10}O_3$	Isoprene epoxide
IEPOXA	$C_4H_{10}O_3$	trans-Beta isoprene epoxydiol
IEPOXB	$C_4H_{10}O_3$	cis-Beta isoprene epoxydiol
ISOP	C_5H_8	Isoprene
ISOPNB	$C_5H_9NO_4$	Isoprene nitrate Beta
ISOPND	$C_5H_9NO_4$	Isoprene nitrate Delta
ITHN	$C_5H_{11}NO_7$	Lumped isoprene tetrafunctional hydroxynitrates
INDIOL	--	Generic aerosol-phase organonitrate hydrolysis product
KO_2	$C_4H_5O_3$	Peroxy radical from >3 ketones
MACR	C_4H_6O	Methacrolein
MAP	$C_2H_4O_3$	Peroxyacetic acid
MBOX	$C_5H_{10}O$	2-methyl-3-buten-2-ol
MOH	CH_3OH	Methanol
MONITS	$C_{10}H_{17}NO_4$	Saturated 1st gen monoterpene organic nitrate
MP	CH_3OOH	Methyl hydro peroxide
MTPA	$C_{10}H_{16}$	α-pinene, β-pinene, sabinene, carene
MVK	C_4H_6O	Methyl vinyl ketone
MVKPC	$C_4H_6O_4$	MVK hydroperoxy-carbonyl
OTHRO2	$C_2H_5O_2$	Other C2 RO_2 not from C_2H_6 oxidation
PAN	$C_2H_3NO_5$	Peroxyacetyl nitrate
PIP	$C_{10}H_{18}O_3$	Peroxide from MTPA
PPN	$C_3H_5NO_5$	Lumped peroxypropionyl nitrate
RCOOH	$C_3H_6O_2$	>C2 organic acids
SQT	$C_{15}H_{24}$	Sesquiterpenes
TSOG	--	Lumped semivolatile gas products of monoterpene + sesquiterpene oxidation
XYLE	C_8H_{10}	Xylene

Table S5: GEOS-Chem species names and formulae used in this analysis.

Supplementary Figures

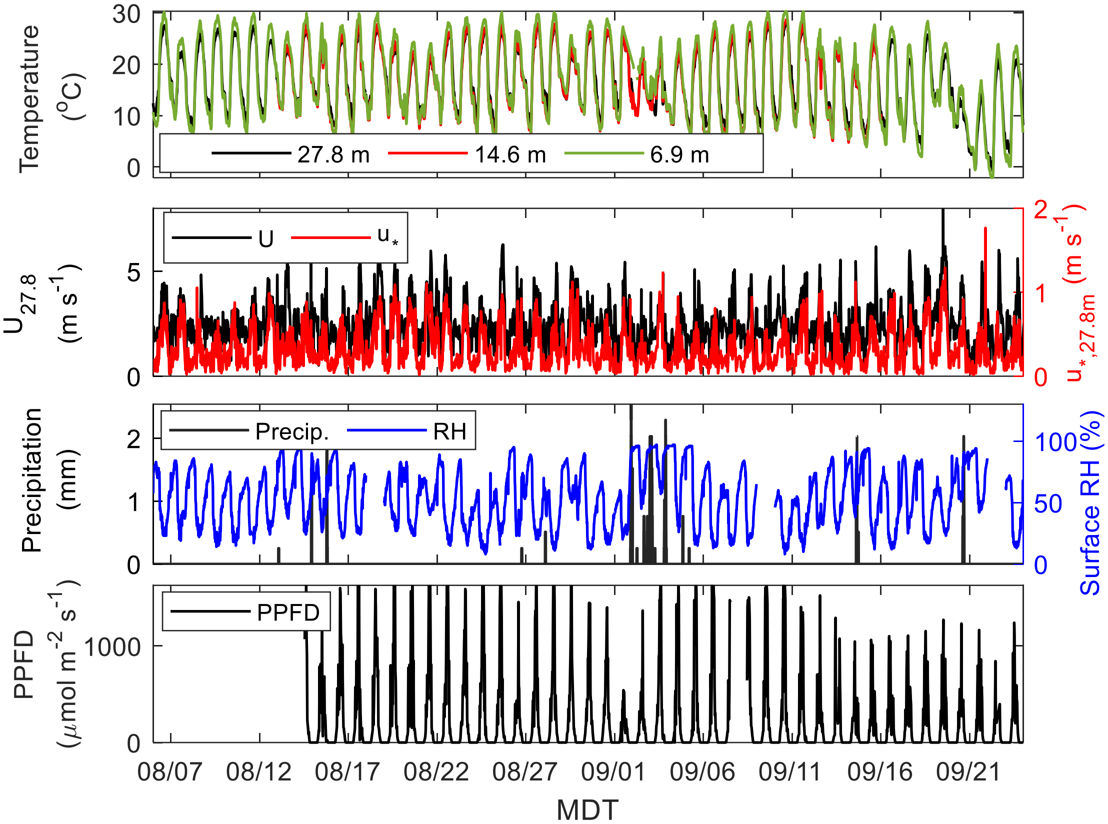

Figure S1: Meteorology during the FluCS 2021 study: a) sonic temperature at three heights, b) horizontal wind (U) and friction velocity (u_*) at 27.8 m, c) precipitation and relative humidity, d) surface photosynthetically active radiation (PAR).

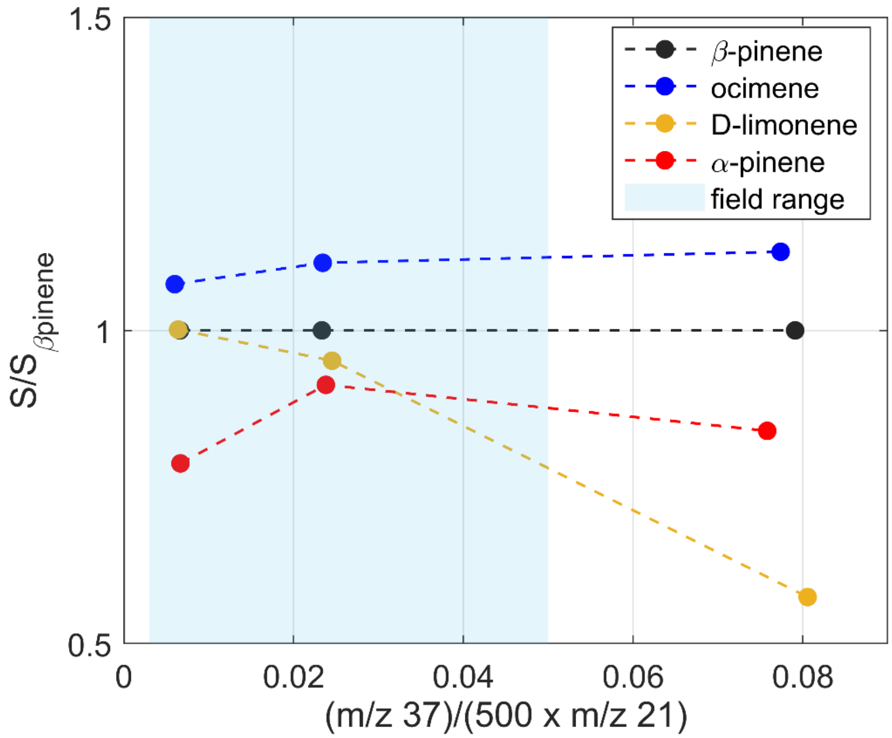

Figure S2: Sensitivities (S) for monoterpenes observed at MEFO relative to β-pinene (circles) over a range of PTRMS water concentrations. Water concentrations are calculated as the ratio of the protonated water dimer (m/z 37; $H_2OH_3O^+$) to the protonated water isotope scaled by abundance (500 × m/z 21; $H_3{}^{18}O^+$). Also indicated is the range of water concentration encountered during FluCS 2021 (blue shaded region).

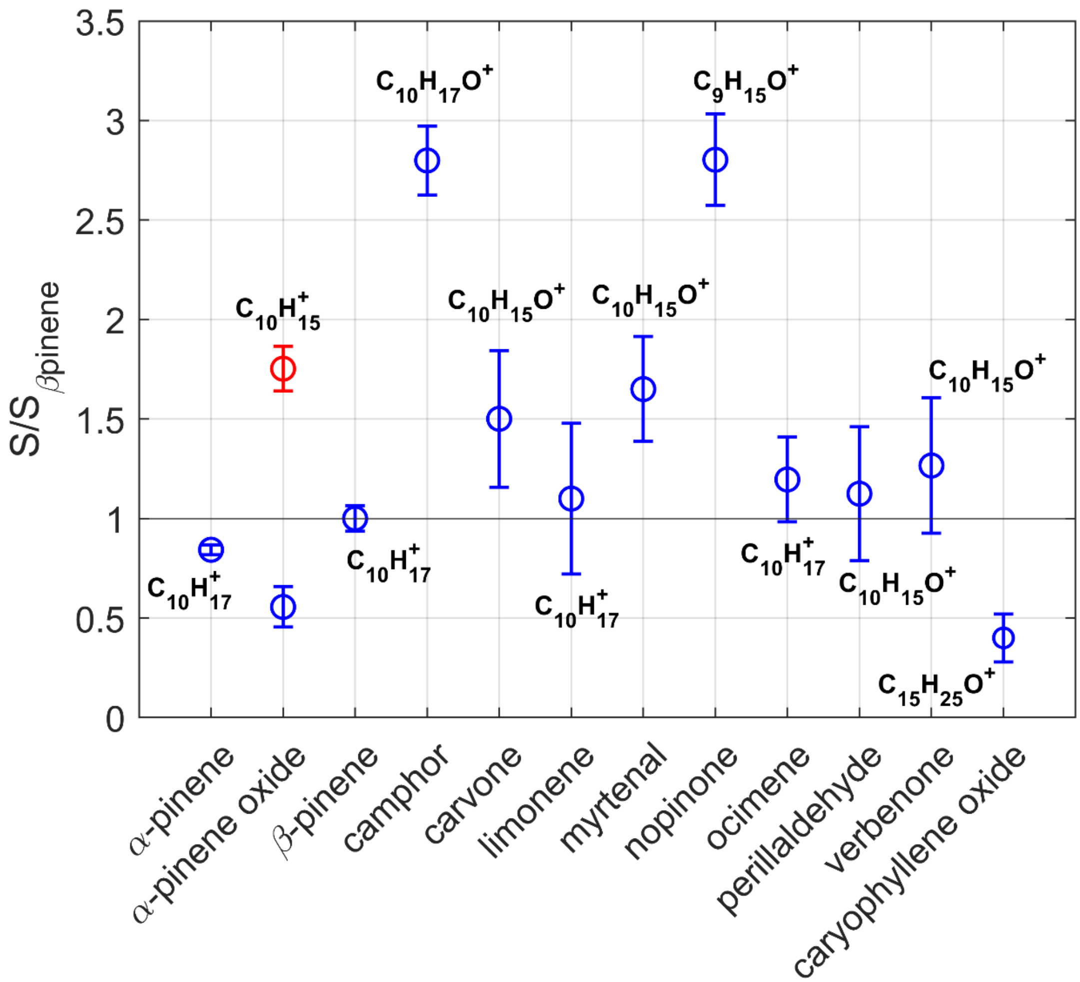

Figure S3: Example compound sensitivities (S) relative to that for β-pinene ($S_{\beta\text{-pinene}}$) measured in-laboratory via liquid calibration. All sensitivities are plotted for the median water concentration for the study. All masses were calibrated at the parent ion (blue circles), except α-pinene oxide (red circle) which was calibrated at both the parent ion and fragment.

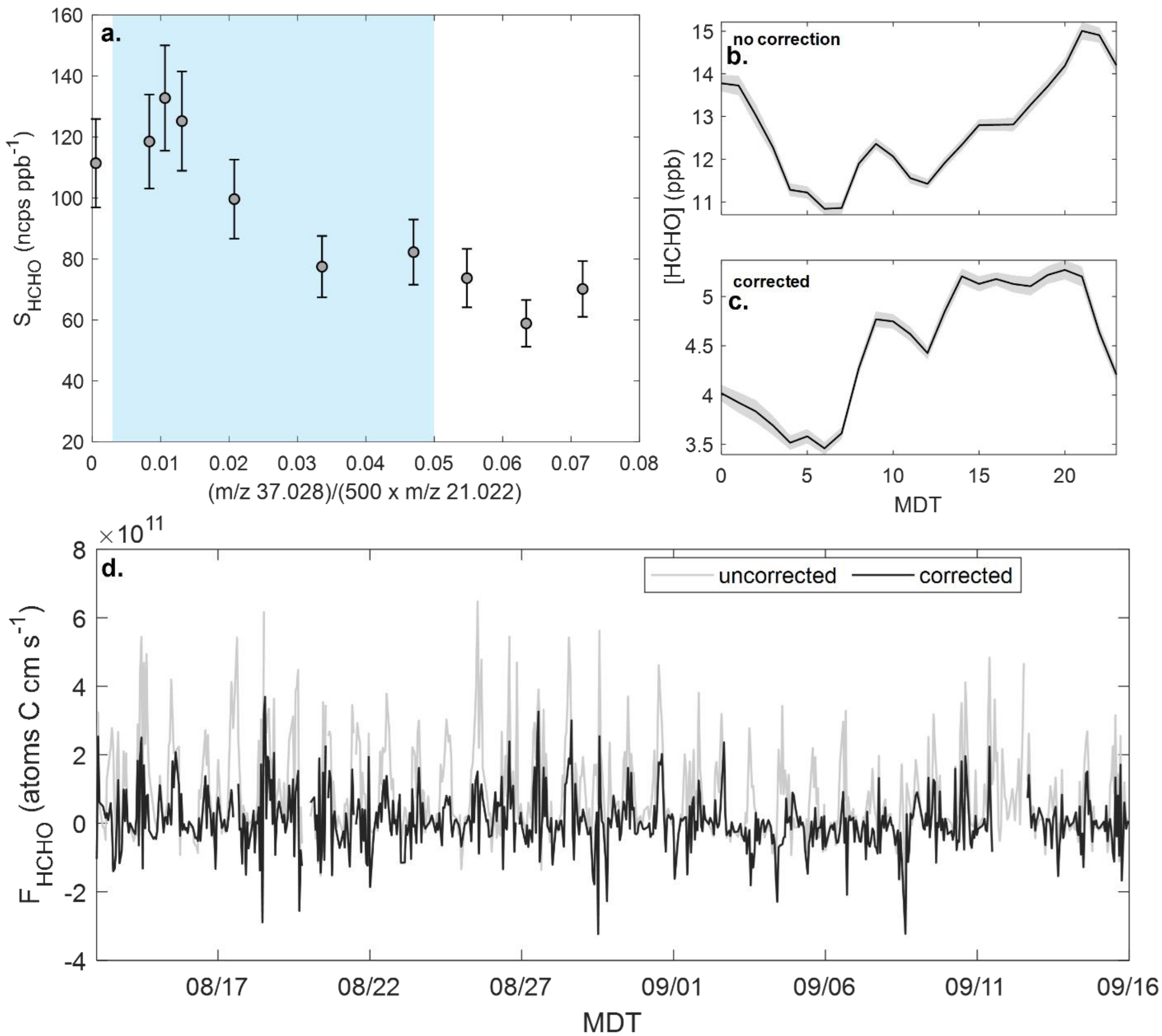

Figure S4: Summary of HCHO calibration and correction results. a) Humidity dependence of the HCHO sensitivity (S_{HCHO}) under different water concentrations. Calibrated HCHO concentrations (b) without correcting for the methanol interference, and (c) after correction. (d) Calibrated HCHO flux before and after methanol correction.

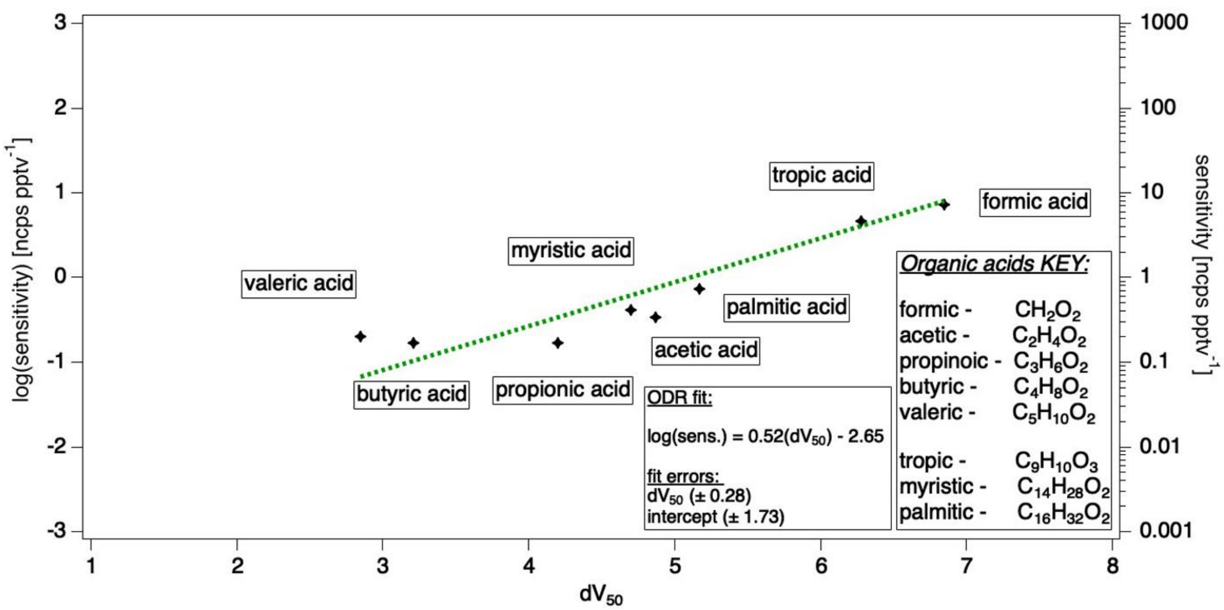

Figure S5: Log-linear dependence of ICIMS sensitivity on dV_{50}. The inset ODR fit was used for calculating ICIMS sensitivity.

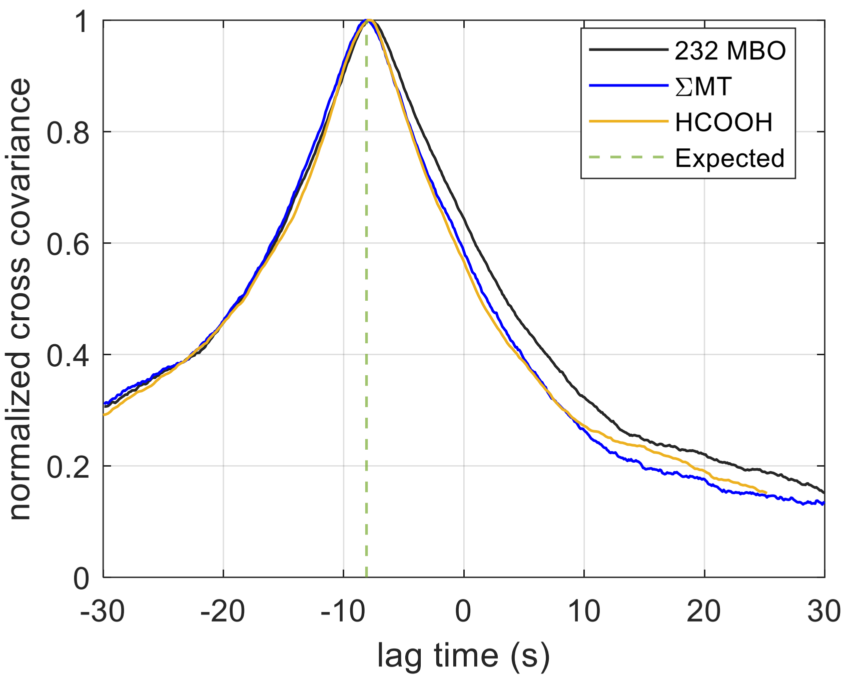

Figure S6: Normalized daytime averaged cross-covariance for 232-MBO and ΣMT (measured by PTRMS) and HCOOH (measured by ICIMS). The dashed line indicates the expected lag time based on the calculated air residence within the flux sampling inlet.

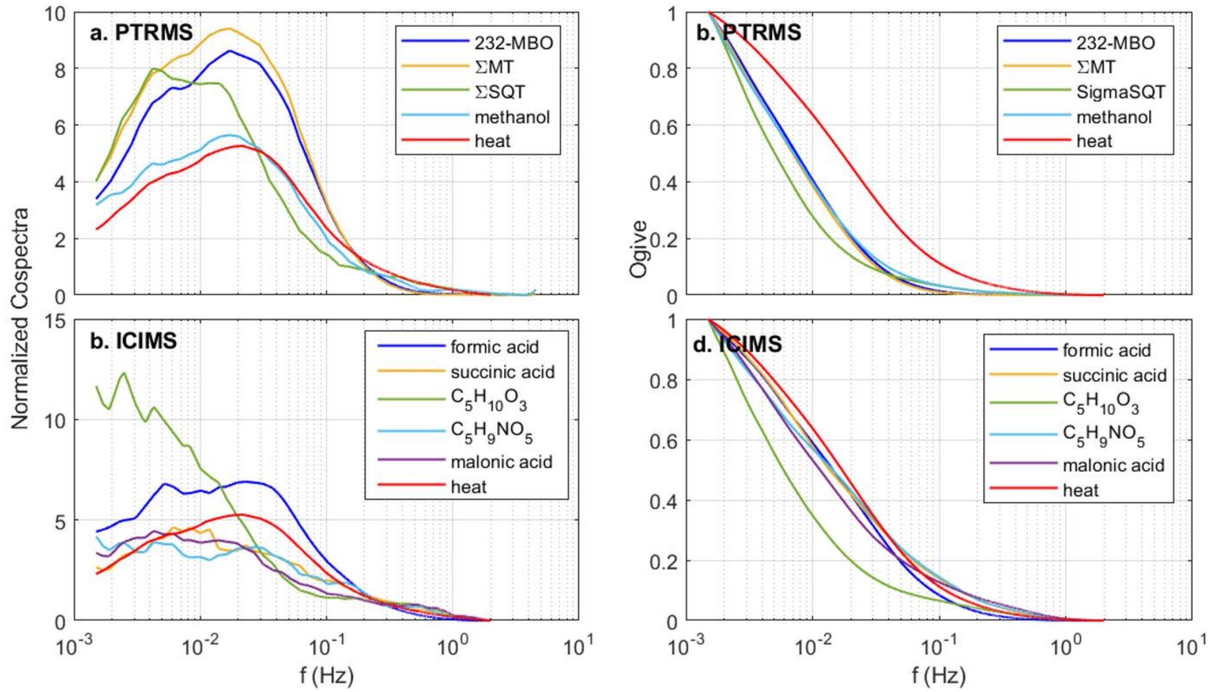

Figure S7: Frequency-normalized cospectra and ogives for high-signal species measured by PTRMS (a + b) and ICIMS (c + d). Cospectra and ogives for the unattenuated sensible heat flux (red lines) are included for reference.

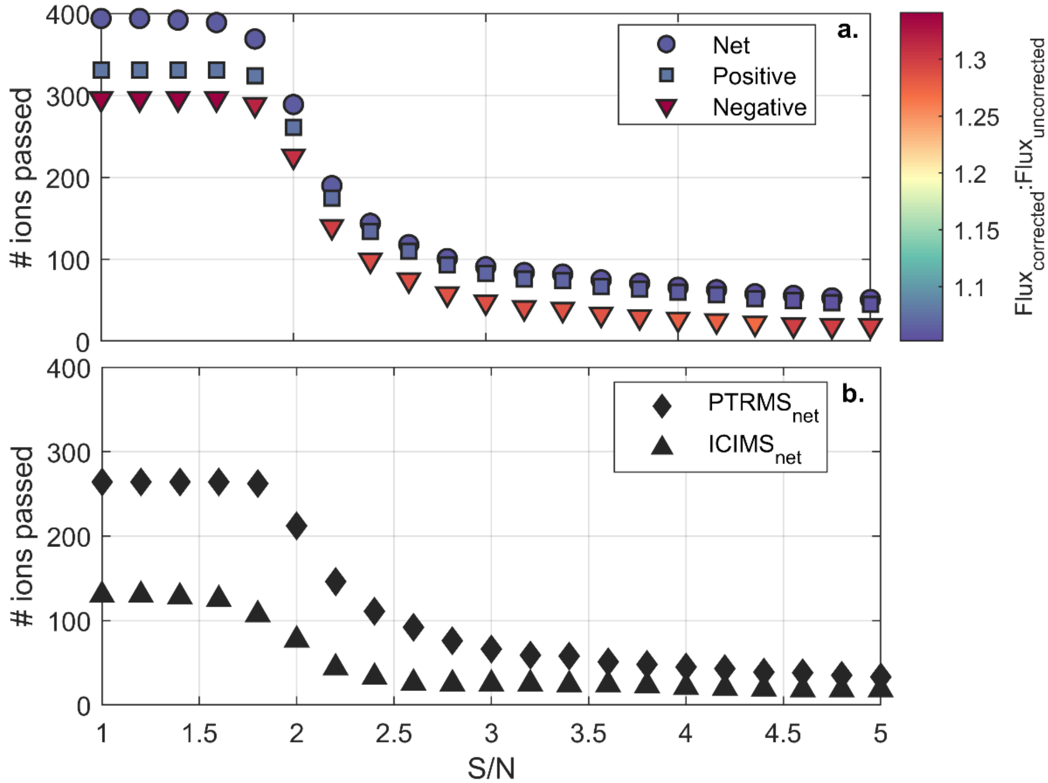

Figure S8: Ion filters based on signal to noise (S/N) evaluation. a) The number of ions with corresponding S/N values for the net, upward, and downward VOC-C fluxes. b) The number of ions with corresponding S/N values for the net PTRMS ICIMS fluxes. The weighted spectral correction factor relative to the uncorrected flux is indicated by the colorbar.

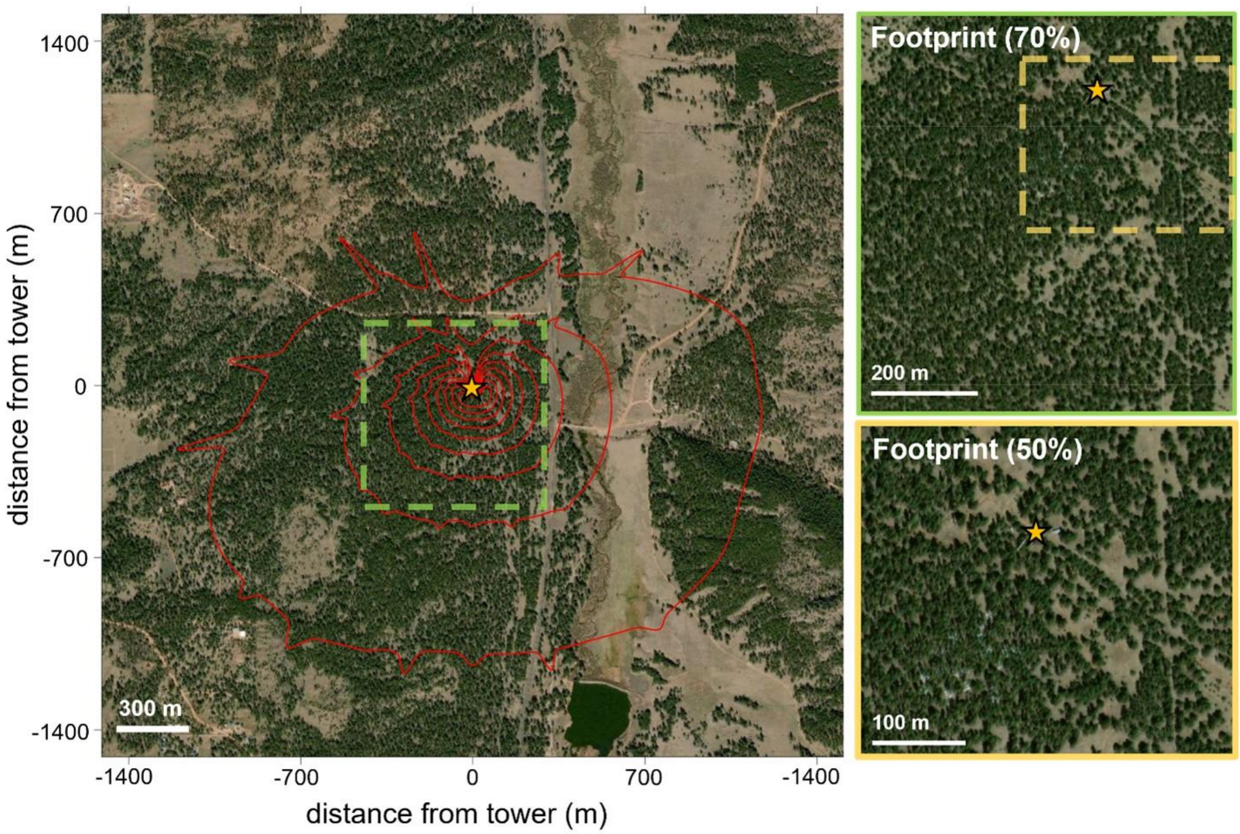

Figure S9: Daytime flux footprint contours (up to 80%) overlaid on geostationary imagery. Included are enhanced images within the 80% and 50% contours, the latter of which contains the highest sampling probability and is used for calculating in-footprint plant functional type contributions.

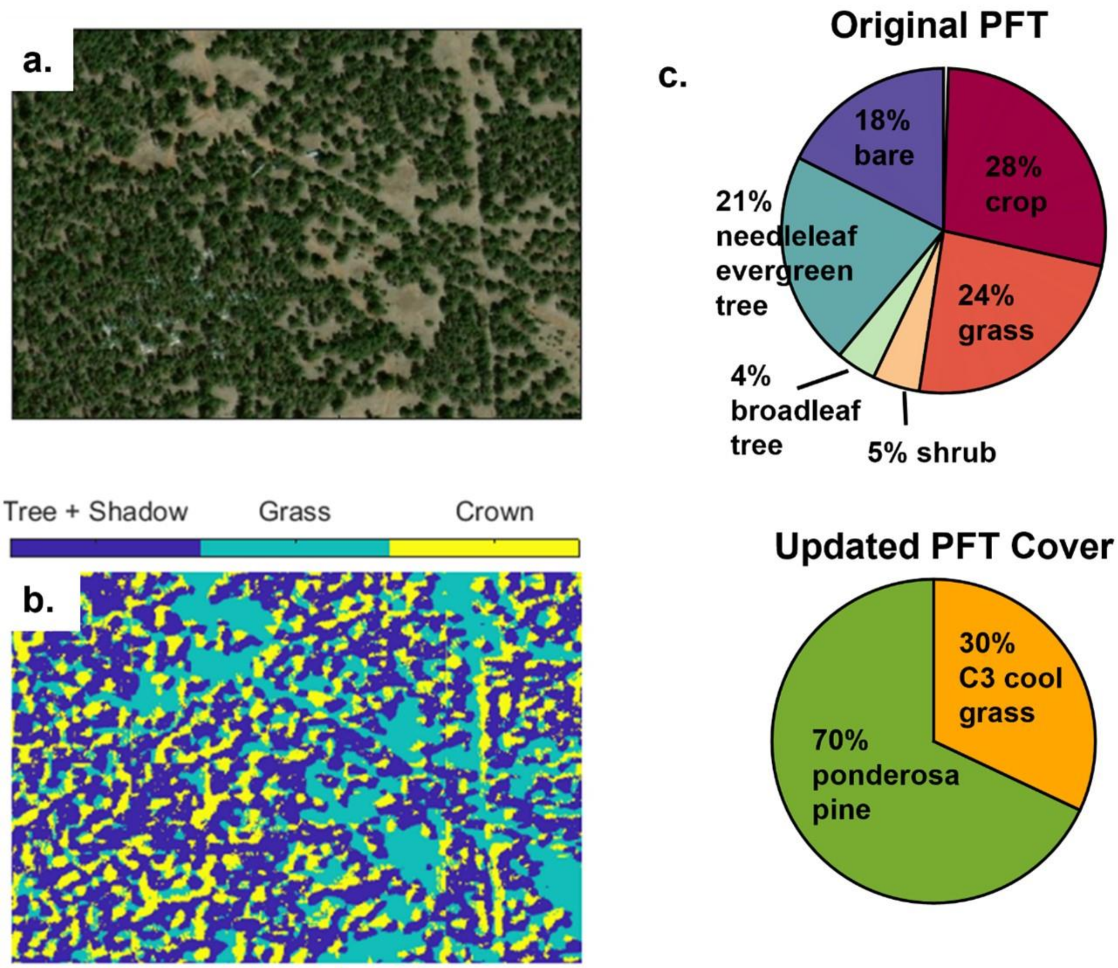

Figure S10: Calculation of plant functional type (PFT) contributions from geostationary imagery. Land cover imagery within the 50% flux footprint (a) undergoes k-means clustering (b) to separate pixels into three groups: “tree and shadow” (dark blue), “grass” (teal), and “tree crown” (yellow). The clusters are separated into ponderosa pine and C3 grass, and the results (c) used to update the default GEOS-Chem land cover within the corresponding model grid cell.

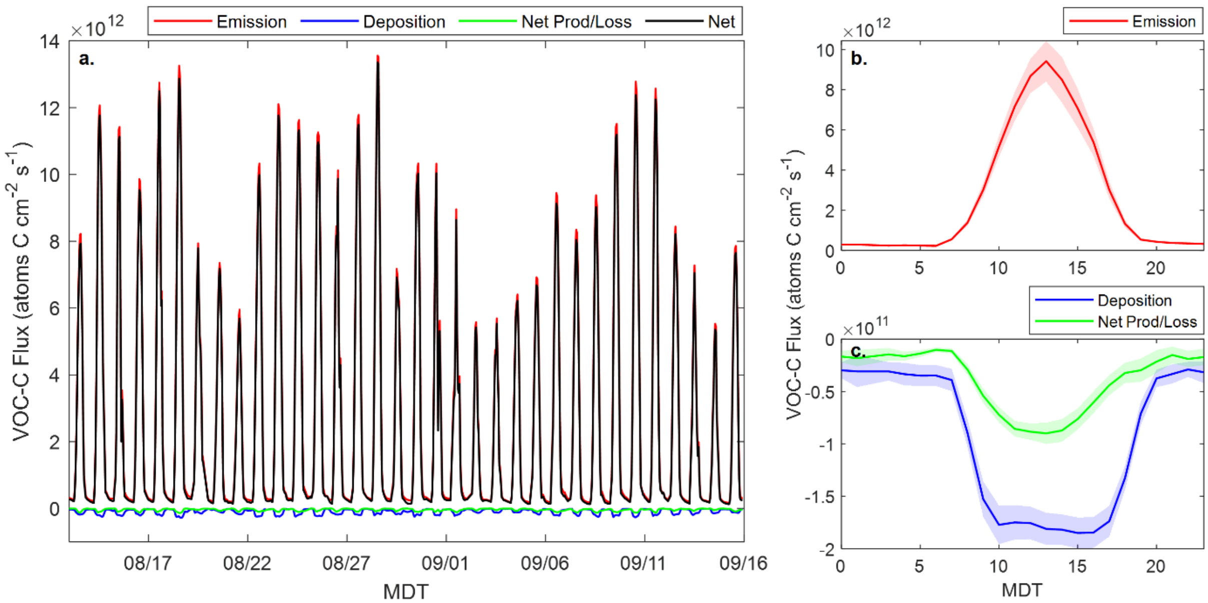

Figure S11: a) Model-simulated fluxes due to emissions (red), deposition (blue), and chemistry (green) along with the resulting net flux (black). The corresponding diel profiles (b, c) show that the GEOS-Chem emission fluxes are ~50× larger than the downward fluxes, while deposition and chemistry are closer in magnitude.

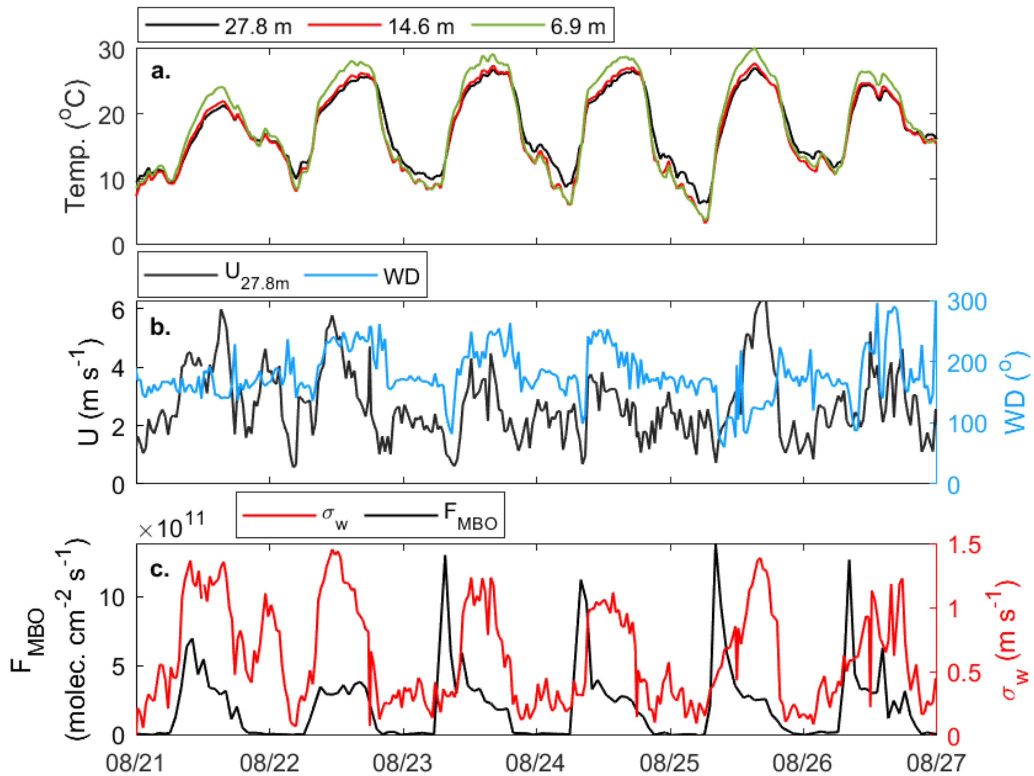

Figure S12: Example timeseries showing the coupling between low but developing morning-time vertical mixing and 232-MBO flux enhancements. A changing temperature gradient (a) is accompanied by a drop in windspeed and shifting wind direction (b). The same transition period also witnesses changes in the standard deviation of vertical wind (σ_w) and enhanced 232-MBO flux.

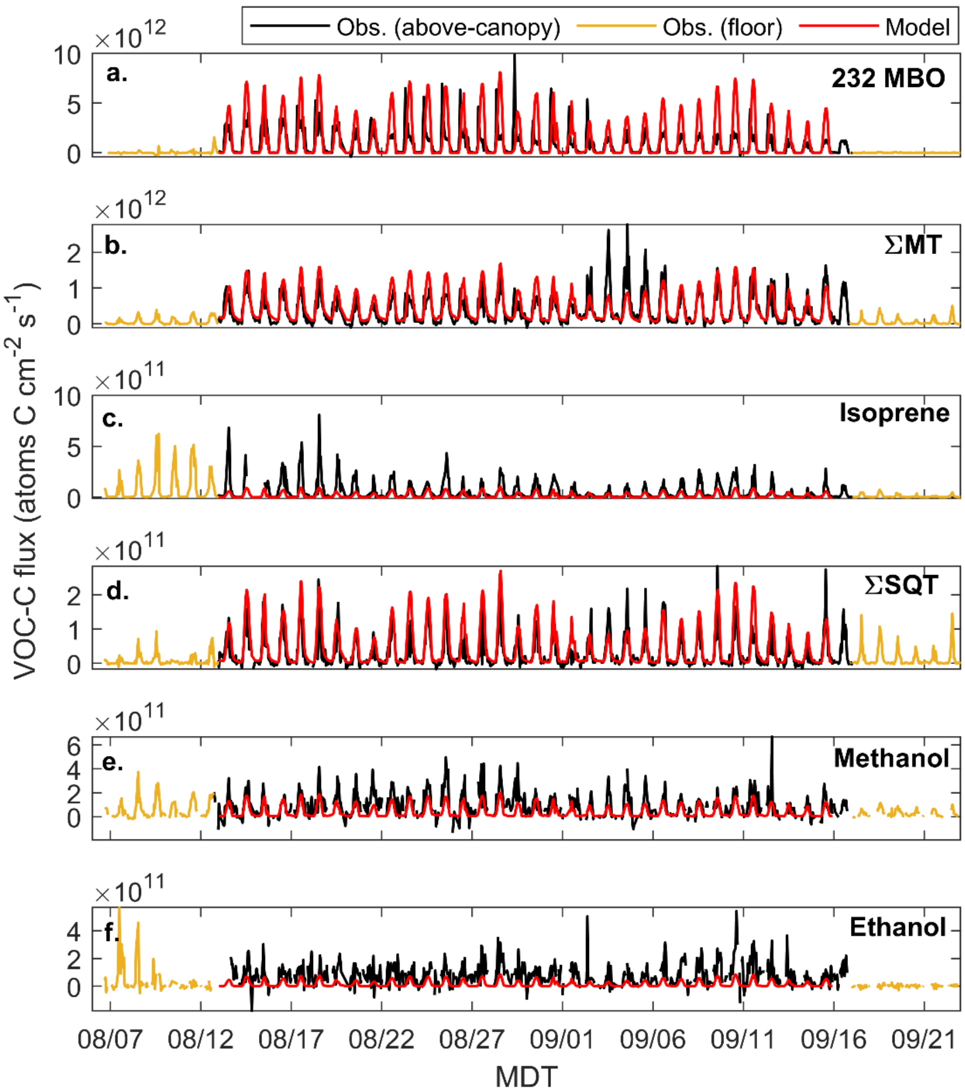

Figure S13: Above-canopy (27.8 m, black) and forest floor (1.9 m, yellow) VOC-C flux measurements for a) 232-MBO, b) ΣMT, c) isoprene, d) ΣSQT, e) methanol, and f) ethanol. The corresponding above-canopy model predictions are shown in red.

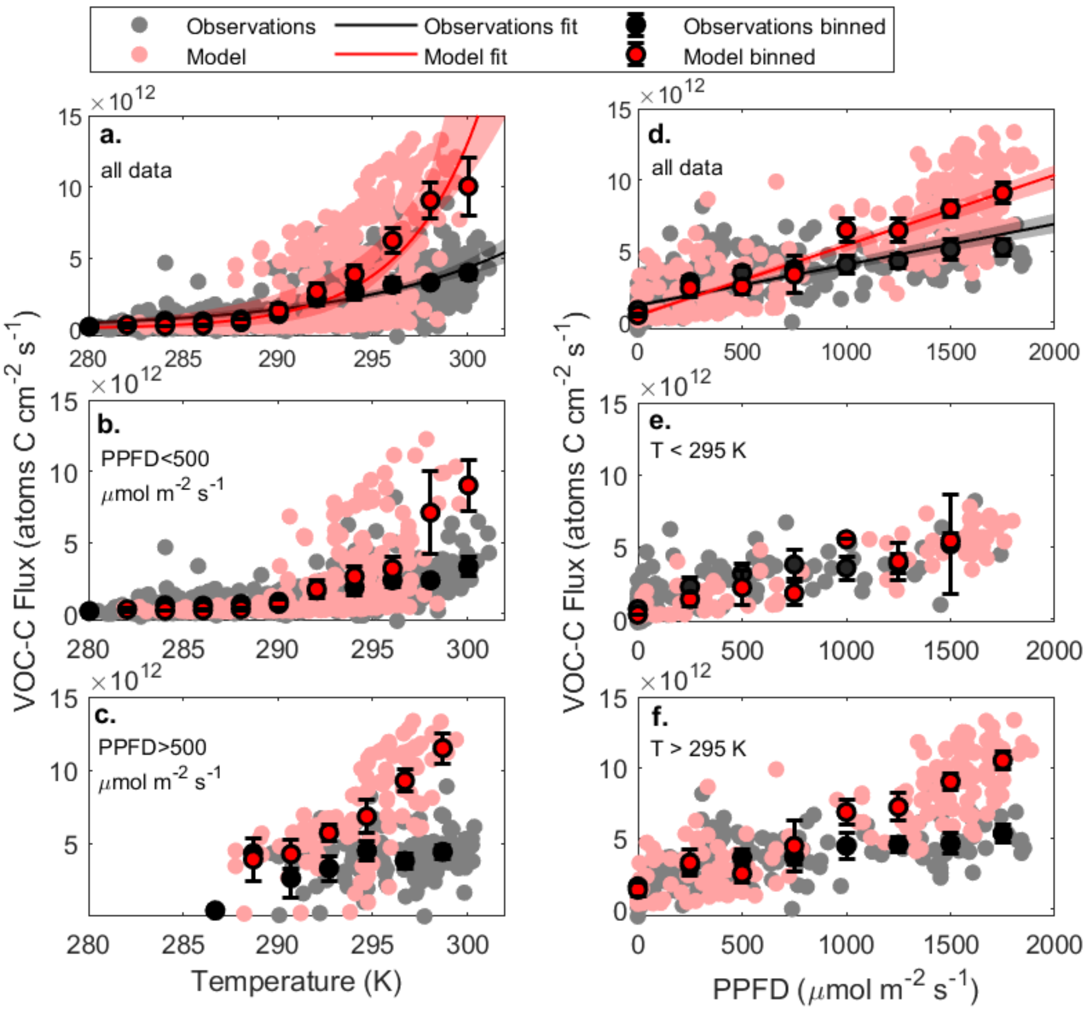

Figure S14: Temperature and light sensitivity of the observed (black) and modeled (red) VOC-C fluxes. The flux-temperature dependence is plotted for a) all data, b) PPFD > 500 μmol m^{-2} s^{-1}, and c) PPFD < 500 μmol m^{-2} s^{-1}. The flux-light dependence is plotted for d) all data, e) T < 295 K, and f) T > 295 K. Temperature fits follow the form y = $a\exp^{b(x-297)}$ with coefficients and bootstrapped 95% confidence intervals presented in the main text. Fits for PPFD are linear, y = $cx + d$, with fits, 95% bootstrapped confidence intervals, and correlation coefficients for the full data ensemble of: $c_{obs} = 2.9\times10^{9}$ [2.6×10^{9}, 3.1×10^{9}], $c_{mod} = 4.9\times10^{9}$ [4.7×10^{9}, 5.2×10^{9}], $d_{obs} = 1.2\times10^{12}$ [1.0×10^{11}, 1.3×10^{12}], $d_{mod} = 4.6\times10^{11}$ [3.6×10^{11}, 6.1×10^{11}], $r^2_{obs} = 0.56$, $r^2_{mod} = 0.81$.

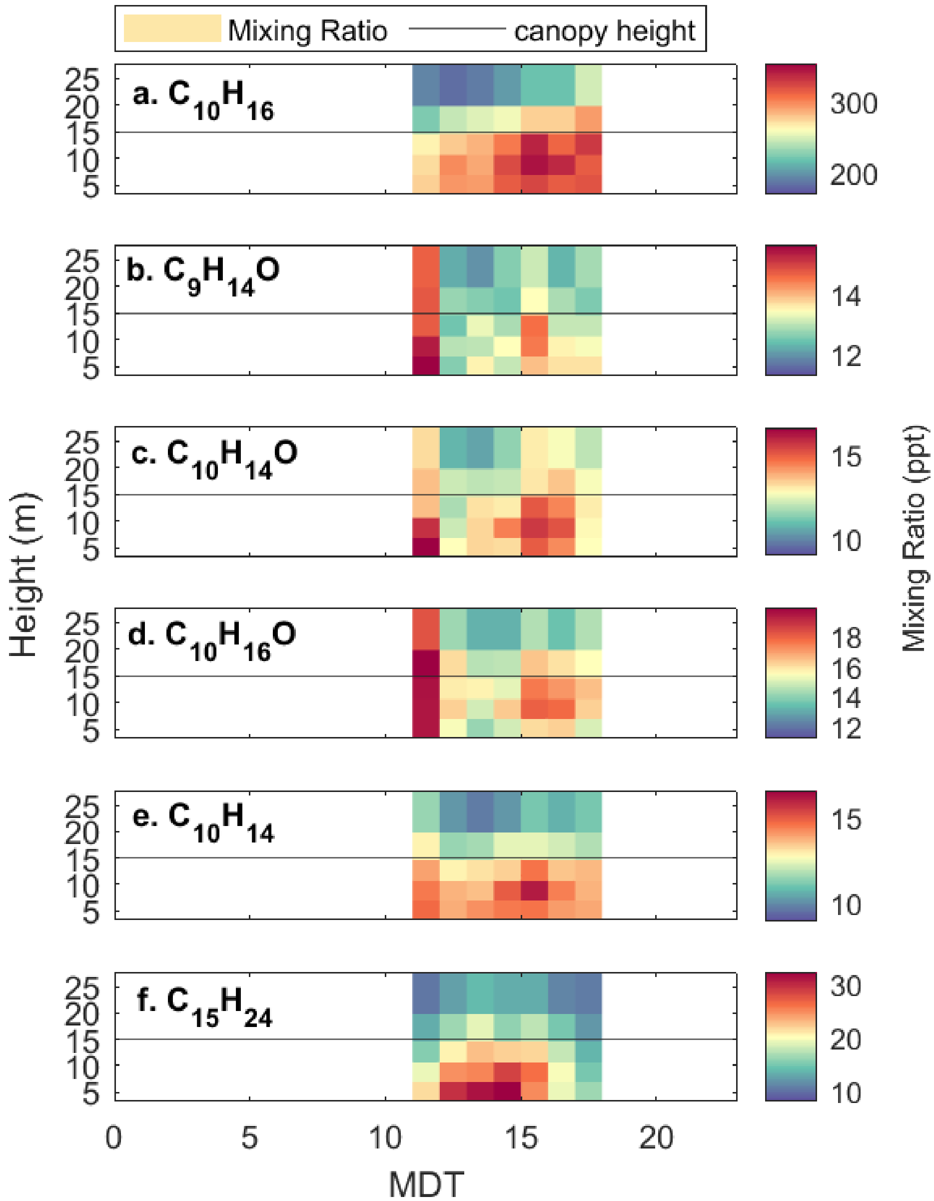

Figure S15: Diel concentration gradients for (a) ΣMT, (b-e) MT oxides, and (f) ΣSQT averaged over the entire study. Horizontal line indicates the canopy height within the flux footprint.

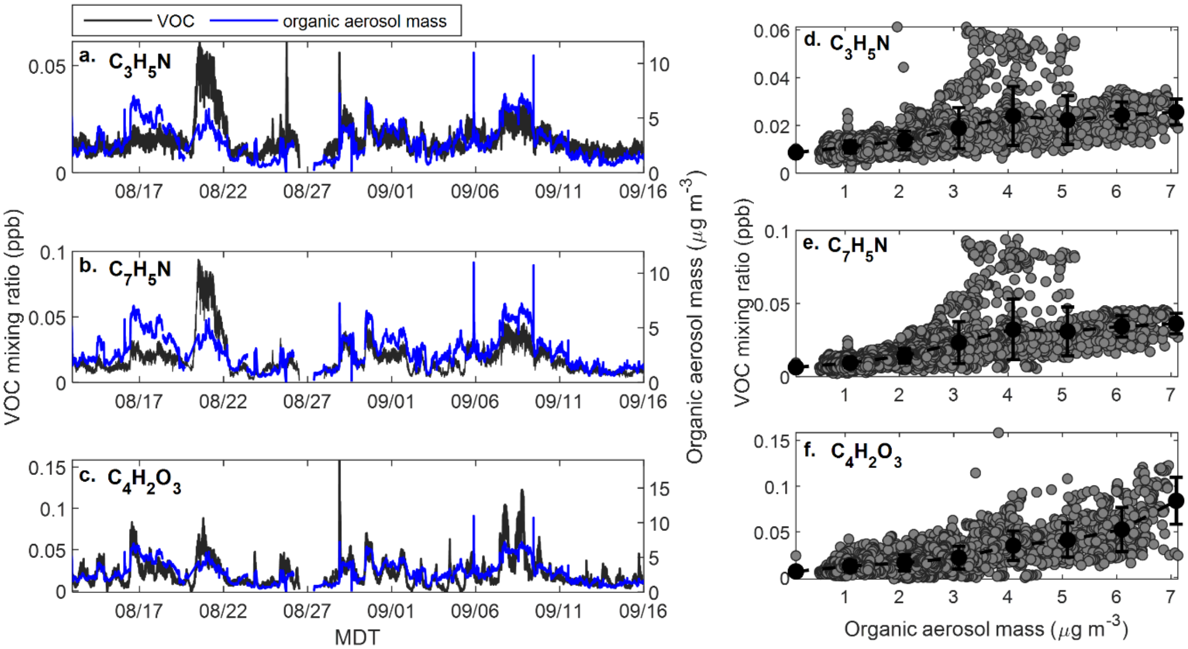

Figure S16: Biomass burning influence during the study as diagnosed with PTRMS-derived VOC tracers (black) and AMS-derived organic aerosol mass (OA, blue line). Data are plotted separately for a) propanenitrile, b) benzonitrile, and c) maleic anhydride. The corresponding regressions (d-f) show a strong maleic anhydride:OA correlation, while the nitriles exhibit periods where they diverge from OA, indicating a change in fire source or aging.

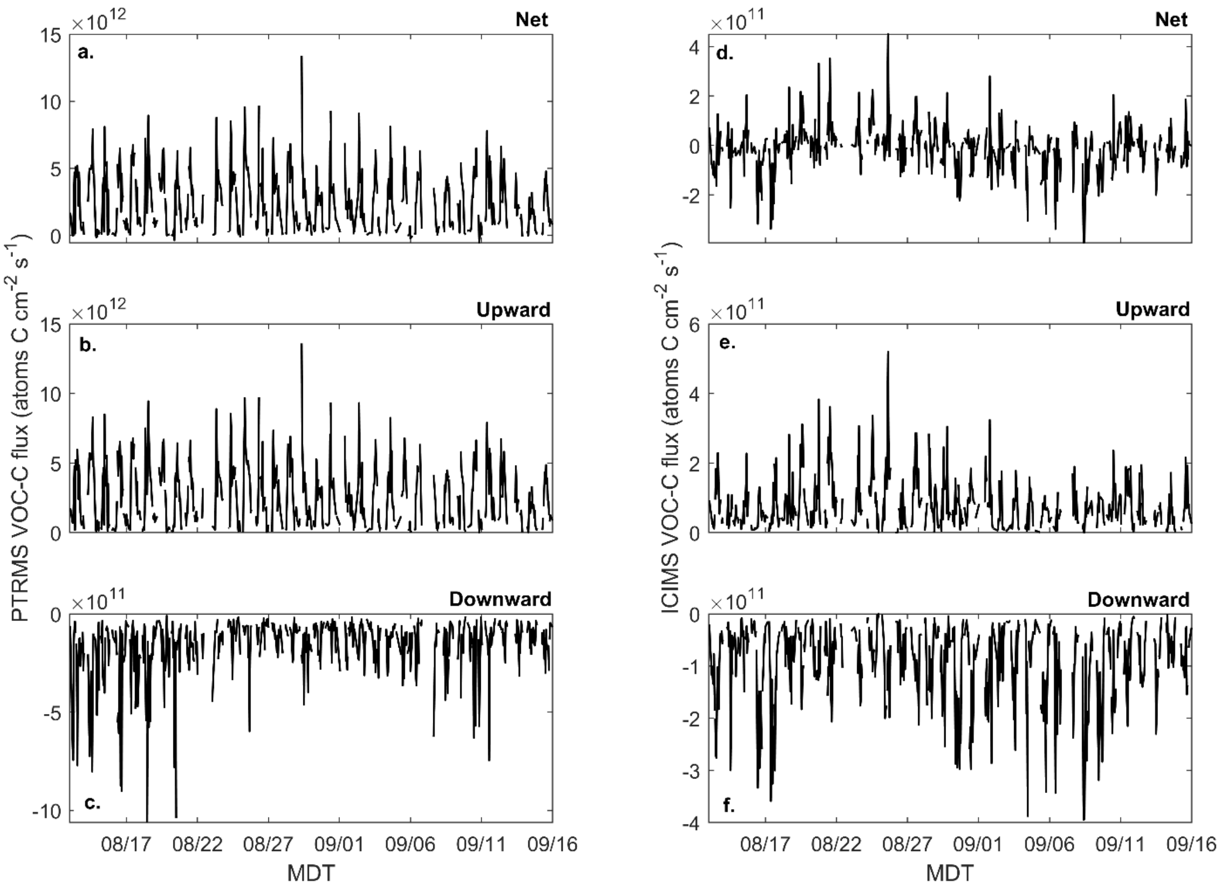

Figure S17: Total net (a + b), upward (b + c), and downward (e + f) VOC-C fluxes as measured by PTRMS and ICIMS.